# Fabrication and Properties of Thin-Walled SOFC Electrolyte Tubes

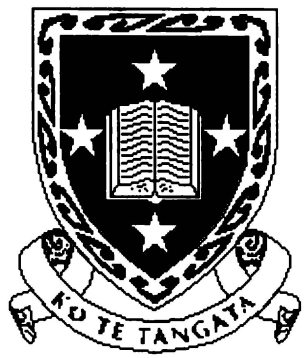


The University of Waikato

*Te Whare Wānanga o Waikato*

A thesis submitted in partial fulfillment of the requirements

for the degree of Doctor of Philosophy

at the University of Waikato

by

Charles Edward Hatchwell

May, 1999

# Erratum

Page 9, line 5, replace Cr-forming with $Cr_2O_3$-forming.

Page 12, line 7, $CeO_2$-basesd should read $CeO_2$-based.

Page 33, equation 2.1 should be replaced with $t = \frac{(r_A + r_O)}{\sqrt{2}(r_B + r_O)}$.

Page 36, line 19, delete the word neutrality and replace with condition.

Page 37, lines 3, 8 and 11, omit the word neutrality.

Page 37, line 17, omit the word neutrality and replace with condition.

Page 38, line 16, remove the word neutrality.

Page 42, paragraph 2, line 4, (both approximately 132 pm) should read (100 and 116 pm respectively).

Page 43, the last sentence of this page should read, This transformation occurs by electronic charge compensation, forming $La_{1-x}Ca_xCr^{3+}_{1-y}Cr^{4+}_yO_{3-\delta}$.

Page 44, Eq. 2.19 should be omitted.

Page 52, Table 2.1 should read Table 2.2.

Page 55, paragraph 2, line 3, $B^{4+}$ should read $B^{2+}$.

Page 63, the final sentence of this page should read, Typical chromia forming alloys include Ducrolloy (composed of 94% Cr, 5% Fe and 1% $Y_2O_3$) (51), Haynes 230 (57Ni-22Cr-14W-2Mo) (68), MA 754 (78Ni-20Cr-1Fe-0.5Ti-0.6$Y_2O_3$-0.5Ti-0.3Al-0.05C) (69) and Inconel 600 (72Ni-16Cr-8Fe); the components in brackets are given in weight percent (wt.%).

Page 64, paragraph 3, line 5, the word deposition should be replaced for permeation.

Page 64, paragraph 3, the formulae $(CrMn)O_4$ should read $(CrMn)_3O_4$.

Page 67, final sentence, Small circular cylinders, should read Small cylinders.

Page 89, paragraph 2, line 8, EVD should be replaced by electrochemical vapor deposition (EVD).

Page 95, omit the words, silver and, from the Table 4.2 caption.

# *Abstract*

The object of this thesis was to fabricate tubular solid oxide fuel cell (SOFC) systems operating with both high and medium temperature electrolytes, and then to study their electrical behaviour using various current collection methods. The research has demonstrated that yttria-stabilised zirconia (YSZ) and $Ce_{0.8}Gd_{0.2}O_{1.9}$ tubular electrolytes can be used as a basis for fabricating excellent high thermal shock resistant, rapid start up SOFC systems. The feasibility of using current collection materials with the $Ce_{0.8}Gd_{0.2}O_{1.9}$ electrolyte system at operational and co-firing temperatures has also been established via chemical compatibility studies.

Three methods of cathode current collection were investigated. These included silver coatings applied as strips along the cathode, Nimonic 90 alloy wires, and grooved metal Cr5Fe1$Y_2O_3$ plates.

Conductive coatings were applied to the surface of the Nimonic 90 wires and Cr5Fe1$Y_2O_3$ plates. The effect these coatings had on cell performance was studied. For example, an 8 mol % YSZ tubular based SOFC was used in combination with an Ag-$La_{0.8}Sr_{0.2}CrO_3$ coated Cr5Fe1$Y_2O_3$ metal plate. At 900°C and 0.7 V, using $H_2$ bubbled through $H_2O$ at 25 $cm^3$ $min^{-1}$, a current density of 40 mA $cm^{-2}$ was achieved for the coated Cr5Fe1$Y_2O_3$ as compared to 16 mA $cm^{-2}$ for the non-coated.

Dense (98% relative to theoretical), gas-tight, $Ce_{0.8}Gd_{0.2}O_{1.9}$ electrolyte tubes were successfully fabricated using an extrusion process. Processing parameters, such as the modification of the $Ce_{0.8}Gd_{0.2}O_{1.9}$ particle size by heat-treatment and addition of the correct proportions of organic extrusion aids, were shown to determine the quality of the final sintered tube. Electrodes were added to the electrolyte tube and the cell tested. At 600°C, using $H_2$ bubbled through $H_2O$ at 25 $cm^3$ $min^{-1}$, an open circuit voltage of 0.911 V was achieved.

The chemical compatibility of the $Ce_{0.8}Gd_{0.2}O_2$ electrolyte with perovskite current collect coatings and $Cr_2O_3$ (the scale formed on the surface of Cr-based metal interconnects) was studied. The $Cr_2O_3$ and phase pure (La,Sr)$CrO_3$ perovskite were shown to be chemically compatible with the electrolyte at typical operating

temperatures, and at co-firing temperatures. Second phases associated with the perovskite coatings were, however, shown to react with $Ce_{0.8}Gd_{0.2}O_{1.9}$ at co-firing temperatures, digesting and reacting with the electrolyte. The reaction products formed were considered to be Cr based perovskite phases.

This thesis concludes with recommendations for future study.

# *Acknowedgments*

I would like to thank Prof. Nigel Sammes for introducing me to the topic of Fuel Cells, for his time, patience and advice throughout my studies, and for providing me with the great opportunity to study at Industrial Research Ltd. (IRL) in Wellington and at Keele University in England.

I would like to express my deep appreciation to Dr. Ian Brown, for allowing me to study at IRL. This opportunity has enriched my life enormously, not only furnishing me with fruitful insights into science, but also providing me with the freedom to interact with an awesome group of people!

I am indebted to Bill Owers, Dr Mark Bowden, Allan Clarke, Martin Ryan, Vaughn White, Carolyn Sheppard, Dr Glen Barris, Dr Marc Daglish and Dr Holly Shulman of the IRL ceramics group. Their patience, kindness, help and advice made an environment that was incredibly friendly and supportive. Hopefully in years to come I will afford other people the same environment that they have shown me.

Thanks also to Prof. Kevin Kendall for his warm hospitality, taking on the "mad kiwi" from New Zealand, and for running me ragged around the squash court.

Above all I would like to thank my family (Edward, Vera and Lyndsey Hatchwell) and my girlfriend Janine Manhart, I owe you all so much. Cheers for putting up with the "ugly side" of me that few people ever see, it cannot have been easy. Your love and support was overwhelming.

To my fellow research students/friends from Waikato and Keele University (Dr Mike Brown, Basil Fenton, Dr Geoff Tompsett, Matt Henderson, Dr Mike Phillipps, Ros Phillips, Tracy Murray, Rupert, Dr Lyndon Mitchell, Olivier Bellon and Dr Richard Whitfield), you all provided some well-needed laughs, good times and help, thanks.

I would also like to praise Yunagi Zhang, Lesly Falconer, Jijian Lu, Alf Harris, Dave Wild, Kay Card, Dr Nick Long, and the workshop boys at Waikato University and IRL, for their patience and technical assistance.

To my friends, you know who you are, thanks - I think, for the gibes of "so have you finished your thesis yet", it has set me back emotionally for the next ten years!

# Table of Contents

**Chapter Two: The Solid Oxide Fuel Cell Interconnect/Current Collect**

**Chapter Three: Experimental Methods**



**Chapter Four: Cathode Current-Collectors for a Novel Tubular Solid Oxide Fuel Cell Design**

**Chapter Five: Fabrication and Properties of $Ce_{0.8}Gd_{0.2}O_{1.9}$ Electrolyte-Based Tubular Solid Oxide Fuel Cells**



**Chapter Six: Current-Collectors for a Novel Tubular Solid Oxide Fuel Cell Design**

**Appendices:**



**List of Figures:**

**List of Tables:**

# Chapter One

## *Introduction to the Solid Oxide Fuel Cell*

## 1.1 Introduction to the Solid Oxide Fuel Cell

Described in Chapter One is an introduction to the solid oxide fuel cell (SOFC), its principles of operation, efficiency, component materials, fabrication and design. The scope of this Chapter is quite broad in order to understand this complex system. For example, the single SOFC unit consists of an anode, electrolyte and cathode. Each of these components has, for example, its own specific material requirements and associated defect chemistry and conductivity. The purpose of this Chapter, is to show how these factors are interrelated and integrated to produce the SOFC system.

A fuel cell is an electrochemical device that converts the energy of a fuel, such as $H_2$ or natural gas, directly into electricity, without the inherent inefficiencies found in traditional heat engines (*1*).

The SOFC is distinguished from other fuel cell designs by the use of a solid state oxide ion conducting electrolyte. A major reason for the development of fuel cells is their ability to convert chemical energy directly to electrical energy, achieving high conversion efficiencies that are not subject to the Carnot type inefficiencies of conventional combustion engines. Since the principles of operation were first reported by Sir William Grove in 1839, the fuel cell has come a long way (*2*). Now becoming a commercial reality, organisations such as Westinghouse (*3*) and Siemens (*4*) are developing SOFCs for use in industry, providing highly efficient, low polluting power generating systems. In June 1998 the Dutch utility NUON, using a 100 kW Westinghouse SOFC system, started supplying 100 kW into the Dutch grid (*3*).

## 1.2 Principles of operation

The operation of a single SOFC unit is depicted in Fig. 1.1. Here the porous anode and cathode (electrodes) are separated by a dense solid electrolyte. Oxygen supplied to the cathode is reduced, accepting electrons from the external circuit to form oxide

ions. The oxide ions then diffuse through the electrolyte to the anode, where they react with the fuel (in this case $H_2$) to produce water. Electrons liberated from the anode reaction are released into the external circuit, flowing back to the cathode, generating direct current.

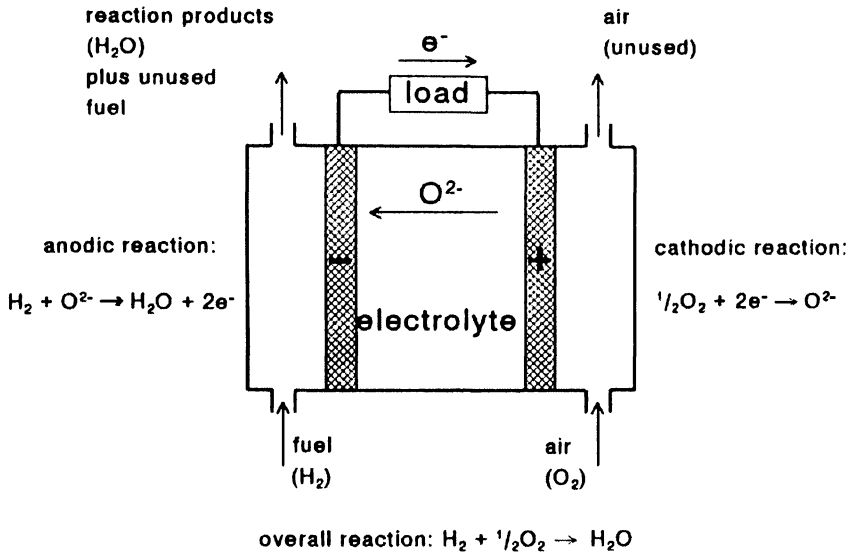


Fig. 1.1. Basic operating principles of a single SOFC unit (*5*).

The simplified cathode and anode reactions are given below in Eq. 1.1 and Eq. 1.2. For practical power generation, single SOFC units are electrically connected in series using interconnects to form stacks (repeat units of anode, electrolyte, cathode and interconnect). These stacks can then be connected in parallel to increase total power output, or in series to increase the voltage.

For an oxygen ion conducting electrolyte, the $O_2$ is reduced at the cathode

Eq. 1.1 $$O_{2(cathode)} + 4e^- = 2O^{2-}_{(electrolyte)}.$$

At the anode, the reverse reaction occurs (considered thermodynamically as the primary electromotive reaction)

Eq. 1.2 $$2O^{2-}_{(electrolyte)} = O_{2(anode)} + 4e^{-}.$$

Thus, the overall cell reaction (which determines cell voltage) is given as

Eq. 1.3 $$O_{2(cathode)} = O_{2(anode)}.$$

A SOFC can be considered as an oxygen concentration cell. The electromotive force (emf) or reversible (thermodynamic) voltage, $E_r$, is represented by Eq. 1.4, the Nernst equation (where the ionic transport ($t_i$) number is considered unity),

Eq. 1.4 $$E_r = \frac{RT}{4F}\ln\frac{P_{O_2(cathode)}}{P_{O_2(anode)}},$$

where $R$ is the gas constant, $T$ the temperature, $F$ the Faraday, and $P_{O_2}$ the oxygen partial pressure of oxygen at the electrode.

For a specific oxygen partial pressure at the cathode, the magnitude of $E_r$, is dependent on the anode oxygen partial pressure, which in-turn is dependent on the type of fuel and its respective composition. For example, when $H_2$ is introduced to the anode, the reaction is

Eq. 1.5 $$H_{2(anode)} + \frac{1}{2}O_{2(cathode)} = H_2O_{(anode)}.$$

Thus, the reversible cell voltage is then given as

Eq. 1.6 $$E_r = E^o + \frac{RT}{4F}\ln P_{O_2(cathode)} + \frac{RT}{2F}\ln\frac{P_{H_2(anode)}}{P_{H_2O(anode)}}.$$

$E^o$ is the standard potential. Depending on the fuel composition, water vapour, and oxidant, the open circuit potential of the cell is typically 0.8-1.0 V.

$E_r$ is equal to $E^o$ at the standard state, such that the following equation is established for every fuel.

Eq. 1.7 $$E_r = -\frac{\Delta G^o}{zF} = -\frac{\Delta H^o - T\Delta S}{zF}.$$

For the combustion reaction, $\Delta G^o$ is the standard Gibbs free energy change, $\Delta H^o$ is the standard enthalpy change, $\Delta S$ the standard free entropy, and $z$ is the moles of oxygen required to oxidise one mole of fuel multiplied by a factor of four. The maximum energy is given as $-\Delta G^o$, where the ideal thermodynamic efficiency is represented by $\Delta G^o / \Delta H^o$.

The effect of temperature and partial pressure on the reversible voltage of a fuel cell can be expressed in terms of the change in free energy with temperature (Eq. 1.8), and pressure (Eq. 1.9), where $\Delta V$ is the change in volume.

Eq. 1.8 $$\left(\frac{\partial E_r}{\partial T}\right)_p = \frac{\Delta S}{zF},$$

Eq. 1.9 $$\left(\frac{\partial E_r}{\partial P}\right)_T = -\frac{\Delta V}{zF}.$$

For the reaction between hydrogen and oxygen, the entropy change is negative, thus the thermodynamic voltage of the cell decreases with increasing temperature. The volume change is negative so the voltage increases with increasing pressure. Increased operational temperatures can improve cell performance, as it increases mass transfer, enhances reaction rates and can lower resistances associated with electrodes/electrolyte (*6*).

## 1.3 Efficiency/polarisation losses

The efficiency of an SOFC is defined as the product of the heating value efficiency and electrochemical efficiency. The heating value efficiency is defined as the ratio of heat energy (the quantity of useable fuel available in the SOFC to produce electricity), to the amount of heat energy contained in all combustible species in the fuel gases fed to the fuel cell. The electrochemical efficiency is the sum of thermodynamic, voltage and current efficiencies. The following discussion will concentrate on voltage efficiency, as it is relevant to the scope of this thesis.

In reality, under operating conditions when current is drawn, the voltage drops below the maximum voltage or reversible voltage ($E_r$). Fig. 1.2 is an I-V curve (polarisation curve), and represents the performance of an SOFC; here the potential difference is seen to decrease with increasing current density (load).

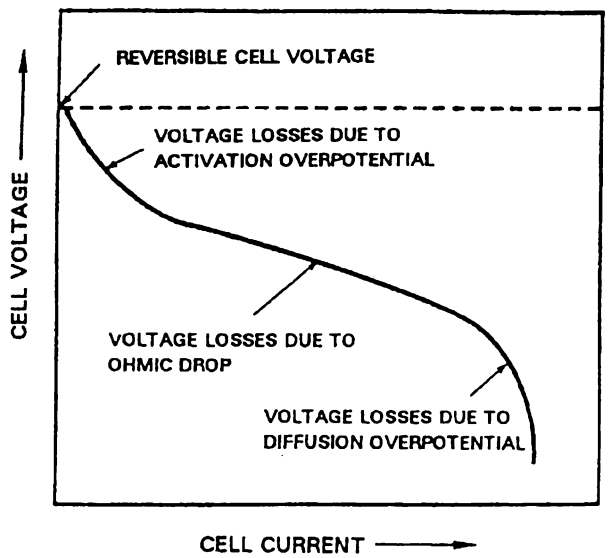


Fig. 1.2. I-V curve (polarisation curve) of an SOFC (*6*).

The voltage decrease is dependent on current density, temperature, pressure, gas flow rate and gas composition, and component materials. Differences between the

maximum voltage ($E_r$) and the actual operating voltage ($E_{op}$) are due to losses. These losses are termed polarisation, overvoltage or overpotential, and are given the symbol $\eta$; where the total polarisation of the cell can be written as

Eq. 1.10 $$\eta = \eta_A + \eta_D + \eta_R + \eta_\Omega .$$

Where $\eta_A$ is the charge activation polarisation, $\eta_D$ concentration polarisation, $\eta_R$ reaction polarisation and $\eta_\Omega$ ohmic polarisation. Activation polarisation ($\eta_A$) is the extra potential needed to decrease the energy barrier of the rate-determining step in order for the electrode reaction to proceed at the required rate. Diffusion polarisation ($\eta_A$) occurs when the electrode reaction is hampered by mass transport effects; where for example, the rate of addition of reactants and/or removal of products is slower than the discharge current reactions. Reaction polarisation ($\eta_R$), similar to diffusion polarisation, occurs when the reaction rate to supply reactants or remove products is slow. Ohmic polarisation ($\eta_\Omega$), defined in Eq. 1.11, is caused by the total internal resistance, $R_i$, associated with the electrolyte, electrodes, current collectors and contact resistance between cell components (*6*).

Eq. 1.11 $$\eta_\Omega = jR_i .$$

In general terms the internal resistance is considered to be independent of current density $j$, such that Ohms law is obeyed; so concentration polarisation losses can be neglected (I-V characteristics are linear). Therefore, if the power output ($P_W$) of the fuel is the product of voltage ($E$) and current ($I$), as given below

Eq. 1.12 $$P_W = EI ,$$

such that the power density can be derived using the linear portion of the I-V curve (ohmic part), where $R_t$ is the ohmic loss, the cell voltage (Eq. 1.13) is given as

Eq. 1.13 $$E = E_r - R_i I \,.$$

Eq. 1.14 shows the power/current relationship is parabolic

Eq. 1.14 $$P_W = I\left(E_r - R_i I\right).$$

Generally, under operating conditions, SOFCs are run at a constant current and varying voltage. The typical target current densities are in the range of 0.3 A $cm^{-2}$ at 0.75 V (*4*).

## 1.4 Component materials

As described previously in Section 1.2, the SOFC stack consists of four components, the interconnect, the anode, the electrolyte, and the cathode. These components perform specific functions and are fabricated from a variety of materials. The materials selection for each of these components is restricted due to the specific functions/roles each component has to achieve. The materials therefore have to meet certain material requirements. In general the material requirements for these SOFC components include:

- matching thermal expansion coefficient (TEC);
- thermal and chemical compatibility/stability with adjoining components in their respective atmospheres;
- good electrical contact;
- sufficient ionic or electronic/mixed conductivity.

The discussion below gives an overview of the most commonly used interconnect, anode, cathode and electrolyte materials, and their respective functions. These examples generally meet most of the material requirements stipulated above.

### 1.4.1 Interconnect/current collect

The interconnect, also referred to as the current collect or bipolar plate, has the primary function of electrically interconnecting single SOFC units to produce SOFC stacks. Many materials have been investigated for this function, including ceramic materials such as Sr (*7*) and Ca (*8*) doped $LaCrO_3$ (*9*), Cr-forming metal alloys (*10*) and cermets (metal-ceramic composites) (*11, 12*). The interconnect/current collect is discussed in detail in Chapter Two.

### 1.4.2 Anode

The anode is used to oxidise fuel and can be utilised for steam reforming and current collection. The most popular anode at present is the Ni-YSZ cermet (*13*). The Ni component has a high electrocatalytic activity towards $H_2$ oxidation, and provides the electronic conduction pathway. The YSZ has multiple functions, it:

- maintains the porous anode structure (supports the Ni catalyst and prevents the Ni from coarsening);
- allows the anode to have a matching TEC with other cell components;
- allows good adherence to the electrode;
- provides an ionic conduction pathway;
- can increase (with correct fabrication procedures) the triple phase boundary (TPB) between the YSZ and the Ni (*2, 14*).

The TPB is the reaction site where fuel gas, electrolyte and electrode connect. The TPB is where the fuel is oxidised. Therefore, a large TPB area would enhance the anode performance (*14*). At present anodes consisting of 40-50 vol% Ni in a matrix of YSZ, with a particle size range of approximately 1 μm, are utilised to achieve a large TPB (*15*). The anode must also be porous for the reactant gas to reach the TPB.

An alternative to the Ni-YSZ cermet is the perovskite based single-phase mixed ionic/electronic anode. The advantage with this anode material is that the fuel is oxidised over the entire surface of the anode (*16*).

### 1.4.3 Cathode

The electrochemical reduction of the oxidant occurs at the cathode. In a similar fashion to the anode, the cathode should be sufficiently porous to permit the rapid passage of gas to the reaction region.

$La_{1-x}Sr_xMnO_3$ (where x = 0.1-0.3) is commonly used in high temperature YSZ based SOFCs, because it has sufficient catalytic activity towards $O_2$ reduction (*6*). A perovskite based material with p-type conductivity, $(LaSr)MnO_3$, exhibits an electronic conductivity in the range of 100-200 S $cm^{-1}$, but shows poor ionic conductivity. Similar to the anode, the cathode active site for $(LaSr)MnO_3$ is the triple phase boundary, where $O_2$, $(LaSr)MnO_3$, and YSZ connect. Thus, YSZ/$(LaSr)MnO_3$ combinations can be used to improve electrode performance (*14*), by increasing the TPB area and improving ionic conduction (*17*). Alternative materials, such as $LaCoO_3$ have higher electronic (800 S $cm^{-1}$ at 800°C) and ionic conductivity and lower cathodic overpotentials (*18*). Unfortunately, $LaCoO_3$ has a mismatched TEC and can react with YSZ.

$(LaSr)MnO_3$ is not used at lower operating temperatures because the cell performance will drop due to increased cathode polarisation (reaction rates are reduced). Mixed conductors such as $La_{1-x}Sr_xCoO_{3-\delta}$ and $La_{0.6}Sr_{0.4}Co_{0.2}Fe_{0.8}O_3$ used in conjunction with lower temperature $CeO_2$-based electrolyte SOFCs yield higher electrochemical performances and reduced cathode polarisation than $(LaSr)MnO_3$. Cathode materials such as $La_{0.84}Sr_{0.16}CoO_3$, exhibit high mixed conductivity and high activity for oxygen reduction at low temperatures (*17, 19-21*). For $La_{0.84}Sr_{0.16}CoO_3$, the oxygen reduction reactions are considered to occur at the $O_2/La_{1-x}Sr_xCoO_{3-\delta}$ interface rather than at the triple phase boundary as observed for $(LaSr)MnO_3$ (*21*). Additionally, Ag-perovskite cermets (Ag-$La_{0.7}Sr_{0.3}CoO_3$) have lower electrode resistance and interfacial resistance

than ceramic electrodes (*22*). The low electrode resistance is beneficial when dealing with cell geometries with long current paths. Ag is considered a good candidate material for incorporation into the cermet as it has high catalytic activity (*23*), high electrical conductivity, and is not appreciably volatile below 750°C (*22*).

## 1.5 Introduction to the SOFC electrolyte

The purpose of the SOFC electrolyte is to conduct ions between the cathode and the anode (see Fig. 1.1), completing the electrical circuit in the SOFC. The SOFC electrolyte should be:

- a good ionic conductor (oxide ion) and a good electronic insulator; thus it must have an ionic transport number close to unity;
- stable over a wide range of $Po_2$ ($1\text{-}10^{-17}$ atm. in SOFC environments);
- dense, to prevent air and fuel gas mixing (*24*).

Detailed below is a discussion on medium temperature $CeO_2$-based electrolytes and the high temperature YSZ electrolyte.

### 1.5.1 $CeO_2$-based electrolyte

Unfortunately, YSZ based SOFCs require high temperature operation (900-1000°C) to achieve sufficient ionic conductivity in the electrolyte (*25*). Reduced operational temperatures (500-700°C) widens the range of materials able to be utilised in SOFCs, allowing for example, the use of a stainless steel interconnect, rather than the equivalent high cost $(La,Sr)CrO_3$ (*19*). Temperature reduction can be achieved using $CeO_2$-based electrolytes as they have higher ionic conductivity than YSZ at lower temperatures (*25*).

Pure $CeO_2$ maintains the fluorite structure up to its melting point and exhibits extremely low ionic conductivity. The addition, however, of dopants such as $Sm_2O_3$,

$Gd_2O_3$ and $Y_2O_3$ into $CeO_2$, leads to the creation of oxygen vacancies, which are responsible for ionic conduction in the electrolyte (*25*).

The $CeO_2$-based electrolytes are discussed below with particular emphasis on $Gd_2O_3$ doping, as $Ce(Gd)O_{2-x}$ was studied in this thesis.

1.5.1.1 The relation of conductivity and temperature for doped $CeO_2$ electrolytes

Empirically, the temperature dependence of electrical conductivity of doped fluorite oxides such as $CeO_2$-basesd electrolytes can be described by equation Eq. 1.15, where A is the pre-exponential factor and $E_a$ is the activation energy of conduction (*25*)

Eq. 1.15 $$\sigma T = A\exp(-E_a / kT).$$

However, the temperature dependence of $CeO_2$-based electrolytes cannot be represented by a single exponential function. It is considered to occur in two distinct temperature regions (*26*). When a dopant such as $Y^{3+}$ is added to $CeO_2$, it is considered to form an association with an oxygen vacancy, as described in Eq. 1.16 using Kröger-Vink notation

Eq. 1.16 $$\left\{Y'_M V_O^{\bullet\bullet}\right\}^{\bullet} = Y'_M + V_O^{\bullet\bullet}.$$

At lower temperature, the charge carrier concentration is dependent upon the thermodynamic equilibrium between free defects and associated pairs. Due to defect associations at low temperature, a binding energy or enthalpy ($\Delta H_{AI}$) exists that is ascribed to the coulombic attraction of the charged defects and to the relaxation (strain) around the lattice; which is related to dopant size, charge and cation polarisability. The conductivity/lower temperature relation is given below, Eq. 1.17; where $W$ is the number of orientations of the associate, $\Delta S_{AI}$ and $\Delta H_{AI}$ are the entropy and enthalpy of association, respectively (*25*).

Eq. 1.17 $$\sigma T = (A'/W)\exp(\Delta S_{A1}/k)\ \text{x}\ \exp[-(\Delta H_m + \Delta H_{A1})/kT].$$

In the higher temperature region, the oxygen vacancies are assumed to be free, so that

Eq. 1.18 $$\sigma T = A' C_M \exp(-\Delta H_m / kT).$$

Where, $C_M$ is the total dopant concentration defined as a site fraction of the cation site, and $H_m$ is the activation enthalpy of migration. Kilner et al. (*26*) showed for strong binding energy (large association enthalpies), full association is apparent up to high temperatures. Ultimately for good conduction at low temperature, low association enthalpies are required to provide a high concentration of free oxygen vacancies at lower temperatures.

### 1.5.1.2 Dopant species and concentration

When doping ceria with a series of 3+ valence dopants, $Sm^{3+}$ yields the highest conductivity, followed by $Gd^{3+}$, then $Y^{3+}$. Here the ionic radii decrease from $Sm^{3+}$ down to $Y^{3+}$, where the $Sm^{3+}$ and $Gd^{3+}$ radii are closest to the host. There is an optimum dopant ionic radius at which the minimum association enthalpy is achieved between the dopant ion and the oxygen vacancy.

There is also an optimum dopant concentration at which maximum conductivity is achieved. With increasing dopant concentration, the conductivity initially increases, reaches a maximum, then decreases. This behaviour is ascribed to complex interactions between dopant ions and oxygen vacancies, and also due to the oxygen ion vacancy concentration (which is a complex function of dopant concentration and dopant species) (*25*).

### 1.5.1.3 Reduction of $CeO_2$-based electrolytes in fuel gas

In fuel gas atmospheres, $CeO_2$-based electrolytes are reduced from $Ce^{4+}$ to $Ce^{3+}$, inducing mixed conduction (electronic n-type/ionic conductivity) in the electrolytes, short circuiting the cell and thereby decreasing the SOFC output voltage. The severity of reduction is dependent on dopant, temperature and $Po_2$. With increasing temperature and decreasing $Po_2$, there is a critical $Po_2$ at which the ionic transference number ($t_i$) decreases (indicating n-type electronic conductivity is induced). There is a range of $Po_2$ over which the $t_i$ is stable, where the width of this stability range is dependent on dopant species. Ideally for an electrolyte, $t_i$ would remain close to unity ($t_i \geq 0.99$) over the required temperature and $Po_2$ range (YSZ achieves this) (*6, 25*). Yahiro et al. (*27*) showed the stability range of $t_i$ for doped Ce-based materials was influenced by the dopant species. For $Ce(Ln)O_{2-x}$ (Ln = Sm, Gd or Y), Sm had the widest $Po_2$ range over which $t_i$ was stable, followed by Gd, then Y. The $Po_2$ range can also be widened by double doping; substitution of Pr into $Ce(Gd)O_{2-x}$ is one example (*28*). Additionally reduction of the electrolyte can be suppressed by fabricating a thin dense layer of YSZ (*29, 30*) or $La_{0.9}Sr_{0.1}Ga_{0.8}Mg_{0.2}O_{2.85}$ (*31*) over the $Ce(Gd)O_{2-x}$.

### 1.5.1.4 The $Ce(Gd)O_{2-x}$ electrolyte in SOFC applications

Various studies have been performed on $Ce(Gd)O_{2-x}$ electrolyte based SOFCs (*19, 27, 31, 32*). Zheng et al. (*19*) compared the I-V characteristics of 5-10 μm (anode supported) and 300 μm (self-supported) thick electrolytes using a fuel cell arrangement of

$$(\text{cathode})La_{0.4}Sr_{0.6}Co_{0.2}Fe_{0.8}O_3\|(\text{electrolyte})Ce_{0.9}Gd_{0.1}O_{1.95}\|(\text{anode})\text{Ni/YSZ}.$$

Air was introduced at the cathode and fuel ($H_2/CO_2/H_2O$) at the anode. The I-V characteristics are shown in Fig. 1.3. The self-supported 300 μm thick electrolyte cell had a terminal voltage of 0.9 V while the anode-supported cell was 0.7 V. Zheng et al. (*19*) gave the following explanation to explain the observed results. The EMF should be dependent on the $Po_2$ at the electrodes and not the thickness of the cell.

As $Ce_{0.9}Gd_{0.1}O_{1.95}$ is a mixed conductor, current and oxygen ion fluxes induce polarisation at the electrodes resulting in overpotentials, such that the cell EMF is reduced. Also, the difference in current and oxygen ion fluxes in mixed conductors are dependent on electrolyte thickness and are greater for thin electrolytes. This may explain the differences in terminal voltage. It was also proposed by Zheng et al. (*19*) that the reduced terminal voltage might be due to gas leakage. Due to the thickness of the self-supported electrolyte and its consequent resistance, the voltage dropped drastically with increasing current compared to the supported 5-10 μm thick electrolyte cell. The linear nature of the I-V curves indicated ohmic behaviour, allowing the cell resistance to be calculated from the gradient.

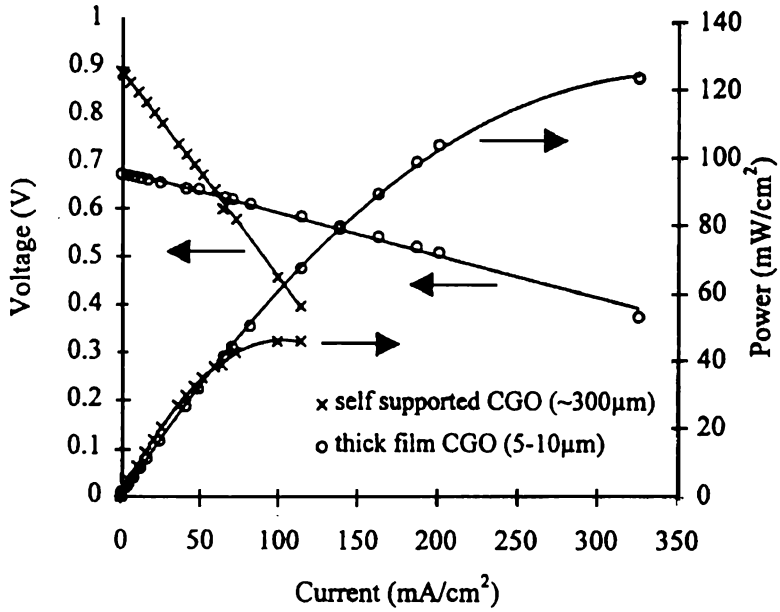


Fig. 1.3. I-V characteristics of $Ce(Gd)O_{2-x}$ based electrolytes (*19*).

## 1.5.2 Yttria stabilised zirconia (YSZ) electrolyte

As with $CeO_2$-based electrolytes the ionic conductivities of $ZrO_2$-based electrolytes are also a complex function of dopant species, dopant concentration and defect interactions. For brevity only the most commonly used high temperature electrolyte, yttria stabilised zirconia (YSZ), will be discussed (*33*).

Unlike $CeO_2$, which exhibits a single cubic fluorite phase up to its melting point, $ZrO_2$ has three phase transformations, which are monoclinic, tetragonal and cubic. Both $CeO_2$ and $ZrO_2$, however, exhibit extremely poor ionic conductivity. Substitution, of an aliovalent cation such as $Y^{3+}$ for $Zr^{4+}$, increases the ionic conductivity, by increasing the number of anion vacancies (by charge compensation) for oxide ion conduction. This is expressed using Kröger-Vink notation below

Eq. 1.19 $$Y_2O_3 \xrightarrow{ZrO_2} 2Y'_{Zr} + V_O^{\bullet\bullet} + 3O_O^x,$$

where: $Y'_{Zr}$ is the $Y^{3+}$ on the $Zr^{4+}$ site,

$V_O^{\bullet\bullet}$ is the oxygen vacancy,

$O_O^x$ is the occupied oxygen vacancy.

Ionic conductivity is proposed to occur by migration of oxygen ions via a complex multi-step oxygen vacancy mechanism. This can be considered simply as oxygen ions "hopping" (thermally assisted), from one unoccupied oxygen vacancy site to the next. The conductivity, as a function of temperature (over the temperature range of interest), obeys an Arrhenius type relation described in Eq. 1.15.

Typically $ZrO_2$ is doped with between approximately 8-10 mol% $Y_2O_3$ (referred to as fully stabilised zirconia) as it can be stabilised with the single cubic fluorite phase up to the SOFC operational temperature, avoiding problematic phase transformations during thermal cycling of the SOFC. This dopant concentration also exhibits a wide oxygen partial pressure range over which ionic conduction is dominant. Maximum ionic conductivity is also exhibited around the 8-10 mol% $Y_2O_3$ dopant range. To avoid problems associated with phase transformation and conduction, dopant concentrations greater than 8 mol% can be used (*33*). Thus, unlike $CeO_2$-based electrolyte materials, YSZ is tailored to be stable over the entire $Po_2$ range ($1\text{-}10^{-17}$ atm.) encountered in SOFC environments.

# 1.6 Fabrication of SOFC electrolytes

Various workers have fabricated highly dense electrolytes for SOFCs (see Table 1.1 and Table 1.2) by tape casting (*19, 31*), calendar rolling (*34*) and extrusion processes (*35*). These shaping processes have common requirements. With major emphasis on extrusion, detailed below are the materials and fabrication processes.

## 1.6.1 Materials

The following discussion gives a general description of the materials used in ceramic fabrication processes. This discussion is then followed by a literature survey (Table 1.1), describing in detail the materials used in extrusion and tape rolling of electrolytes. This Table highlights the variety and complexity of organic additives needed to successfully form an electrolyte into the desired shape.

### 1.6.1.1 Ceramic powder

Properties of the starting powders' such as particle size/distribution, morphology, homogeneity and extent of agglomeration are extremely important considerations when forming ceramics (*36*). For example, powder particle sizes below 1 μm are considered to reduce problems associated with extrusion (*36*). If, however, the surface area of the powder is too high, too many organic additives are required to produce a "green body" (unfired ceramic containing organic additives) with the correct flow properties. As discussed in the literature (*37*), a high proportion of organics will result in low green body densities and low sintered densities. Organics are added to the ceramic to confer flow properties so the material can be formed into the desired shape while maintaining structural integrity in the green state (*38*).

### 1.6.1.2 Solvent

The solvent provides the fluid medium for the other additives. A basic rule for solvent selection is that it should not react with the ceramic powder and it should dissolve the organic additives (*39*). Typical solvents are water, methyl alcohol, ethyl alcohol, toluene, acetone, n-hexane and methylethlylene ketone. Important solvent properties are dielectric constant, surface tension, viscosity, and boiling point (*40*).

### 1.6.1.3 Dispersant

As shown in Table 1.1 dispersants can be added to the solvent/powder system. For tape casting, the dispersant is used to maintain the stability of the slip (ceramic powder, additives and solvent mixture) by preventing the ceramic grains from agglomerating (*40*). The two mechanisms by which dispersants can stabilise a suspension are electrostatic stabilisation and polymeric stabilisation. Common dispersants include: sodium silicates, sodium carbonates, menhaden fish oil, glycerol trioleate and phosphate esters.

### 1.6.1.4 Binders and plasticisers

The binder is used to bind ceramic particles together, increasing the strength of the green shaped ceramic in wet and dry states (*38*). Methyl cellulose and hydroxyethyl cellulose are commonly used binders in aqueous systems (*41*), while PVB (Table 1.1) is a typical binder used in non-aqueous systems (*36*). Ceramic systems containing binder are usually shaped above their glass transition temperatures (Tg) (the temperature at which the binder changes from a brittle to a plastic state). A plasticiser can be added to decrease the Tg, improving the plasticity and flexibility of the green ceramic (*42*). By adjusting the binder:plasticiser ratio the correct strength and flexibility can be achieved. Typical plasticisers include di butyl phthalate (DBP) (*34*) and poly (ethylene glycol) (PEG) (*43*).

## 1.6.2 Processing

This Section gives an overview of ceramic processing with respect to electrolyte fabrication. A detailed description of various electrolyte fabrication processes is also included and is described in Table 1.2.

### 1.6.2.1 Mixing

One of the most important processes is proper mixing of the ceramic with the organic additives (*36, 44*). Poor mixing will result in areas of inhomogeneity such that pockets of binder and powder can form voids after firing. For extrusion, mixing is usually achieved using high intensity mixers such as pug mills or sigma-blade mixers, filter pressing or slurry mixing followed by drying (*36*).

### 1.6.2.2 Order of addition

The order of addition of the additives is also a critical step when processing ceramics (see Table 1.2, processes B and C). In the preparation of slips, the solvent, powder, and dispersant are mixed/milled to produce a suitable dispersed slip. The plasticisers and binders are then added in a second step milling/mixing step. The dispersant is added first to prevent competitive adsorption with other additives onto the particle surface (*40*).

### 1.6.2.3 Drying

Generally, in tape casting the drying rate is controlled, as fast evaporation rates of liquids can result in the formation of a skin and the trapping of bubbles. Drying the tape in a solvent saturated atmosphere can reduce drying rates. Decreased solvent gradients between the slip and the atmosphere have been shown to decrease deformation and cracking of the slip during drying. Typically, high shrinkage and differential shrinkage (due to differences in particle size, liquid content and drying rates) should be avoided as they can induce stresses (*42*). High shrinkage during

drying can be avoided by decreasing the surface area of the powder and subsequently decreasing the amount of organics added (*40*).

#### 1.6.2.4 Firing

Binder burnout is an extremely important consideration when firing a ceramic body. During binder burnout heating rates and dwell periods are selected to reduce pressure associated with organic burnout and moisture evaporation (*42*). Balachandran et al. (*39*) used a heating rate of 5°C/h, between 150-400°C, to slowly remove the organics from extruded ceramic tubes, stopping the formation of large voids and preventing the tubes from "bloating". After this sensitive stage, the heating rate can be increased to reach the required sintering temperature in a shorter time. The sintering is thus only dependent on the temperature, time and composition of the sample (*42*).

### 1.6.3 Extrusion

Extrusion is a plastic forming method that has been adapted to form tubular SOFCs (see Table 1.1 and Table 1.2). Extrusion is usually performed using an auger or piston extruder. Typically a plastic dough-like mixture consisting of ceramic, binders and additives is forced through a die to be formed into the desired shape (*38*). Extrusion using an auger has been utilised to fabricate support tubes in the seal-less tubular designed SOFC. The extrusion process involves ball milling the ceramic powder, calcining, blending with organics, kneading, extrusion, drying and firing. The organic additives and ceramic are mixed and kneaded to ensure homogeneity and adequate plasticity. The mixture is then de-aired, compacted in the auger and extruded (*6*).

Table 1.1. Literature survey of ceramic powders, organic additives and firing conditions of extrusion and tape rolling electrolyte fabrication processes.

| Process | Powder | Solvent | Dispersant | Binder | Plasticiser | Ref. |
|---|---|---|---|---|---|---|
| (A) Extrusion | 8YSZ | $H_2O$ | ammonium polyacrylate | cellulose-based | glycerol | (*45*) |
| (B) Extrusion | CGO | acetone | Hypermer KD1 | PVB | Octanol-1 | (*35*) |
| (C) Tape Rolling | CGO | MEK/ ethanol | p-hydroxy-benzoic acid | PVB | DBP | (*34*) |

CGO is $Ce(Gd)O_2$, 8YSZ is 8 mol% yttira stabilised zirconia, MEK is methyl-ethyl-ketone, PVB is polyvinyl butyral, DBP is di-butyl phthalate.

Table 1.2. Process procedures used in extrusion and tape rolling processes described in Table 1.1.

| Process | Process procedures | Ref. |
|---|---|---|
| (A) Extrusion | Pre-made tapes consisting of organics and powder were moistened in humidified environment, then mixed into a paste for extrusion. After extrusion the tubes were dried under ambient conditions, then sintered at 1420°C. | (*45*) |
| (B) Extrusion | CGO was initially heat-treated (550-1000°C). The solvent and dispersant were added to the powder and roller milled for between 4 to 12 h. The binder and plasticiser were then added and the mix milled for a further 12 to 24 h. The slurries were then tape cast onto acetate sheets, dried and then mixed manually into pastes/doughs for extrusion. After extrusion the tubes were dried in air for 24 h. Binders were burnt out at a rate of 1°C $min^{-1}$ to 500°C, with subsequent sintering between 1300 and 1600°C, for 2 to 10 h. | (*35*) |
| (C) Tape Rolling | CGO was heat-treated at 1100°C for 3 h (the surface area of the powder reduced from 36 $m^2 g^{-1}$ to 6.4 $m^2 g^{-1}$). The powder was mixed with the solvent and dispersant by an ultrasonic method, then ball milled 24 h. Subsequently the binder and plasticiser were added and the mix milled for a further 24 h. Finally, most of the solvent was evaporated off to make a paste for tape rolling. Green sheets were fabricated by repeatedly passing the ceramic paste between the rollers. Binders were burnt out at a rate of 1°C $min^{-1}$ to 400°C, with subsequent sintering at 1525°C, for 2 to 48 h. | (*34*) |

# 1.7 SOFC design

There are four common stack designs: the seal-less tubular (*46*), the segmented cell in series (*47*), the monolithic (*48*) and the planar (*4*). The differences between the designs include the method of sealing between fuel gas and oxidant, the nature of the electrical losses within the cells, and the methods of electrical interconnection between the cells (*2*). The discussion below is limited to the seal-less tubular, the planar, and the small diameter tubular SOFC design (the small diameter SOFC was used in this thesis).

## 1.7.1 Planar

The basic planar SOFC design is shown in Fig. 1.4. Repeat units of anode/electrolyte/cathode and interconnect (current collectors or bipolar plates) are stacked together forming the planar stack (*24*). The interconnect generally has a multi-functional role as gas distributor/separator, electrical interconnector and structural support.

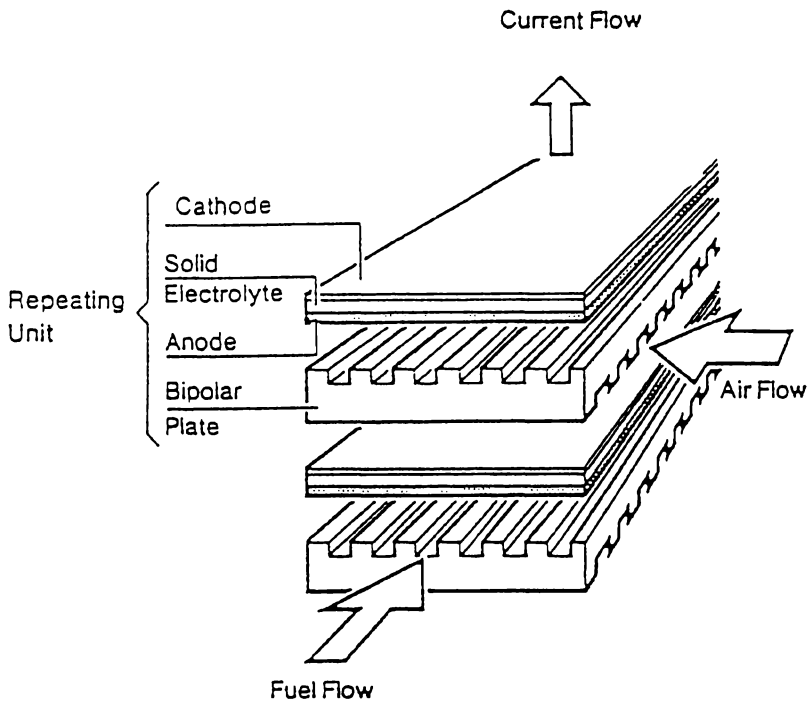


Fig. 1.4. The basic planar SOFC (*24*).

Major advantages of the planar SOFC over other designs include high power densities (*2*), the shortest current paths (lowest ohmic losses) (*24*), and simple design. A further advantage is the ability for components to be produced by conventional ceramic processing techniques such as tape casting (*49*) of the electrolyte, and application of the electrodes by tape casting (*50*), wet powder spraying (*51*) and screen printing (*49, 52*).

Disadvantages of the planar design include difficulty achieving adequate sealing, temperature gradients causing high thermal stresses (*53, 54*) and slow start-up (*55*).

### 1.7.2 Tubular Siemens Westinghouse SOFC

The current Siemens Westinghouse SOFC is shown in Fig. 1.5. The porous air electrode serves as the support onto which the electrolyte, anode and interconnect are fabricated. Fabrication of these cells is complex. It involves extrusion and sintering of the doped $LaMnO_3$ air electrode, electrochemical vapour deposition of the YSZ electrolyte, plasma spraying of doped $LaCrO_3$ interconnect, and slurry spraying and electrochemical vapour deposition of the Ni-YSZ anode (*46*). The tubes are approximately 2 cm in diameter with active cell lengths of up to 150 cm (active cell area is 834 $cm^2$) (*3*). At 0.7 V, current densities in the order of 0.2-0.35 A $cm^{-2}$ have been achieved for single cells operated in the range of 900-1000°C; where the fuel was 89% $H_2$ and 11% $H_2O$ and the oxidant was air (*46*).

A major advantage of this design is that no sealing is required to separate the exhaust air and exhaust fuel, thus the need for high temperature gas tight seals is eliminated. A major disadvantage is the long current paths (circumferential in the plane of the electrodes) in the porous electrodes which can cause appreciable ohmic loss (*24*). As shown in Fig. 2.11 (Section 2.4), the single cells are connected to form stacks.

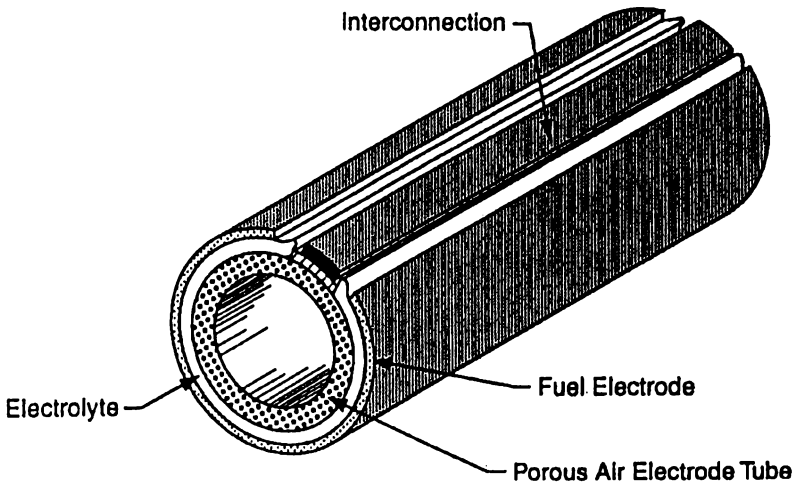


Fig. 1.5. The tubular Siemens Westinghouse SOFC (*46*).

### 1.7.3 The small diameter tubular SOFC

The small diameter tubular SOFC developed by Kendall et al. (*55-57*) has two major advantages over the conventional planar and tubular (Siemens Westinghouse) SOFC designs: the ability to survive extreme thermal cycling (good thermal shock resistance); and the ability of the electrolyte to be fabricated by a relatively simple and low cost extrusion technique. The single hollow tubular SOFC with associated electrodes and current collectors is shown in Fig. 1.6. Electrodes are applied using simple coating techniques involving electrode inks. The fuel is introduced to the anode through the inside of the hollow tube, while air surrounds the cathode on the outside.

A thousand tube YSZ electrolyte tubular stack was recently assembled for micro-cogeneration from natural gas. The system yielded 200 W of power and 20 kW of heat. The use of this system, Fig. 1.6, is envisaged as a small-scale cogeneration device for domestic purposes, with power generation in the range of 0.2 to 10 kW. It is proposed the small stacks could be integrated into houses using natural gas. The key component of this design is that, unlike other SOFC designs, it can handle the on/off cycling anticipated in the domestic environment (*57*). A major problem associated with this design is the development of a current collector/interconnector

for the anode. The small diameter of the tube restricts the fabrication options of the anode current collector.

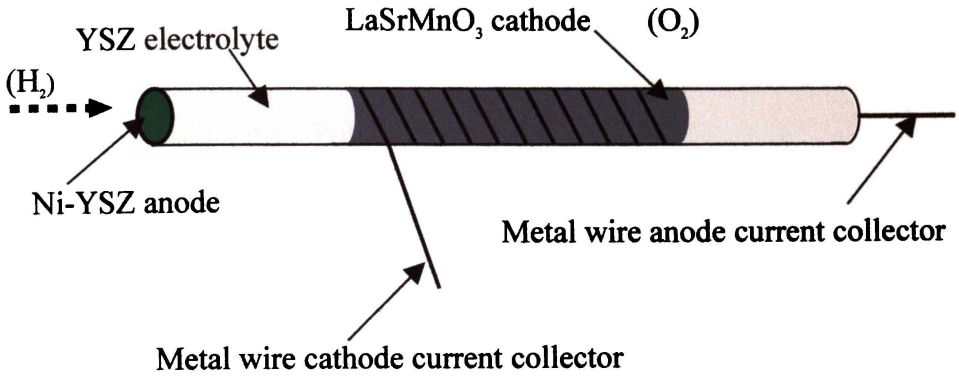


Fig. 1.6. The small diameter tubular SOFC.

## 1.8 References


1. W. Gao and N. M. Sammes, "Introduction to Electronic and Ionic Materials," World Scientific Publishing, Singapore, 1999.
2. N. Q. Minh, *J. Amer. Ceram. Soc.* **76**, 563 (1993).
3. S. E. Veyo and C. A. Forbes, *in* "Third European Solid Oxide Fuel Cell Forum" (P. Stevens, ed.), p. 79, Nantes-France, 1998.
4. H. J. Beie, L. Blum, W. Drenckhahn, H. Greiner, B. Rudolf, and H. Schichl, *in* "Solid Oxide Fuel Cells V" (U. Stimming, S. C. Singhal, H. Tagawa, and W. Lehnert, eds.), Vol. PV 97-40, p. 51. The Electrochemical Society, Inc., Aachen, Germany, 1997.
5. F. H. Vanheuveln, F. P. F. Vanberkel, and J. P. P. Huijsmans, *in* "14th Risø International Symposium on Material Science, High Temperature Electrochemical Behaviour of Fast Ion and Mixed Conductors" (F. W. Poulsen, J. J. Bentzen, T. Jacobsen, E. Skou, and M. J. L. Østergård, eds.), p. 53, 1993.
6. N. Q. Minh and T. Takahshi, "Science and Technology of Ceramic Fuel Cells," Elsevier Science B.V., Netherlands, p. 1, 1995.
7. I. Yasuda and M. Hishinuma, *Solid State Ionics* **80**, 141 (1995).
8. I. Yasuda and T. Hikita, *J. Electrochem. Soc.* **140**, 1699 (1993).
9. M. Dokiya, T. Horita, N. Saki, T. Kawada, H. Yokokawa, B. A. van Hassel, and C. S. Montross, *in* "14th Risø International Symposium on Material Science" (F. W. Poulsen, J. J. Bentzen, T. Jacobsen, E. Skou, and M. J. L. Østergård, eds.), p. 33, 1993.
10. W. Quadakkers, H. Greiner, and W. Köck, *in* "First European Solid Oxide Fuel Cell Forum" (U. Bossel, ed.), Vol. 1, p. 525, Lucerne Switzerland, 1994.
11. U. Vondercrone, F. Tietz, R. Vassen, and D. Stöver, *Euromat.* **97**, 215 (1997).
12. R. H. Song, D. R. Shin, and M. Dokiya, *in* "Fuel Cell", p. 179, Orlando Florida, November 17-20, 1996.
13. B. C. H. Steele, *Solid State Ionics* **86-8**, 1223 (1996).
14. M. Mogensen and S. Skaarup, *Solid State Ionics* **86-8**, 1151 (1996).

15. D. W. Dees, T. D. Claar, T. E. Easler, D. C. Fee, and F. C. Mrazek, *Solid State Ionics* **137**, 2141 (1987).

16. M. Mogensen, *in* "14th Risø International Symposium on Material Science, High Temperature Electrochemical Behaviour of Fast Ion and Mixed Conductors" (F. W. Poulsen, J. J. Bentzen, T. Jacobsen, E. Skou, and M. J. L. Østergård, eds.), p. 117, 1993.

17. R. Doshi, V. L. Richards, and M. Krumpelt, *in* "Solid Oxide Fuel Cells V" (U. Stimming, S. C. Singhal, H. Tagawa, and W. Lehner, eds.), Vol. PV 97-40, p. 379. The Electrochemical Society, Inc., Aachen, Germany, 1997.

18. O. Yamamoto, Y. Takeda, R. Kanno, and M. Noda, *Solid State Ionics* **22**, 241 (1987).

19. K. Zheng, B. C. H. Steele, M. Sahibzada, and I. S. Metcalfe, *Solid State Ionics* **86-8**, 1241 (1996).

20. W. Bakker, C. Milliken, J. Hartvigsen, S. Elangovan, and A. Khandkar, *in* "Solid Oxide Fuel Cells V" (U. Stimming, S. C. Singhal, H. Tagawa, and W. Lehner, eds.), Vol. PV 97-40, p. 254. The Electrochemical Society, Inc., Aachen, Germany, 1997.

21. M. Gödickemeier, K. Sasaki, L. J. Gauckler, and I. Riess, *Solid State Ionics* **86-8**, 691 (1996).

22. L. S. Wang and S. A. Barnett, *Solid State Ionics* **76**, 103 (1995).

23. R. Baker, J. Guindet, and M. Kleitz, *J. Electrochem. Soc.* **144**, 2427 (1997).

24. M. Mogensen, C. Bagger, K. Aasberg-Petersen, L. J. Christiansen, B. Sander, and J. N. Paulsen, ELSAM's SOFC Programme, Phase 2, 1992.

25. H. Inaba and H. Tagawa, *Solid State Ionics* **83**, 1 (1996).

26. J. A. Kilner and C. D. Waters, *Solid State Ionics* **6**, 253 (1982).

27. H. Yahiro, K. Eguchi, and H. Arai, *Solid State Ionics* **36**, 71 (1989).

28. B. G. Pound, *Solid State Ionics* **52**, 183 (1992).

29. K. Eguchi, T. Setoguchi, and H. Hiromichi, . Dept of Material Science and Technology, Kyushu University at Kasuga-shi, Fukuoka 816, Japan, 1990.

30. K. Eguchi, *J. Alloys Compounds* **250**, 486 (1997).

31. M. Sahibzada, R. A. Rudkin, B. C. H. Steele, I. S. Metcalfe, and J. A. Kilner, *in* "Solid Oxide Fuel Cells V" (U. Stimming, S. C. Singhal, H. Tagawa, and

W. Lehner, eds.), Vol. PV 97-40, p. 244. The Electrochemical Society, Inc., Aachen, Germany, 1997.

32. D. L. Maricle, T. E. Swarr, and S. Karavolis, *Solid State Ionics* **52**, 173 (1992).

33. F. T. Ciacchi, K. M. Crane, and S. P. S. Badwal, *Solid State Ionics* **73**, 49 (1994).

34. N. Ozkan and B. J. Briscoe, *J. Mat. Res.* **13**, 665 (1998).

35. O. Bellon, N. M. Sammes, and J. Staniforth, *J. Power Sources* **75**, 116 (1998).

36. M. A. Janney, *in* "The American Ceramic Society 96th Annual Meeting & Exposition, Short Course, Ceramic Forming Processes", Indiana Convention Center Indianapolis, Indiana, 1994.

37. A. Roosen, *in* "Ceramic Transactions, Ceramic Powder Science II" (G. L. Messing, E. R. Fuller, and H. Hausner, eds.), Vol. 1, p. 675, 1988.

38. M. A. Janney, "Ceramic Processing," p. 174. Chapman and Hall, 1995.

39. U. Balachandran, S. L. Morissette, J. J. Picciolo, J. T. Dusek, R. B. Poeppel, S. Pei, M. S. Kleefisch, R. L. Mieville, T. P. Kobylinski, and C. A. Udovich, *in* "1992 International Gas Research Conference", p. 2499, 1992.

40. R. Moreno, *Am. Ceram. Soc. Bull.* **71**, 1521 (1992).

41. J. E. Schuetz, *Ceram. Bull.* **65**, 1556 (1986).

42. J. S. Reed, "Introduction to the Principals of Ceramic Processing," p. 486. John Wiley & Sons, Inc., New York, 1988.

43. J. Zheng, J. S. Reed, and S. K. Verma, *Am. Ceram. Soc. Bull.* **73**, 61 (1994).

44. R. Moreno, *Am. Ceram. Soc. Bull.* **71**, 1647 (1992).

45. M. Prica, T. Alston, and K. Kendall, *in* "Solid Oxide Fuel Cells V" (U. Stimming, S. C. Singhal, H. Tagawa, and W. Lehner, eds.), Vol. PV 97-40, p. 619. The Electrochemical Society, Inc., Aachen, Germany, 1997.

46. S. C. Singhal, *in* "Solid Oxide Fuel Cells V" (U. Stimming, S. C. Singhal, H. Tagawa, and W. Lehnert, eds.), Vol. PV 97-40, p. 37. The Electrochemical Society, Inc., Aachen, Germany, 1997.

47. N. Hisatome, K. Nagata, S. Kakigami, and H. Omura, *in* "Fuel Cell", p. 195, Orlando Florida, November 17-20, 1996.

48. S. Majumdar, T. Claar, and B. Flandermeyer, *J. Am. Ceram. Soc.* **69**, 628 (1986).

49. W. Schafer, A. Koch, U. Heroldschmidt, and D. Stolten, *Solid State Ionics* **86-8**, 1235 (1996).

50. H. Takagi, H. Taira, S. Kobayashi, S. Sakamoto, and K. Tomono, *in* "Proceedings of the Fourth International Symposium on Solid Oxide Fuel Cells (SOFC-IV)" (M. Dokiya, O. Yamamoto, H. Tagawa, and S. C. Singhal, eds.), p. 120. The Electrochemical Society Inc., Yokohama, Japan, 1995.

51. R. Wilkenhoner, L. G. J. de-Haart, W. Mallener, and H. P. Buchkremer, *in* "Fuel Cell", p. 202, Orlando Florida, November 17-20, 1996.

52. Y. Miyake, T. Yasuo, Y. Akiyama, S. Taniguchi, M. Kadowaki, H. Kawamura, and T. Saitoh, *in* "Proceedings of the Fourth International Symposium on Solid Oxide Fuel Cells (SOFC-IV)" (M. Dokiya, O. Yamamoto, H. Tagawa, and S. C. Singhal, eds.), p. 100. The Electrochemical Society Inc., Yokohama, Japan, 1995.

53. B. C. H. Steele, *in* "Proceedings of the International Symposium of Solid Oxide Fuel Cells", Nagoya, Japan, 1989.

54. C. Bagger, P. V. Hendriksen, and M. Mogensen, *in* "First European Solid Oxide Fuel Cell Forum" (U. Bossel, ed.), Vol. 2, p. 691, Lucerne Switzerland, 1994.

55. K. Kendall and M. Prica, *in* "Proceedings of the First European Solid Oxide Fuel Cell Forum" (U. Bossel, ed.), Vol. 1, p. 163, Lucerne, Switzerland, 1994.

56. K. Kendall and T. W. J. Longstaff, *in* "Second European Solid Oxide Fuel Cell Forum" (B. Thorstensen, ed.), Vol. 1, p. 195, Oslo Norway, 1996.

57. K. Kendall, M. Prica, and T. Alston, *in* "Third European Solid Oxide Fuel Cell Forum" (P. Stevens, ed.), p. 113, Nantes-France, 1998.

# Chapter Two

## *The*
## *Solid Oxide Fuel Cell*
## *Interconnect/Current Collect*

# 2.1 Introduction to the SOFC interconnect/current collect

The primary purpose of the interconnect, also referred to as the bipolar plate or current collector, is to electrically connect solid oxide fuel cell (SOFC) units of cathode/electrolyte/anode in series and/or parallel to produce higher power outputs (*1*).

The material requirements of the interconnect are mainly dependent on the SOFC design. For example, the planar SOFC design operated at approximately 900°C requires the interconnect to serve not only as an electrical connector, but also as a structural support and gas manifold/separator. The material requirements imposed on the interconnect to meet this multi-functional role are rather severe. They include high electronic conductivity, low ionic conductivity, matching thermal expansion coefficient (TEC), chemical stability in oxidising and reducing environments, chemical compatibility with other cell components, mechanical strength (in self-supporting systems) and high density. As these requirements are so severe, the choice of materials is extremely limited (*2*). Obviously, at higher operational temperatures of 800-900°C, and with thermal cycling, material requirements are even more restricted due to increased reaction rates and greater TEC mismatches. A reduction in the operating temperatures can allow a wider range of materials to be selected (*3-6*). However, no matter what the SOFC design (tubular, planar, monolithic) or operating temperature, the interconnect material must be tailored to fit the requirements specific to the type of SOFC.

The two most widely adopted interconnect materials are perovskite doped compounds such as (La,Sr)$CrO_3$ or perovskite coated chromia forming alloys (*2*). A discussion of these two materials follows, relating their reactivity, conductivity, chemical stability/reactivity and design.

## 2.2 Perovskite-based materials

### 2.2.1 Structure of perovskites

Doped $LaCrO_3$ and $LaCoO_3$ belong to a class of materials known as the perovskites or pseudo-perovskites. The perovskites exhibit many useful properties including high electronic conductivity, high melting point, ferroelectricity and ferromagnetism (*7, 8*). The ideal perovskite structure shown in Fig. 2.1 is cubic, and is characterised by the simple formula $ABO_3$, where the A-site cation is co-ordinated with 12 oxygen ions and the B-site cation with 6 (*9*). With respect to perovskite interconnect materials, the A-site (La) can be substituted with an alkaline earth element (A = Sr, Ca), and the B-site (Cr) can be substituted with transition metals (B = Mn, Fe or Co) (*1*). The partial substitution of these alkaline earth or transition metals is known as doping.

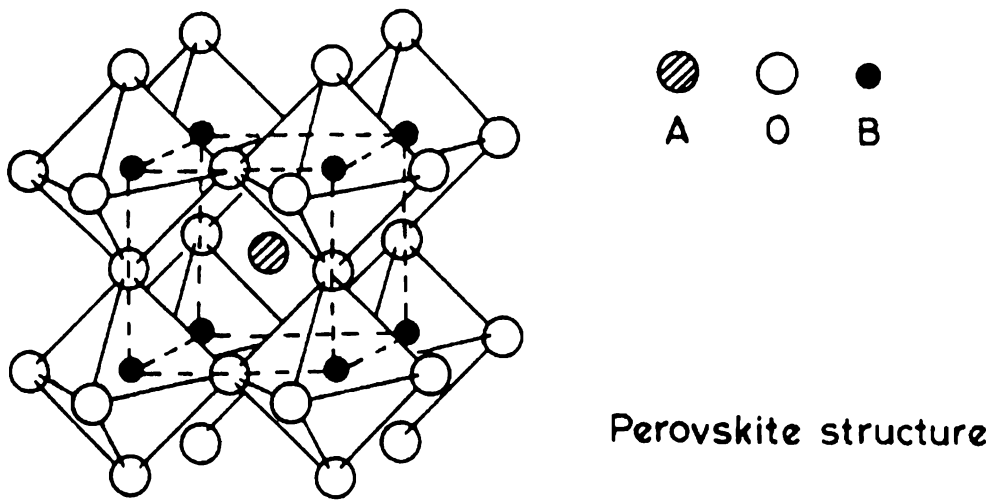


Fig. 2.1. The ideal cubic perovskite structure (*9*).

The ideal perovskite structure is cubic, but in practice many display lower symmetries arising from lattice distortions. Pure $LaCrO_3$, for example, exhibits three well defined polymorphs, namely orthorhombic, rhombohedral and cubic, with

transformations occurring from orthorhombic to rhombohedral at 250°C, and rhombohedral to cubic at 1650°C. Substitution of Sr on the A-site can lower the transformation temperature, stabilising the rhombohedral form at room temperature (*10*), while substitution of Ca can increase the transformation temperature (*11*). For $La_{1-x}Sr_xCoO_{3-\delta}$, the rhombohedral to cubic transition temperature has been shown to decrease with increasing Sr content (*12*).

Dopants can be substituted into the $ABO_3$ structure if charge balance is maintained and the ionic radii meet certain criteria. Charge balance is maintained by charge compensation (see Section 2.2.3), while ionic radii ($r$) of A, B and O site ions must satisfy the condition $0.75<t<1$ given below for the tolerance factor $t$ (*13*). Distortions are related to the value of the tolerance factor. For example, when $t$ is slightly less than unity a rhombohedral distortion can prevail, if $t$ is close to the lower limit of 0.75, distortions from cubic symmetry can be so great that the structure becomes orthorhombic (*9*).

Eq. 2.1 $$t = (r_A + r_O)\left[\sqrt{2}(r_B + r_O)\right],$$

where:

$t$ = the Goldschmidt tolerance factor,

$r_A$ = radius of the A ion,

$r_B$ = radius of the B ion,

$r_O$ = radius of the O ion.

The stability condition requires that $r_A > 0.90$Å and $r_B > 0.51$Å.

By substituting aliovalent or isovalent ions onto A or B positions, properties such as electrical conductivity, TEC, and chemical stability can be modified to meet material requirements for SOFC interconnects.

## 2.2.2 Defect chemistry in p-type perovskite oxides

It is important to understand the nature of the defect chemistry in perovskite materials. Variations in dopant, together with changes of temperature and $Po_2$ can transform the defect chemistry within perovskites, bringing about dramatic changes in conductivity, reactivity/chemical diffusion and TEC. An understanding of the defect chemistry in perovskites under varying conditions is essential to combat many of the problems encountered when utilising them in SOFC applications.

Perovskite-type oxides, such as $LaCrO_3$, containing trivalent transition metal ions on the B site and a trivalent rare earth on the A site are p-type conductors (*14*). Their native or majority defects are considered to be cation vacancies and electron holes; oxygen vacancies are considered the minority. Substitution, however, of acceptor dopants onto atomic sites of perovskite structures has been shown to lead to an increased oxygen ion vacancy concentration. Anderson (*7*) developed a simple defect chemistry model of the oxidation-reduction behaviour of these p-type perovskite oxides. Here, $RE_{1-x}A'_xBO_{3\pm\delta}$ is used to describe the p-type perovskite oxide. RE is a rare earth (typically a trivalent rare earth ion such as La), A is an acceptor dopant ($A^{2+}$ = $Sr^{2+}$ or $Ca^{2+}$) which can be substituted for $RE^{3+}$, and B is a transition metal ion (typically trivalent transition metal ions such as Cr, Mn, Fe or Co). Anderson (*7*) discusses and illustrates (Fig. 2.2) the general defect behaviour of $RE_{1-x}A'_xBO_{3\pm\delta}$ with reduction-oxidation. A plot of the oxygen content of $RE_{1-x}A'_xBO_{3\pm\delta}$ as a function of the oxygen activity at constant temperature (such that the temperature is high enough to maintain equilibrium) is given.

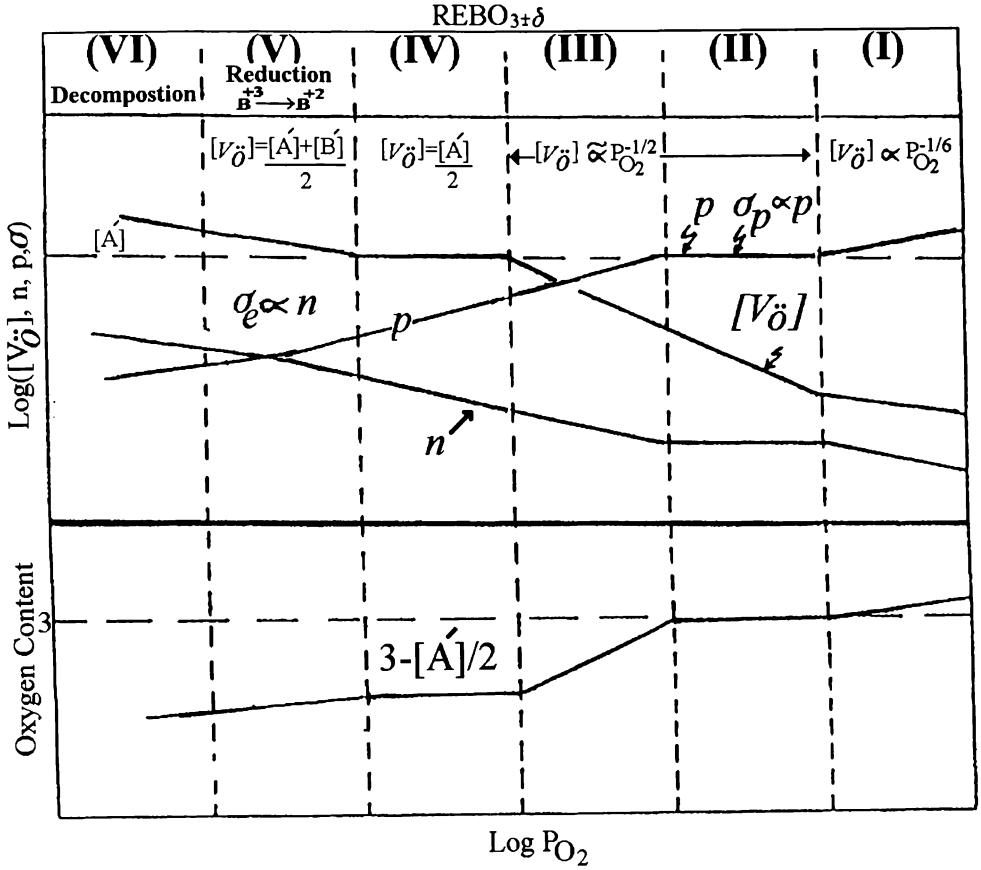


Fig. 2.2. Carrier concentration, oxygen content and electrical conductivity as a function of oxygen activity of $REBO_3$ (*7*).

This plot is divided into six oxygen activity regions, where each region contains the dominant defect considered to be present (and associated neutrality condition). Anderson (*7*) stipulates these divisions are only a simplification and may not represent real behaviour. Anderson (*7*) assumed that:

- p-type disorder prevails in nonstoichiometric $REBO_3$;
- defects are fully ionised;
- the ratio of large cations to small cations is unity;
- defect association does not occur;
- acceptor dopant $A^{2+}$, for example Sr or Ca, substitutes for $RE^{3+}$ on a normal lattice site.

By applying the Kröger-Vink notation (*15*), see Appendix A, the Schottky reaction of the undoped $REBO_3$ compound is given by

Eq. 2.2 $$nil \leftrightarrow V_{RE}''' + V_B''' + 3V_O^{\bullet\bullet}.$$

The intrinsic electronic defects are

Eq. 2.3 $$nil \leftrightarrow e' + h^{\bullet}.$$

It is assumed that cation stoichiometry remains constant unless a second phase has formed. Thus, $[V_{RE}'''] = [V_B''']$ throughout the entire single-phase region. The p-type nonstoichiometric reaction is shown below by

Eq. 2.4 $$\frac{3}{2}O_2 \leftrightarrow V_{RE}''' + V_B''' + 3O_O^X + 6h^{\bullet}.$$

When an acceptor dopant, $A_{RE}'$, containing one effective negative charge is added, the extra charge can be compensated for by oxidation of $B^{3+}$ to $B^{4+}$ or the formation of oxygen vacancies. This leads to the following situation (where $p = [h^{\bullet}]$)

Eq. 2.5 $$2[V_O^{\bullet\bullet}] + p = 6[V_B'''] + [A_{RE}'].$$

A high concentration of defects can be generated by the substitution of acceptor dopants onto either the RE or B sites. The concentration of these defects is shown in Fig. 2.2 to change with varying $Po_2$ and, as described previously, are divided into six separate regions. These regions are discussed below.

Region I: native nonstoichiometry is prevalent (cation vacancies), where the acceptor concentration, $[A_{RE}'] < [V_B''']$ and the neutrality becomes

Eq. 2.6 $$p = 3\left[V_{RE}'''\right] + 3\left[V_B'''\right] = 6\left[V_B'''\right].$$

Region II: With a decrease in oxygen activity, both $\left[V_B'''\right]$ and $\left[V_O^{\bullet\bullet}\right]$ are smaller than the impurity content, the neutrality condition is described by

Eq. 2.7 $$p = \left[A_{RE}'\right].$$

Region III: With further decrease in oxygen activity, oxygen deficiency starts to occur, where electrical conductivity declines and weight loss is observed. This loss of weight is ascribed to the reversible formation of oxygen vacancies which are inclined to compensate the acceptors. The neutrality condition is now

Eq. 2.8 $$p = \left[A_{RE}'\right] - 2\left[V_O^{\bullet\bullet}\right].$$

Region IV: With additional decrease in oxygen activity, no oxygen vacancy dependence on oxygen activity is seen. The neutrality condition becomes

Eq. 2.9 $$2\left[V_O^{\bullet\bullet}\right] = \left[A_{RE}'\right].$$

Region V: Here it is assumed that $B^{3+}$ to $B^{2+}$ reduction predominates (see below), such that dissociation does not occur until region VI.

Eq. 2.10 $$2B_B^x + O_O^x \leftrightarrow 2B_B' + V_O^{\bullet\bullet} + \frac{1}{2}O_2.$$

The reduction reaction above dominates, where the oxygen vacancies increase, greater than those associated with the acceptor alone, such that the neutrality is

Eq. 2.11 $$\left[B_B'\right] = n = 2\left[V_O^{\bullet\bullet}\right].$$

Region VI: This region is defined by the oxygen activity region where dissociation occurs, the limit where oxygen vacancies cease to exist.

2.2.2.1 Defect Models for $(La,Sr)CrO_{3-\delta}$, $(La,Ca)CrO_{3-\delta}$ and $La_{1-x}Sr_xCoO_{3-\delta}$.

The simple point defect model has been applied to $(La,Sr)CrO_{3-\delta}$, $(La,Ca)CrO_{3-\delta}$ (*16, 17*) and $La_{1-x}Sr_xCoO_{3-\delta}$ (*12*). A generalised condition can be written as

Eq. 2.12 $$\left[A_{La}'\right] = \left[B_B^{\bullet}\right] + 2\left[V_O^{\bullet\bullet}\right].$$

When the B site ion is Cr, A is either Ca or Sr, and when the B site ion is Co, A is usually Sr. The equilibrium between oxygen in the gas phase and the point defects can be written as

Eq. 2.13 $$O_O^x + 2B_B^{\bullet} \leftrightarrow \frac{1}{2}O_2(g) + V_O^{\bullet\bullet} + 2B_B^x.$$

For $(La,Sr)CrO_{3-\delta}$ and $(La,Ca)CrO_{3-\delta}$ the $Po_2$ dependency has been interpreted using the simple defect model (*16, 17*). For $(La,Sr)CrO_{3-\delta}$ under high $Po_2$ conditions ($Po_2$ above $10^{-10}$ atm.), the reaction given in Eq. 2.13 moves to the left, where the concentration of oxygen vacancies can be neglected in comparison to the $Cr^{4+}$; i.e., $\left[Cr_{Cr}^{\bullet}\right] >> \left[V_O^{\bullet\bullet}\right]$, such that the neutrality condition can be simplified to

Eq. 2.14 $$\left[Sr_{La}'\right] = \left[Cr_{Cr}^{\bullet}\right].$$

Here, $\left[Cr_{Cr}^{\bullet}\right]$ is considered to be determined only by the dopant concentration, not $Po_2$ or temperature. Dropping below a critical value of $10^{-10}$ atm., oxygen vacancies are generated at the expense of electron holes, such that the charge imbalance due to Sr is increasingly compensated for by oxygen vacancy formation. In this situation the condition given in Eq. 2.12 should be applied. A similar description can be used for $(La,Ca)CrO_{3-\delta}$ (*16*), here the critical value at which oxygen vacancies are generated is slightly higher, around $10^{-8}$ atm.

If no defect associations occur, the simple defect model can be applied to $La_{1-x}Sr_xCoO_{3-\delta}$. Due to Sr doping, $Co^{4+}$ ions and oxygen vacancies are formed by charge compensation. For $La_{1-x}Sr_xCoO_{3-\delta}$, where $x \leq 0.3$, the concentration of $Co^{4+}$ ions was shown to increase linearly with increased Sr content up to a maximum value of 0.4. Beyond 0.4, $Co^{4+}$ concentration decreased with increasing dopant addition. The decrease was attributed to oxygen vacancies being formed at the expense of $Co^{4+}$ ions. The formation of these oxygen vacancies was shown to be increasingly prominent at high temperature and low $Po_2$ (*12*).

### 2.2.2.2 Defect association

Anderson (*7*) used the simple point defect model (assumes no defect interaction) to describe the defect behaviour or nonstoichiometry of perovskites. As highlighted by Van Roosmalen et al. (*18*), however, interaction between point defects can occur when defect concentrations exceed 0.1 at%. Van Roosmalen et al. (*18*) proposed that point defects can interact and form extended defects and microdomains; which in turn can interact (depending on defect concentration) and form new highly defective ordered phases. The formation of these defects in $LaMO_{3-\delta}$ (M = Cr, Co, Mn, Fe and Ni) was explained by Van Roosmalen et al. (*18*) using a defect model (cluster model). As described in Eq. 2.15, when oxygen is lost from $LaMO_{3-\delta}$, an oxygen vacancy is formed. There is also an associated reduction of two $M^{3+}$ ions to two $M^{2+}$ ions.

Eq. 2.15 $$O_O^x \leftrightarrow V_O^{\bullet\bullet} + \frac{1}{2}O_2 + 2e'.$$

Upon formation of the oxygen vacancy two electrons are left, reducing $M^{3+}$ to $M^{2+}$,

Eq. 2.16 $$2M_M^x + 2e' \leftrightarrow 2M'_M.$$

Removal of oxygen from the lattice leaves a net positive charge of 2+. The reduction of $M^{3+}$ to $M^{2+}$ results in the oxygen vacancy being bound by charge interaction to two $M^{2+}$ ions, forming a $M^{2+} - V_O^{\bullet\bullet} - M^{2+}$ defect cluster (extended defect) as described below

Eq. 2.17 $$2M_M^x + O_O^x \leftrightarrow (M^{2+} - V_O^{\bullet\bullet} - M^{2+}) + \frac{1}{2}O_2.$$

If the concentration of these extended defects is too high then it is possible for them to react forming micro-domains, which in turn (depending on temperature) can form new ordered phases. The $M^{2+} - V_O^{\bullet\bullet} - M^{2+}$ defect cluster can be regarded as a building block for the formation of highly defective phases.

Defect structures of the p-type perovskites are usually described using the ideal dilute solution model (*12*), where it is assumed defects are single, unassociated and are randomly distributed in the lattice with concentrations less than 1% (as described previously, Anderson (*7*) applied this model). With defect concentrations greater than 1% more complex models of defect chemistry are needed. These involve proposed defect associations, where defect complexes and clusters (extended defects) are formed, and the formation of microdomains or shear structures with ordered defects (*12*).

Petrov et al. (*12*) described a possible neutral defect complex as $(Sr'_{La}V_O^{\bullet\bullet}Sr'_{La})^x$, proposing that with an increased concentration these complexes may order, Eq. 2.18,

forming microdomains or slabs consisting of intermediate, perovskite-related phases with lowered oxygen content.

Eq. 2.18 $$n(Sr'_{La}V_O^{\bullet\bullet}Sr'_{La})^x \rightarrow (Sr'_{La}V_O^{\bullet\bullet}Sr'_{La})_n^x.$$

## 2.2.3 Electrical conductivity of p-type perovskites

One of the primary requirements for a SOFC interconnect/current collect is high electronic conductivity. Simple p-type conducting perovskites such as $LaCrO_3$ usually have a relatively poor electronic conductivity, however, when dopants like Ca, Sr and Mg are introduced, the conductivity is notably improved. For example, $LaCrO_3$ has a conductivity of less than 1 S $cm^{-1}$ in air at 1000°C (*19*) while $La_{0.7}Ca_{0.3}CrO_3$ exhibits a conductivity of 60 S $cm^{-1}$ under the same conditions (*16*).

The improvement in conductivity for $LaCrO_3$ by addition of the dopant arises because the dopant invokes a charge compensation mechanism in the lattice, which in turn induces the formation of charge carriers, and leads to improved conductivity.

Two charge compensation mechanisms of relevance to p-type conducting perovskites exist; electronic charge compensation, which involves the formation of small polarons, and ionic compensation, where oxygen vacancies are formed. The mechanisms present or dominant for doped $LaCrO_3$ are in part determined by the partial pressure of $O_2$. In air, the dominant mechanism is electronic charge compensation, which leads to p-type conductivity. As the partial pressure of $O_2$ drops there is a shift in the mechanism from electronic conductivity, through mixed electronic/ionic, to ionic conductivity.

In general, the conductivity of p-type perovskites can be explained in terms of carrier concentrations and carrier mobility, which are directly related to the type and concentration of the dopant.

In the following discussion, only the electronic conductivity in air of p-type perovskites is considered, as the studies described in this thesis were limited to the use of these materials in air. A description, however, of the defect chemistry/conductivity in varying $Po_2$ environments is given in Section 2.2.2. Detailed below is a discussion on the electrical conductivity of p-type perovskites, with particular emphasis on the types of doping available, the electronic charge mechanism, and the effect that temperature, dopant concentration and dopant type have on electrical conductivity. Band-like and small polaron models are also used to explain the different conductive nature of the various examples presented.

### 2.2.3.1 Dopants

The purpose of the dopant is to introduce charge carriers into the perovskite lattice. Since the perovskite ($ABO_3$) has two cation sites, substitution can be made for either the A or B cation. Of the common dopants used with $LaCrO_3$, $Ca^{2+}$ and $Sr^{2+}$ can substitute onto the A site because their ionic radii (both approximately 132 pm) are similar to $La^{3+}$, while $Mg^{2+}$ can occupy the B site because its ionic radius (86 pm) more closely matches $Cr^{3+}$ (*20*). The conductivity of various doped perovskites is given in Table 2.1.

Table 2.1. The electrical conductivity of various perovskite materials in air.

| Composition | Conductivity S $cm^{-1}$ | Temperature (°C) | Ref. |
|---|---|---|---|
| $LaCrO_3$ | 0.8 | 1000 | (*19*) |
| $La_{0.9}Ca_{0.1}CrO_3$ | 12.1 | 1000 | (*20*) |
| $La_{0.8}Ca_{0.2}CrO_3$ | 40.0 | 1000 | (*20*) |
| $La_{0.9}Sr_{0.1}CrO_3$ | 8.5 | 1000 | (*20*) |
| $La_{0.8}Sr_{0.2}CrO_3$ | 36.6 | 1000 | (*20*) |
| $LaCoO_3$ | 950 | 950 | (*21*) |
| $La_{0.8}Sr_{0.2}CoO_3$ | 1270 | 950 | (*21*) |

Generally, the conductivity of $LaCrO_3$ at elevated temperatures increases with increasing dopant concentration (*16, 20*), as shown in Fig. 2.3. This is because increased dopant concentration results in increased charge carrier or small polaron concentration.

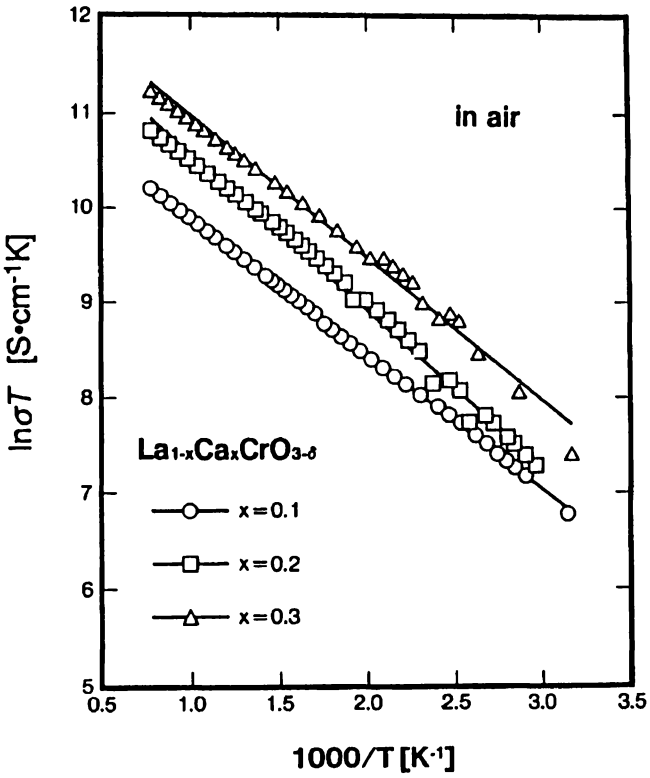


Fig. 2.3. Electrical conductivity as a function of dopant concentration and temperature for $La_{1-x}Ca_xCrO_{3-\delta}$ (x = 0.1-0.3) (*16*).

2.2.3.2 Electronic charge compensation mechanism

In air, the addition of acceptor dopants leads to a charge imbalance in the $ABO_3$ type lattice that is rectified by an electronic charge compensation mechanism. This mechanism can be explained using Ca doped $LaCrO_3$ as an example (*16*). In order to maintain electroneutrality, the substitution of Ca onto the La sites causes some of the $Cr^{3+}$ ions to be oxidised to $Cr^{4+}$. This transformation occurs by an electronic charge compensation mechanism that can be written as

Eq. 2.19 $$(1-x)LaCrO_3 + xCaO \longrightarrow La_{1-x}Ca_xCr^{3+}_{1-y}Cr^{4+}_yO_{3-\delta} + \frac{\delta}{2}O_2.$$

Using Kröger Vink notation (*15*), the equilibrium between the surrounding atmosphere and the defect species is given by

Eq. 2.20 $$\frac{1}{2}O_2 + V_O^{\bullet\bullet} + 2Cr_{Cr}^{x} \leftrightarrow O_O^{x} + 2Cr_{Cr}^{\bullet}.$$

In air, the dominant charge compensation mechanism present is due to oxidation of $Cr^{3+}$ to $Cr^{4+}$ (formation of $Cr^{\bullet}_{Cr}$ holes) (*16, 20*). Thus, if electronic compensation is considered the only compensation mechanism present in air, then δ is zero and x is equal to y, hence $[Cr^{\bullet}_{Cr}]$ is equal to $[Ca'_{La}]$ (the right hand side of Eq. 2.20 dominates). This is observed for Sr doped $LaCrO_3$ up to a critical $Po_2$ of $10^{-10}$ atm., when oxygen vacancies are then generated at the expense of electron holes (*17*). The holes $[Cr^{\bullet}_{Cr}]$ created, due to the $Cr^{3+}$ to $Cr^{4+}$ transformation, leads to p-type conductivity. The change in oxidation state forces a change in ionic radius of the $Cr^{3+}$ ion, producing polarisation/distortion of local areas of the lattice, such that charge is trapped. This combination of ion, polarisation/distortion and trapped charge is known as a small polaron. The term "small polaron" is used to describe the association between the lattice distortion and the charge carrier. The small polarons can jump to equivalent sites in the lattice by a temperature activated hopping process.

For small polaron hopping to occur, localisation and delocalisation are almost equally favoured such that activation energy is required for the electron to jump via a thermally activated hopping mechanism. This process can be described as an electron transfer between 2 transition metal ions via the bridging oxygen.

In a discussion by Karim et al. (*22*) the hole is considered trapped in a potential well created by the distortion of the surrounding lattice. Hopping of the polaron to a neighbouring site occurs when thermal fluctuations reduce the depth of the potential well, and create an empty well on a neighbouring site. Because the charge carrier is

localised, the band model for conduction is not considered appropriate. An insulator results when there is almost no orbital interaction (totally localised), such that no charge is transferred. When, however, the overlap of the orbitals is sufficient to delocalise the charge, metallic-type conduction occurs (large polaron formation) (*23, 24*). The localisation/delocalisation is illustrated in Fig. 2.4, using a configuration co-ordinate model (*23*).

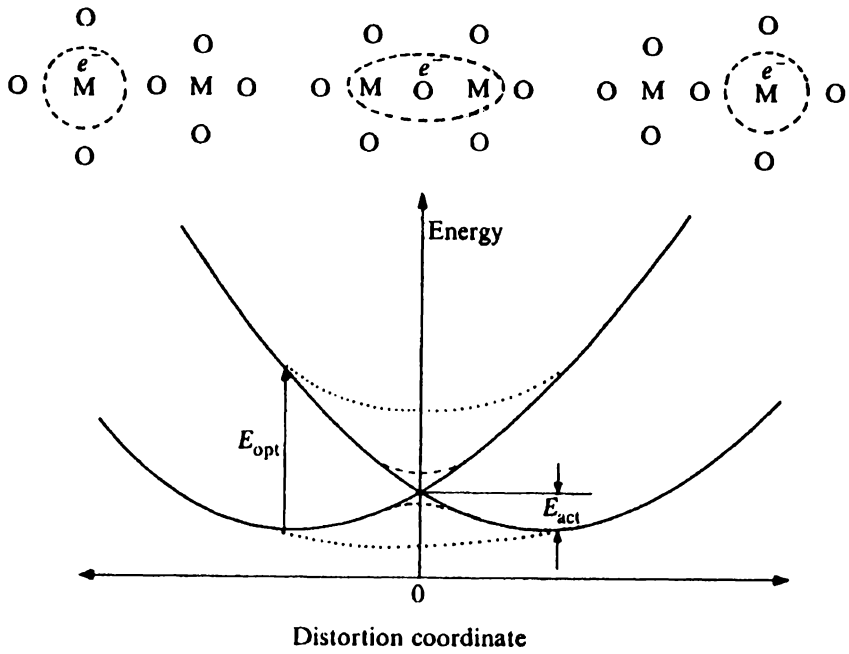


Fig. 2.4. Configuration co-ordinate model (*23*).

### 2.2.3.3 Temperature dependence of Sr or Ca doped $LaCrO_3$

The localised small polarons are able to jump to equivalent sites via a phonon assisted (thermally assisted) hopping mechanism. In essence, an electron transfer occurs between two Cr ions. The $Cr^{3+}$-$Cr^{4+}$ system can be considered as a two $Cr^{3+}$ system with a hole, where the two sites are momentarily identical such that the hole can "hop" with an activation energy, $E_a$, to an equivalent site. Thus if the temperature is increased, the small polaron drift mobility will increase, such that the mobility increases, in an Arrhenius manner. The carrier mobility is thermally activated, not the

carrier concentration. This Arrhenius relationship is given by Eq. 2.21. $E_a$ can be obtained from the gradient of plots of Ln ($\sigma T$) versus $1/T$.

Eq. 2.21 $$\sigma(T) = \frac{A}{T}\exp(-E_a/kT),$$

where: $k$ = Boltzmann constant,
$A$ = pre-exponential factor,
$T$ = absolute temperature (K),
$E_a$ = activation energy.

$LaCrO_3$ materials doped with Sr (*17, 25*) or Ca (*16*) are considered to obey the small polaron mechanism, because their Arrhenius plots are linear (see Fig. 2.3). Studies by Karim et al. (*22*) on $La_{1-x}Sr_xCrO_3$ (x = 0-0.4) using direct carrier mobility measurements showed their electrical conductivity to be consistent with the small polaron hopping model because:

- the carrier concentration was shown to be independent of temperature (Seebeck coefficient was constant with increasing temperature);
- the carrier concentration was dependent on dopant concentration (Seebeck coefficients' magnitude varied with dopant addition);
- the activation energy decreased with increasing carrier concentration (overlap of polaron clouds);
- and the magnitude and temperature dependence of mobility was confirmed to be consistent with the small polaron theory.

#### 2.2.3.4 Doped Lanthanum Cobaltites

Doped lanthanum cobaltite may be used as a coating on the metal interconnect to improve the electrical contact with the cathode in SOFCs. In comparison to Ca and Sr doped $LaCrO_3$, doped $LaCoO_3$ possesses a much higher conductivity in air (of the

order of a 10 fold increase, see Table 2.1). Koc et al. (*26*) observed that $LaCoO_3$ conducts via the diffusion of small polarons, where electronic charge compensation occurs, transforming $Co^{3+}$ to $Co^{4+}$ (*26*). Petrov et al. (*27*) investigated $La_{1-x}Sr_xCoO_{3-\delta}$ (x = 0.0-0.6) and found anomalies in conductivity, see Fig. 2.5. For $x \leq 0.2$, conductivity initially increased with increasing temperature then decreased with further increase in temperature. Petrov et al. (*12*) suggested this represented a transition from semiconductor/small polaron behaviour to metallic conduction. For $x \geq 0.3$ conductivity decreased from room temperature up, suggesting metallic conduction. Furthermore, when the electrical conductivity of $La_{1-x}Sr_xCoO_{3-\delta}$ (x = 0.0-0.6) was measured at constant temperature, conductivity was found to show a maximum at x = 0.4. The increased Sr concentration up to x = 0.4 was shown to improve conductivity, while further dopant addition resulted in decreased conductivity.

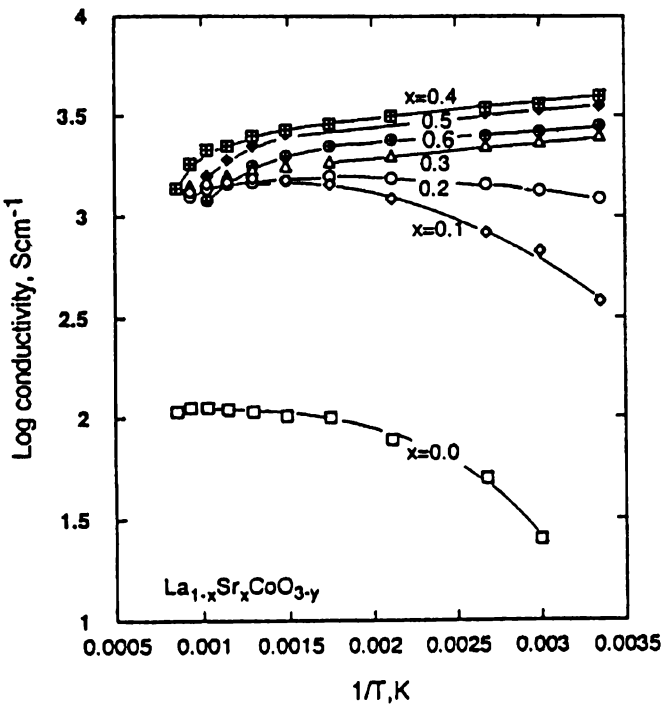


Fig. 2.5. Electrical conductivity of $La_{1-x}Sr_xCoO_{3-\delta}$ (x = 0.0-0.6), at $Po_2$ = 0.21 atm., as a function of the reciprocal of absolute temperature (*12*).

The decrease in conductivity with temperature is explained by Petrov et al. (*12*) using the metallic conduction and semiconductor models. For the metallic conduction model proposed, they applied the itinerant model, where the close proximity in

energy states between high-spin ($t_{2g}^5 e_g^1$) and low-spin ($t_{2g}^6 e_g^0$) $Co^{3+}$ ions is used to explain how electron hopping between two spin states gives rise to a charge-transfer state. The Co ions are in the diamagnetic low spin state at decreased temperatures. However with increased temperature, a transformation to the high spin configuration occurs. With increased temperature $e_g$ electrons are inclined to form a Co-O $\sigma^*$ band structure (delocalised/itinerant) and thus exhibit metallic type conductivity. The localised and itinerant (band) structures proposed are shown in Fig. 2.6. The itinerant model closely mirrors the classic band-gap model used to describe electronic conduction in metals.

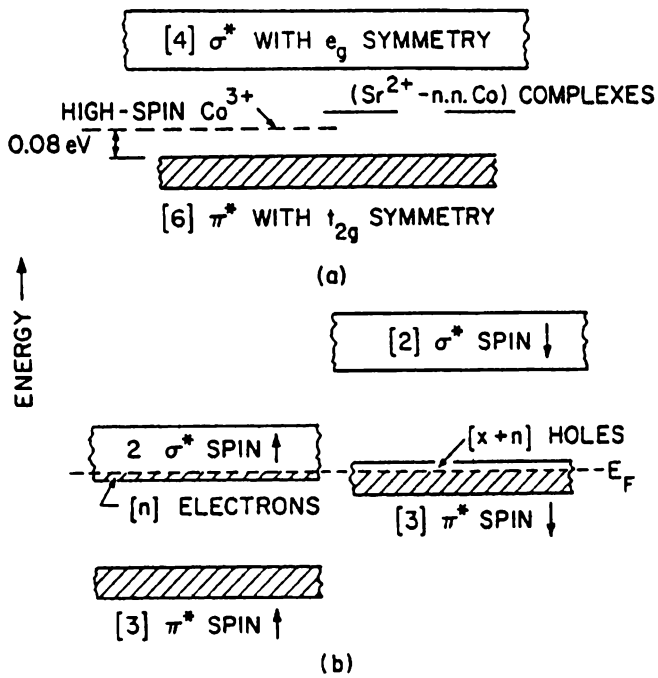


Fig. 2.6. Localised and itinerant (band) structure models (*28*).

A semiconductor-like conductivity model was also proposed by Petrov et al. (*12*) to explain the reduction in conductivity of $La_{1-x}Sr_xCoO_{3-\delta}$ with increased temperature and increased Sr content. In essence, the concentration of electronic charge carriers decreases with increasing temperature and increasing Sr content due to the preferential formation of oxygen vacancies at higher values of x and higher temperatures. Oxygen vacancies are considered to be formed at the expense of $Co^{4+}$ in $La_{1-x}Sr_xCoO_{3-\delta}$.

## 2.2.4 Stability/Reactivity of p-type perovskite materials

It is important to understand the stability and reactivity of the perovskite-based interconnect materials with other cell components under co-firing (SOFC components sintered together in a single step (*29*)) and operating conditions. The stability of the perovskites are dependent on their composition (dopant species/concentration and stoichiometry), and the temperature and atmosphere under which they operate (*30-34*).

Typically, dopants are added to modify electrical conductivity, TEC and sintering temperature. The addition of these dopants can have a major effect on their reactivity/stability. For example, the doping of Ca into $LaCrO_3$ is used to improve sinterability of the perovskite when co-firing with other cell components such that firing temperatures can be reduced. The addition of dopants such as Ca into $LaCrO_3$ can lead to the formation of second phases that can migrate during co-firing or during operation to react with SOFC components (*35*). The second phases formed can have very low conductivity (*32*) and different TEC from the cell components (*36*). The formation of these second phases can lead to stress build up within the stack and/or decreased cell performance.

In addition, chromium deficiency in doped $LaCrO_3$ can be disastrous. For example chromium deficient Mg, Sr (*30*) or Ca (*37*) doped $LaCrO_3$ have been shown to precipitate $La_2O_3$ in air. The presence of $La_2O_3$ (which is hydroscopic in nature), can lead to the disintegration of the doped $LaCrO_3$.

An overview of the reactivity and stability of doped $LaCrO_3$ under various conditions and with other cell components is highlighted in Table 2.2. This Table is intended to highlight the complex nature of the reactivity and stability of doped $LaCrO_3$ materials. For brevity, discussions are limited to the reactivity of doped $LaCrO_3$ with YSZ, and to the reactivity of doped $LaCrO_3$ with the metal interconnects (note, doped $LaCrO_3$ is often used as a protective/conductive coating on the metallic interconnect/current collect see Section 2.3).

A useful study on the thermodynamic stabilities of perovskite oxides by Yokokawa et al. (*38*) is also discussed. Here, Yokokawa et al. (*38*) used thermodynamic considerations to rationalise perovskites stabilities.

### 2.2.4.1 Stability/Reactivity of perovskites with the electrolyte

As described by Mori et al. (*36*) the doped $LaCrO_3$ interconnect/current collect can come into contact with the YSZ electrolyte in certain designs of SOFC. If reactions occur, then it is important to understand the nature of these reactions such that the correct material selection can be achieved.

Various studies have focused on understanding the stability of the current collect with the YSZ. As, for example described in Table 2.2, Mori et al. (*36*) showed powder mixtures of Sr and Mg doped $LaCrO_3$ with YSZ reacted to form, $SrZrO_3$ and $La_2Zr_2O_7$ respectively. No reaction products were however detected for $(La,Ca)CrO_3$. Mori et al. (*36*) determined the solubility limits of the constituent oxides in YSZ to explain the difference in reactivity. The solubility limit of $La_2O_3$ was higher than SrO, and thus more $La^{3+}$ dissolved into the YSZ than $Sr^{2+}$. This left excess SrO in the chromite to react with the YSZ, forming $SrZrO_3$. Similarly, MgO and CaO had higher solubility limits than $La_2O_3$, so excess $La^{3+}$ left in the chromite (after diffusion of Mg and Ca into the YSZ), reacts with the YSZ to form $La_2Zr_2O_7$. All elements however were found to diffuse into YSZ at 1500°C.

Carter et al. (*31*) investigated the reactivity of $(La,Ca)CrO_3$ and $CaCrO_4$ (an associated liquid phase present in $(La,Ca)CrO_3$), with YSZ, finding the chemical interaction was due to the presence of a Ca-Cr-O liquid phase emanating from $(La,Ca)CrO_3$. Carter et al. (*31*) stated that $CaCrO_4$ has approximately the same composition as the transient liquid phase in $(La,Ca)CrO_3$, therefore reaction products between YSZ and $CaCrO_4$ could be related to those of the transient liquid phase. The authors reacted $La_{0.76}Ca_{0.24}CrO_3$ (containing approximately 5 mol% $CaCrO_4$) with YSZ (Table 2.2), and found Ca had diffused into the YSZ. Also, when a powder mixture

containing $CaCrO_4$ 1.36:1 YSZ was annealed (see Table 2.2), $CaZrO_3$, $CaCr_2O_4$, Ca in YSZ and Y-Cr-O were found.

In addition, plates of $CaCrO_4$ or sintered $La_{0.70}Ca_{0.36}CrO_3$ with YSZ were annealed in air at 1200°C for 100 h. A Ca-Cr-O liquid reacted through the entire thickness of the YSZ plate for both $CaCrO_4$ and $La_{0.70}Ca_{0.36}CrO_3$. $CaZrO_3$ was formed along the grain boundaries, digesting the YSZ grains into a $CaZrO_3$ matrix. Y-Cr-O grains were also shown to form at the original YSZ free surface. A simplified reaction as proposed by Carter et al. (*31*) is given below

Eq. 2.22 $$2CaCrO_4 + ZrO_2 \rightarrow CaCr_2O_4 + CaZrO_3 + \frac{3}{2}O_2 .$$

The simplified reaction in Eq. 2.22 becomes more complicated with the presence of $Y^{3+}$ in $ZrO_2$. However Eq. 2.22, does illustrate the need to develop (La,Ca)$CrO_3$ that contains no residual $CaCrO_4$ or high Ca content compositions, as they will react to form $CaZrO_3$. Carter et al. (*31*) reports the difficulty of co-firing (La,Ca)$CrO_3$ with YSZ in the presence of Ca-Cr-O liquid phase and specifies the need to eliminate Ca-Cr-O liquid phase in sintered (La,Ca)$CrO_3$ to achieve compatibility with YSZ.

Table 2.1. Literature survey of the reactivity and stability of perovskite-based interconnect materials and associated phases.

| Reactants | Reaction conditions | Phase and chemical analysis | Ref. |
|---|---|---|---|
| 7.5YSZ/$La_{1-x}Sr_xCrO_3$ (x = 0.1, 0.2) | powder mixture, 1500°C 168 h in air | no reaction | (*39*) |
| 7.5YSZ/$La_{0.7}Sr_{0.3}CrO_3$ | powder mixture, 1000°C 500 h in air | $SrZrO_3$ | (*39*) |
| 7.5YSZ/$La(Cr_{0.8}Mg_{0.2})O_3$ | powder mixture, 1500°C 96 h in air | $La_2Zr_2O_7$ | (*39*) |
| 8YSZ/$La_{1-x}Ca_xCrO_3$ (x = 0.1-0.3) | powder mixture, 1500°C 168 h in air | no reaction | (*39*) |
| 8YSZ/$La_{0.76}Ca_{0.24}CrO_3$ + ~ 5 mol% $CaCrO_4$ | pellet/pellet interface, 1000°C 100 h in air | Ca in YSZ | (*31*) |
| YSZ/$CaCrO_4$ | pellet/pellet interface, 1200°C 24 h in 1% $H_2/N_2$ | $CaZrO_3$, Y-Cr-O, Ca in YSZ, $CaCr_2O_4$ | (*31*) |
| $La_{0.8}Sr_{0.2}CrO_3$/Ni-YSZ | pellet/pellet interface, 1400°C 12 h in 1% $H_2/N_2$ | no reaction | (*40*) |
| (La,Ca)$CrO_3$/Ni-YSZ | pellet/pellet interface, 1400°C 12 h in 1% $H_2/N_2$ | Ca in YSZ | (*40*) |
| $La(Cr_{0.8}Mg_{0.2})O_3$/Ni-YSZ | pellet/pellet interface, 1400°C 12 h in 1% $H_2/N_2$ | $La(Cr_{1-x}Ni_x)O_3$, Mg in YSZ | (*40*) |
| $Ca_5(CrO_4)_3OH$/LSM | powder mixture, 900°C in air saturated with $H_2O$ | no reaction | (*32*) |
| $Ca_5(CrO_4)_3OH$/Ni-YSZ | powder mixture, 1000°C in $N_2/H_2/H_2O$ | $CaZrO_3$ | (*32*) |

Other authors (*29, 41*) have investigated the (La,Ca)$CrO_3$ system, suggesting Ca-Cr-O melts to be a major problem. For example, the migration of Ca into the YSZ during co-firing can lead to a low density (La,Ca)$CrO_3$ interconnect (*29*). Saki et al. (*41*) studied chemical degradation on the surface of (La,Ca)$CrO_3$ and (La,Sr)$CrO_3$, under simulated SOFC operating conditions. The authors found that $Ca_m(CrO_4)_n$ and $SrCrO_4$ migrated and decomposed on their respective surfaces that were directly exposed to fuel gas or air. The degree of degradation was dependent on the locality and amount of chromate species. Saki et al. (*34*) also revealed that the preparation method and impurities ($SiO_2$) can determine the type of second phases present in the sample.

### 2.2.4.2 Stability/Reactivity of interconnect perovskites with the metal interconnect

Few studies have been performed on the stability of the perovskite coatings applied to the metal interconnect. Schmidt et al. (*21*), however, showed that when $LaCrO_3$ or $LaCoO_3$ were doped with Sr, $SrCrO_4$ would form at the interface between the perovskite coating and the Cr5Fe1$Y_2O_3$ metal interconnect. The formation of $SrCrO_4$ was considered to increase the contact resistance of the coating. Additionally when $LaCoO_3$ was applied to the metal, $CoCr_2O_4$ was observed to form. The formation of $CoCr_2O_4$ was considered to lead to the improved adherence of the coating to the metal.

### 2.2.4.3 Thermodynamic stabilities of perovskite oxides

Thermodynamic analysis, performed by Yokokawa et al. (*38*), determined that the stability of perovskite oxides could be understood in terms of their valence stability and the stabilisation energies from their constituent binary oxides. These concepts are discussed below.

The stabilisation energy ($\delta$) of perovskites ($ABO_3$) can be calculated from the enthalpy change for formation ($\Delta_f H^o$) of the binary oxides ($AO_n$, $BO_m$),

Eq. 2.23 $$\delta(ABO_3) = [\Delta_f H^o(ABO_3) - \{\Delta_f H^o(AO_n) + \Delta_f H^o(BO_m)\}].$$

Furthermore, the stabilisation energy and Goldschmidts tolerance factor (which can be evaluated simply from the ionic radii, see Section 2.2.1) correlate well. The perovskite tolerance factor (*tp*) describes the geometrical matching between ions in a perovskite lattice. When the match is ideal (*tp* = 1), the perovskite is cubic with a large stabilisation energy. A plot of stabilisation energies against their respective tolerance factors yielded a linear correlation. This linear relation between stabilisation energy and tolerance factor can be achieved for $A^{3+}$-$B^{3+}$, $A^{3+}$-$B^{4+}$ and $A^{3+}$-$B^{5+}$ perovskites. The stabilisation energy can be used to characterise thermodynamically, the chemical stability of perovskites under varying chemical conditions (*38*).

The stabilisation energy is calculated (A = lanthanide), Eq. 2.24, by using the perovskite tolerance factor (*tp*), derived from the 12 co-ordinate ionic radii of the A ions as described in Section 2.2.1.

Eq. 2.24 $$\delta(ABO_3) = 2[-45 + 360(1 - t_p)].$$

In addition, the thermodynamic stability of transition metal binary oxides $MO_m$ can be determined by the relative stability of the valence states. For multi-component systems (formation of perovskites $ABO_3$), however, the averaged valence value alone cannot provide correct information on the valence stability. Therefore the change in valence stability with formation of double oxides from their binary oxides can be understood only in terms of the valence stability in the binary oxides and the stabilisation energy. These concepts are discussed here using the reduction reaction (Eq. 2.25) of $LaBO_3$ (B = Co, Ni).

Eq. 2.25 $$LaBO_3 = \frac{1}{2} La_2O_3 + BO + \frac{1}{4} O_2(g).$$

Neglecting the formation of $La_2BO_4$ and $La_4B_3O_{10}$ the reaction can be divided into two steps described in Eq. 2.26 and Eq. 2.27. The Gibbs free energy change, $\Delta_r G^o$, can be calculated for the two reactions.

Eq. 2.26 $$LaBO_3 = \frac{1}{2} La_2O_3 + \frac{1}{2} B_2O_3,$$

$$\text{where, } \Delta_r G^o = \delta(ABO_3) = 2[-45 + 360(1 - t_p)],$$

Eq. 2.27 $$\frac{1}{2} B_2O_3 = BO + \frac{1}{4} O_2(g),$$

$$\text{where, } \Delta_r G^o = \Delta(B^{3+}, B^{2+}).$$

The first reaction, Eq. 2.26, can be understood with respect to the stabilisation energy. Eq. 2.27 can be characterised with respect to relative valence stability $\Delta(B^{3+}, B^{2+})$ (valence stability in the binary oxides) between $B^{3+}$ and $B^{4+}$ ions. The Gibbs energy change for Eq. 2.25 can therefore be written as

Eq. 2.28 $$\Delta_r G^o(Eq.2.25) = \Delta(B^{3+}, B^{2+}) - \delta(LaBO_3).$$

For $LaBO_3$, where B = Ni and Co, the stabilisation energy is large, allowing the "unusual" 3+ valence state of Ni and Co to be maintained in the perovskite. If La was replaced by $Y^{3+}$, the $Y^{3+}$ ion would be too weak to stabilise the 3+ valence state of Ni or Co.

The thermodynamic reactivity of $ABO_3$ reactions with other oxides can be expressed in terms of stabilisation energy. For example, the reactions of $LaBO_3$ (where B = Mn, Co) with YSZ, are given in Eq. 2.29.

Eq. 2.29 $$LaBO_3 + ZrO_2 = \frac{1}{2} La_2Zr_2O_7 + BO + \frac{1}{4} O_2(g).$$

The reaction in Eq. 2.30 can be regarded as a displacement reaction, while Eq. 2.31 is considered as the reduction of $B^{3+}$

Eq. 2.30 $$LaBO_3 + ZrO_2 = \frac{1}{2} La_2Zr_2O_7 + \frac{1}{2} B_2O_3,$$

Eq. 2.31 $$\frac{1}{2} B_2O_3 = BO + \frac{1}{4} O_2(g).$$

The Gibbs energy change $\Delta_r G^o$ for Eq. 2.29 can be written as

Eq. 2.32 $$\Delta_r G^o(Eq.2.29) = \Delta(B^{3+}, B^{2+}) + \frac{1}{2}\delta(La_2Zr_2O_7) - \delta(LaBO_3).$$

At 1273 K, only $LaCoO_3$ reacts with YSZ forming $La_2Zr_2O_7$. Analysis of Gibb's energy changes for the reaction indicates only $LaCoO_3$ reacts, even though both Co and Mn doped $LaBO_3$ have similar stabilisation energies. The difference is explained with respect to the different valence stability's of $Co^{3+}$ and $Mn^{3+}$. Typically $Co^{3+}$ is not stable, but due to a large stabilisation energy associated with the ion in the perovskite phase, it can exist. The $Co^{3+}$ valence state becomes unstable when in chemical contact with zirconia, because the pyrochlore $La_2Zr_2O_7$ and the perovskite $LaBO_3$ have stabilisation energies of similar magnitude (*38, 42*).

When the $B^{3+}$ ion is stable, for example in $LaCrO_3$, reaction with the zirconia is only determined by the difference in the stabilisation energies of $LaCrO_3$ and $La_2Zr_2O_7$. The stabilisation energy of $LaCrO_3$ is larger, thus no $La_2Zr_2O_7$ is formed (*38*).

## 2.2.5 Thermal expansion

Thermal expansion is the change in dimensions of a material with increasing or decreasing temperature. The change is due to the changing amplitude of vibration between atoms with variations in temperature. The size of the dimensional change is related to the bond strength and the arrangement of the atoms in a material. As bond strength increases, the melting point temperature will increase while the thermal expansion coefficient decreases (*43*).

A major consideration when designing the SOFC is to match the thermal expansion of components; otherwise mechanical stresses induced by temperature variations can occur, causing mechanical failure (*44*). A difference in the thermal expansion coefficient (TEC) of cell components when cooling down from fabrication and/or operational temperatures (thermal cycling) can induce stress. Montross et al. (*45*), studying the tensile and shear stresses in planar SOFCs, found the difference in TEC between components should be less than $\Delta\alpha = 0.1 \times 10^{-6}K^{-1}$, for stable SOFC operation. Dopants can be added to modify the TEC of $LaCrO_3$ to obtain a closer match with other components. Table 2.3 shows how dopant addition of 20 mol% Ca to $LaCrO_3$, results in a closer match with 7.5 YSZ. Table 2.3 also illustrates the difference in TEC between various materials associated with the SOFC.

Another important consideration when evaluating perovskites for use in SOFCs is that the thermal expansion of these materials can vary with $Po_2$. According to Montross (*46*), the TEC of alkali earth doped $LaCrO_3$ will change on exposure to wet $H_2$. For example, the TEC of both Sr and Mg doped $LaCrO_3$ will increase under reducing conditions, while for Ca doped $LaCrO_3$, a decrease in TEC is observed.

Mori et al. (*36*) proposed that the interconnect and electrolyte can contact each other in certain designs of SOFC. During operation, $(La,Ca)CrO_3$ and YSZ could react to form $La_2Zr_2O_7$. Because $La_2Zr_2O_7$ has a smaller TEC than YSZ, cracking could occur at the interface due to thermal stresses, causing gas leakage.

Table 2.3. Average linear thermal expansion coefficients.

| Material | TEC (ppm/°C) | Temperature range (°C) | Ref. |
|---|---|---|---|
| $LaCrO_3$ | 9.5 | † | (*47*) |
| $La_{0.9}Ca_{0.1}CrO_3$ | 9.7 | 20-1000 | (*36*) |
| $La_{0.8}Ca_{0.2}CrO_3$ | 10.0 | 20-1000 | (*36*) |
| $La_{0.8}Sr_{0.2}CrO_3$ | 11.1 | 350-1000 | (*3*) |
| $La_{0.6}Sr_{0.4}CoO_3$ | 18.8 | 25-900 | (*48*) |
| $LaCoO_3$ | 22.4 | 100-1100 | (*21*) |
| $Ce_{0.8}Gd_{0.2}O_{2-y}$ | 11.59 | 30-1000 | (*49*) |
| 7.5 YSZ | 10.0 | 20-1000 | (*36*) |
| $La_2Zr_2O_7$ | 9.0 | 20-1000 | (*36*) |
| $SrZrO_3$ | 10.8 | 20-1000 | (*36*) |
| Ni-based alloys | 13-18 | 1000 | (*50*) |
| $Cr5Fe1Y_2O_3$ | 11.3 | † | (*51*) |
| Ag | 25.2 | 900 | (*3*) |

† temperature not given in literature

## 2.2.6 Sintering of perovskite-based materials

Sintering is defined as a process of chemical and physical change accompanied by a reduction in porosity by grain growth and grain bonding. For sintering to occur, a material transport mechanism must be present combined with a source of energy to maintain this material transport. The main mechanisms of material transport are diffusion (lattice and/or grain boundary mechanisms) and viscous flow. The major source of energy is heat, in association with energy gradients due to particle-particle contact and surface tension. Sintering is considered to occur in three stages (simplified here for brevity) (*43, 52*):

- stage 1-involves rearrangement and neck formation between particles;
- stage 2-the neck increases in size, porosity decreases, grains grow and a high amount of shrinkage is observed;
- stage 3-pores shrink to a limited size or disappear and increased grain growth is observed.

Sintering proceeds via a number of mechanisms, these can occur alone or in combination, they are (*43*):

- vapour-phase transport;
- solid-state;
- liquid phase sintering;
- reactive (transient) liquid sintering (similar to liquid phase except the liquid can change composition or disappear).

Vapour phase sintering results in no densification, while solid state and liquid phase sintering can. The driving force for solid state sintering is the reduction in the total free energy $\Delta G_T$ of the system given in Eq. 2.33, where $\Delta G_v$, $\Delta G_b$ and $\Delta G_s$ are the changes in free energy associated with volume, boundaries and surfaces respectively. A reduction of $\Delta G_s$ is considered the major force behind conventional sintering (*52*).

Eq. 2.33 $$\Delta G_T = \Delta G_v + \Delta G_b + \Delta G_s .$$

$LaCrO_3$, $(La,Sr)CrO_3$ and $(La,Ca)CrO_3$ cannot be sintered to high densities in air at moderate temperatures (1300-1400°C). For example, $La_{1-x}Sr_xCrO_3$ (x = 0-0.2) required $Po_2$ activities to exceed $10^{-10}$ atm., with sintering temperatures greater than 1720°C. The following discussion is used to explain the poor sinterability of this material. In high $Po_2$, pure $LaCrO_3$ is poorly sinterable, due to the volatile nature of certain Cr oxide species in oxidising atmospheres. Yokokawa et al. (*30*) proposed the main difficulty in sintering chromite compounds was due to evaporation of gaseous Cr species from $LaCrO_3$, Eq. 2.34,

Eq. 2.34 $$LaCrO_3(s) + \frac{3}{4}O_2(g) \rightarrow CrO_3(g) + \frac{1}{2}La_2O_3(s),$$

and subsequent condensation at the inter-particle neck (bridge between the particles), Eq. 2.35, forming a thin layer of $Cr_2O_3$(s).

Eq. 2.35 $$CrO_3(g) \rightarrow \frac{1}{2}Cr_2O_3(s) + \frac{3}{4}O_2(g).$$

Little densification occurs because the major mass transport mechanism is by evaporation/condensation (vapour phase sintering). This is illustrated in Fig. 2.7.

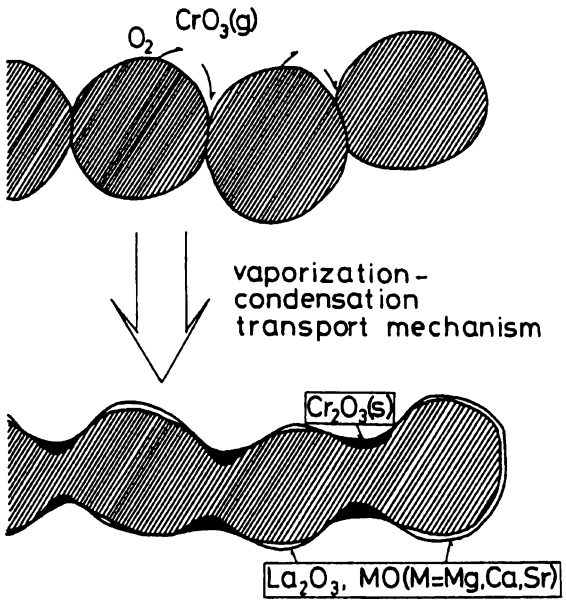


Fig. 2.7. Evaporation/condensation mechanism (vapour phase sintering) of $LaCrO_3$ (*30*).

Heterogenisation occurs inside the pellet because Cr vaporises leaving regions of $La_2O_3$ behind, on the convex surfaces. The formation of a $Cr_2O_3$(s) layer at the neck was considered to stop diffusion, thus reducing sinterability. Improvements in sinterability could be affected by the removal of the $Cr_2O_3$(s) layer, or by a decrease in the $CrO_3$(g) component. Yokokawa et al. (*30*) suggested Ca doped $LaCrO_3$ sintered well because of low $CrO_3$(g) vapour pressures. When x is greater than 0.3, the Cr oxide gases condense as $CaCrO_4$, which has a lower vapour pressure. The model can be used to explain the improved sintering of $LaCrO_3$ by substitution of alkaline earth metals, the use of reducing atmospheres, and the addition of sintering aids. This model assumes the presence of an inter-particle layer of $Cr_2O_3$, for which there is no current evidence.

Methods utilised to overcome the poor sinterability of $LaCrO_3$ include:

- sintering in reducing atmospheres (*53*);
- sintering in a $Cr_2O_3$ environment (*54*);
- liquid phase sintering aids (*25*);
- dopant substitution;
- non-stoichiometry.

The latter two will be discussed in detail.

### 2.2.6.1 Doped Lanthanum Chromite and Cr deficiency

In general, stoichiometric samples such as $La_{0.8}Ca_{0.2}CrO_3$ and $La_{0.8}Sr_{0.2}CrO_3$ are difficult to sinter; Groupp et al. (*53*) attributes the poor sintering of $La_{1-x}Sr_xCrO_3$ to the volatilisation of Cr components. Improved sintering can be achieved by synthesis of Cr deficient (non-stoichiometric) Sr or Ca doped $LaCrO_3$ (*55, 56*). These methods are discussed below. One of the most important effects of dopant addition (*1*) and Cr deficiency on sintering (*56*) is the formation of a transient liquid phase during firing that enhances densification. For example, chromium deficiencies in Ca doped lanthanum chromites have been found to improve the sinterability in air by the formation of $Ca_m(CrO_4)_n$ liquid phases (*56*). Carter et al. (*57*) have shown the formation of the presence of $CaCrO_4$, prior to densification. For Ca doped $LaCrO_3$ the following general conclusions were drawn (*56*):

- Cr deficiency can lead to a large increase in densification (*58*);
- the liquid phase formed $Ca_m(CrO_4)_n$ reacts with $(La,Ca)CrO_3$ increasing mass transport, resulting in rapid densification;
- sintering depends on Ca content in the perovskite, as Ca concentration will affect phase relations between the perovskite and the liquid phase;
- Cr excess can lead to $Cr_2O_3$ formation, this can lead to poor sintering;
- liquid $Ca_m(CrO_4)_n$ phases formed may react with other cell components (*31*).

The proposed liquid phase sintering mechanism of $La_{1-x}Ca_xCrO_3$, is shown in Fig. 2.8 (*56*). Carter et al. (*59*) proposed that the best composition for solid solution stability at SOFC operating temperatures, and for liquid phase sintering, lies between 20 and 30 mol% Ca composition.

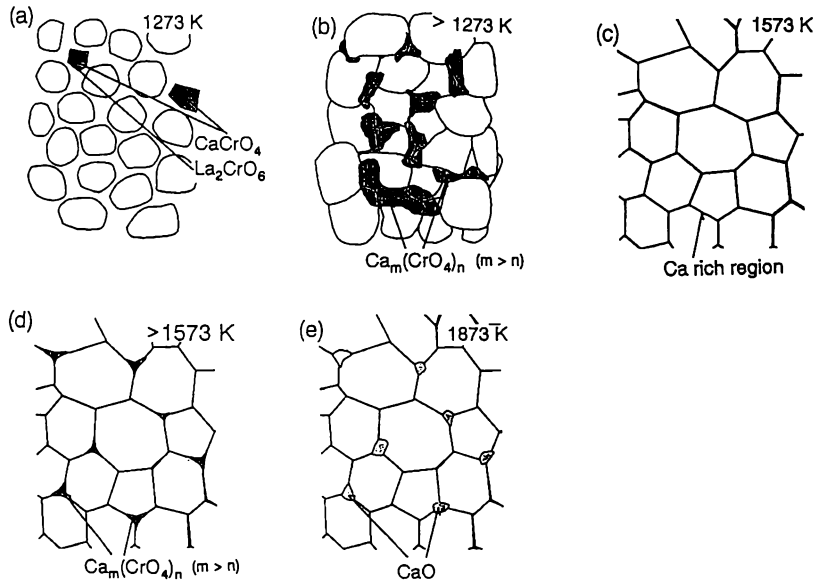


Fig. 2.8. The proposed liquid phase sintering mechanism of $La_{1-x}Ca_xCrO_3$ (*56*).

Sr addition also improves the sinterability and density of $LaCrO_3$. Meadowcroft et al. (*25*) proposed that Sr doping increased density because of the formation of the $SrCrO_4$ phase at intermediate temperatures, followed by melting and liquid phase sintering. Chick et al. (*55*), also found the $SrCrO_4$ phase in the Sr doped perovskite powders at low temperatures of approximately 650°C. After sintering, however, the liquid phase was absent. Chick et al. (*55*) proposed that this absence suggested the sintering mechanism was not due to liquid phase sintering, but predominantly a solid-phase sintering mechanism, involving either bulk or grain boundary diffusion. The authors proposed that the sintering of $(La,Sr)CrO_3$ is dependent upon the relative dominance of vapour-phase as against solid-phase mass transport mechanisms. Chick et al. (*55*) revealed that the highest densities were obtained for Cr deficient $(La,Sr)CrO_3$. Density, however, decreased with Cr enrichment of $(La,Sr)CrO_3$. These observations were consistent with research by Meadowcroft et al. (*60*). Cr enrichment resulted in reduced densities and increased Cr oxide volatility, while Cr

deficient samples sintered to high densities in air, but contained crystals of $La_2O_3$. In addition, stoichiometric samples were homogeneous but yielded poor densities.

#### 2.2.6.2 Sintering of Co doped perovskites

Christiansen et al. (*61*) sintered $(La_{0.7}Ca_{0.3})Cr_{1-y}Co_yO_3$ (y = 0.025) in air at 1300°C, and achieved a density of 98% theoretical. The presence of $CaCrO_4$ and $La_2CrO_6$ were found in Ca and Co doped $LaCrO_3$ powders, indicating a sintering mechanism similar to that of Ca doped $LaCrO_3$. $La_{1-x}Sr_xCoO_{3-\delta}$ (x = 0.2-0.7) was hot pressed at 1100°C under pressure, for 8 h, yielding densities in the range of 95-97% (*62*). Sammes et al. (*63*) sintered $La_{0.9}Sr_{0.1}Cr_{0.9}Co_{0.1}O_3$ in air at 1500°C and achieved a density of 94% theoretical, compared to 84% for $La_{0.9}Sr_{0.1}CrO_3$. A literature survey has revealed little information on the sintering mechanisms of Co doped $(La,Sr)CrO_3$.

## 2.3 Pervoskite coatings on metal alloy interconnects

### 2.3.1 Introduction to the metal alloy interconnect

Metal alloys are attractive materials for use as the interconnect in planar SOFCs because of their high electronic conductivity, high thermal conductivity, ease of machinability and good mechanical integrity (*2*). Of the alloys available, chromia-forming alloys (alloys that form a protective $Cr_2O_3$ scale) are widely used. Chromia-forming alloys are chosen because the oxide scale formed is conductive (*50, 64-66*) and provides a barrier against further oxidation of the metal at high temperatures. Other alloys, such as alumina formers (alloys that form a protective $Al_2O_3$ scale), provide good oxidation resistance at high temperature, but form an insulating scale that reduces the electrical contact between electrode and interconnect (*50, 67*). Typical chromia forming alloys include Cr5Fe1$Y_2O_3$ (*51*), Haynes 230 (*68*), Ni-25Cr, MA 754 (*69*) and Inconel 600 (*70*).

A major disadvantage associated with most of these alloys, is their large mismatch in TEC with other cell components, which can induce cracking in the relatively weak ceramic components during thermal cycling. To overcome the TEC mismatch, Plansee developed Cr5Fe1$Y_2O_3$ a metal alloy interconnect, which has good hot tensile properties, good creep strength, and closely matching TEC (*69*). Unfortunately Cr5Fe1$Y_2O$ is a high cost material.

Further problems associated with alloy interconnects include establishing good electrical contact with the electrodes (*68*) and reduction of volatile chromium species to the cathode (*70-74*). In air at high temperatures (900-1000°C), volatile chromium species react with the (LaSr)$MnO_3$ cathode reducing cell performance. Functional layers applied to the metal interconnect surface, typically perovskite coatings, can improve electrical contact between the cell components (*68, 75*) and can reduce the volatilisation of chromium components to the cathode (*76, 77*).

## 2.3.2 Reactivity of metal alloy interconnects with cell components

A problem associated with the use of the chromia forming interconnects is the degradation of SOFC performance over time (*70, 72-75, 78, 79*). When chromia forming alloys are used on the cathode side of an SOFC, gaseous Cr ($6^+$) species such as $CrO_3$ and $Cr(OH)_2O_2$ are formed that react with the LSM cathode, reducing cell performance. Subsequent deposition through the cathode and at the interconnect/LSM/electrolyte interfaces leads to chemical interaction with the LSM. This results in the formation of a $(CrMn)O_4$ spinel phase which degrades SOFC performance. The mechanisms by which this degradation takes place are complex (*72*). The reaction involves the presence of $Cr_2O_3$ and $(CrMn)O_4$, and also causes changes in chemical composition of the LSM. The changes in chemical composition of the LSM cathode can alter the oxygen adsorption/surface kinetics, resulting in cell degradation. The rate of degradation increased with higher current densities and longer periods of use. When no current was drawn, less degradation was observed (*72*).

Strategies used to overcome Cr evaporation include:

- dense surface coatings;
- coating the gas channels of a planar SOFC with $Al_2O_3$ (chemically more stable compound), and the contacting ribs with doped (La,Sr)$CrO_3$ (*74*);
- inclusion of $La_2O_3$ into the LSM cathode material (reduces Cr vapour pressure due to the reaction of $La_2O_3$ with Cr, forming $LaCrO_3$) (*70*).

### 2.3.3 Perovskite coatings on metal alloy interconnects

Perovskite coatings are applied to the metal interconnect to stop Cr evaporation to the cathode (stopping cell degradation), and to improve electrical contact. The coating needs to adhere to the surface of the metal interconnect providing good electrical contact with the electrodes. Ideally the coating must be:

- high in electrical conductivity;
- impervious to Cr evaporation and solid-state transport (stops Cr species reaching and reacting with the cathode);
- impenetrable to migration of oxygen and oxide ions (oxygen reaching the metal results in increased oxide scale);
- mechanically stable and have matching TEC (*72, 80*).

Various perovskite coatings investigated include (La,Sr)$CoO_3$ (*50*), $LaCoO_3$ (*75*), (La,Sr)$CrO_3$, (LaSr)$MnO_3$ and (La,Ca)$CrO_3$ (*77*). Typically these coatings can be applied to the metal interconnect by vacuum plasma spray (VPS) processes (*75, 77*).

2.3.3.1 Electrical contact between the interconnect/current collect and electrodes

An important consideration when stacking SOFCs is to obtain and maintain good electrical contact between the interconnect and the electrodes, otherwise stack performance can be seriously reduced.

Brückner et al. (*68*) investigated the improvement of the electrical contact between the interconnect and cathode in a planar SOFC. Ignoring bulk resistance of the interconnect, Brückner et al. (*68*) state that sheet and contact resistance contribute to the overall resistance of the SOFC stack. Sheet resistance involves a voltage drop associated with the current flows along the cathode toward the contact area, while contact resistance involves current flows between the interconnect and cathode, Brückner et al. (*68*) investigated the latter.

Brückner et al. (*68*) state that the electrical contact areas between cathode and interconnect are very small, due to rigidity and residual corrugations of their respective surfaces. When, for example, 10 mV is applied between two electronically contacting solids under mechanical pressure, electron flow can only occur when the separation is 0.1 nm or less. Application of a 50 μm thick perovskite coating onto the interconnect can increase the contact area. Heating the stack under mechanical pressure results in the coating adjusting to variations in mechanical pressure compensating for surface roughness. Thus, contact area is increased with a corresponding decrease in resistance.

A clear example showing the positive effect coatings can have on SOFC stack performance is shown by Brückner et al. (*68*). For SOFC stacks at 0.7 V, 0.4 A $cm^{-2}$ was achieved using coatings, while only 10 mA $cm^{-2}$ was realised for the non-coated interconnect SOFC stack. For an uncoated Cr forming alloy, contact resistances of between 300 to 400 mΩ $cm^2$ were realised, while coatings reduced the contact resistance to levels as low as 30 mΩ $cm^2$. Other authors (*50, 81*) have also demonstrated improvement in electrical contact and cell performance by employing perovskite coatings. For example, the I-V characteristics of a planar cell using

uncoated and $La_{0.6}Sr_{0.4}CoO_3$ coated metal wire current collectors (Fig. 2.9), shows the coating can improve cell performance (*81*).

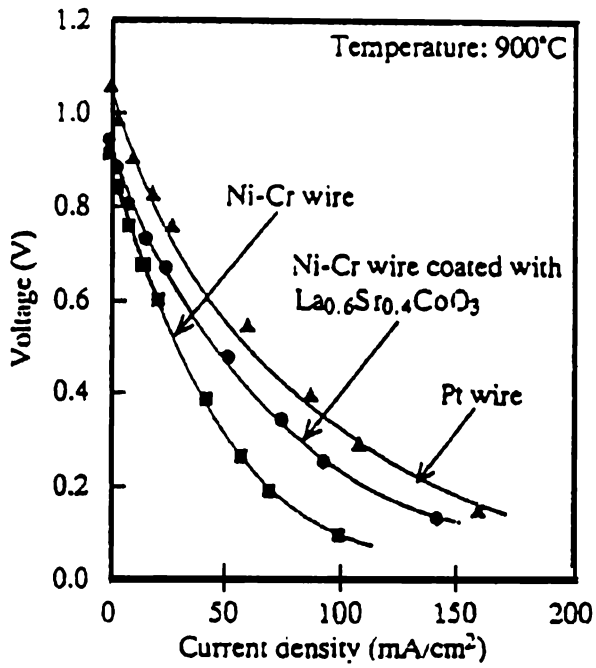


Fig. 2.9. I-V characteristics of a planar cell using uncoated and $La_{0.6}Sr_{0.4}CoO_3$ coated metal wire current collectors (*81*).

The electrical contact area and geometry of the interconnect/current collect is also an important consideration, as it can have a major effect on SOFC performance. Sasaki et al. (*82*), studying a planar SOFC, found that both ohmic loss and cathode polarisation increased with increased current collect contact spacing. The effective electrode area was shown to decrease with increased contact spacing. Additionally, Koeppen et al. (*83*) calculated the maximum number of contacts required to obtain highest power outputs for planar SOFCs. If too much of the active electrode area was covered, it could result in decreased stack performance. Furthermore, the geometry of the contacting areas of the interconnect is important in obtaining maximum power output. Small circular cylinders, jutting out from the interconnect plate, were shown to provide improved electrical contact over the normal ribbed design contacts.

### 2.3.3.2 Layered coatings on metal alloy interconnects

Additional perovskite layers can be applied over existing coatings. The coatings perform different functions. Brückner et al. (*75*) used a layered coating, where $La_{0.9}Sr_{0.1}CrO_3$ was applied using vacuum plasma spraying onto the interconnect, this layer was highly dense and contacted the metal interconnect. A second porous layer of $LaCoO_3$ was applied (using an air brush) over the $La_{0.9}Sr_{0.1}CrO_3$. The function of $La_{0.9}Sr_{0.1}CrO_3$ was to protect the cathode from Cr evaporation, while the function of the second layer was to provide electrical contact during thermal cycling. The $LaCoO_3$ was porous, and able to deform, providing good electrical contact between the interconnect and the cathode during thermal cycling, such that contact resistance remained low and constant. If $LaCoO_3$ was used without the protective coating, contact resistance increased constantly during operation. For example, after thermal cycling, the contact resistance had been found to increase by a factor of 2 which was attributed to a large mismatch in TEC between $LaCoO_3$ and the interconnect, causing the coating to de-laminate from the surface of the interconnect. Other multi-layer combinations were used by Brückner et al. (*75*) who achieved similar results.

## 2.4 Interconnect design

There are many planar (*51, 81, 84-89*) and tubular interconnect designs (*90-93*). The material requirements of the interconnect are dependent on the design of the SOFC and associated interconnect. It is possible to widen or reduce the materials' selection by changing the interconnect design.

Changes to the design of the interconnect often incur a new set of challenges. For example, a major focus of interconnect design is to maintain good electrical contact between electrodes and interconnect during thermal cycling without the build up of stresses. If a simple fixed planar SOFC is used, where the TEC of the interconnect and other cell components are closely matching, the effect of thermal cycling will be less severe (as movement and thermal stresses will be minimal), but the materials selection will be seriously restricted. Alternatively, if a free floating planar design is

adopted, the materials selection is widened considerably, as mismatches in TEC are compensated for by free movement of the interconnect, however the physical design increases in complexity. Design areas such as sealing and breakdown of interconnect/electrode contact become increasingly complex to solve. This increase in complexity is seen from the fixed, shown in Fig. 2.10(a), to the free floating planar interconnect designs shown in Fig. 2.10(b) (*85*). The interconnect in the fixed planar design is limited to Cr5Fe1$Y_2O_3$ or (La,Sr)$CrO_3$ materials that have a matching TEC with the cell components. The other planar designs can accommodate metal interconnects such as Inconel 600 and Hastalloy X, which have higher TEC values.

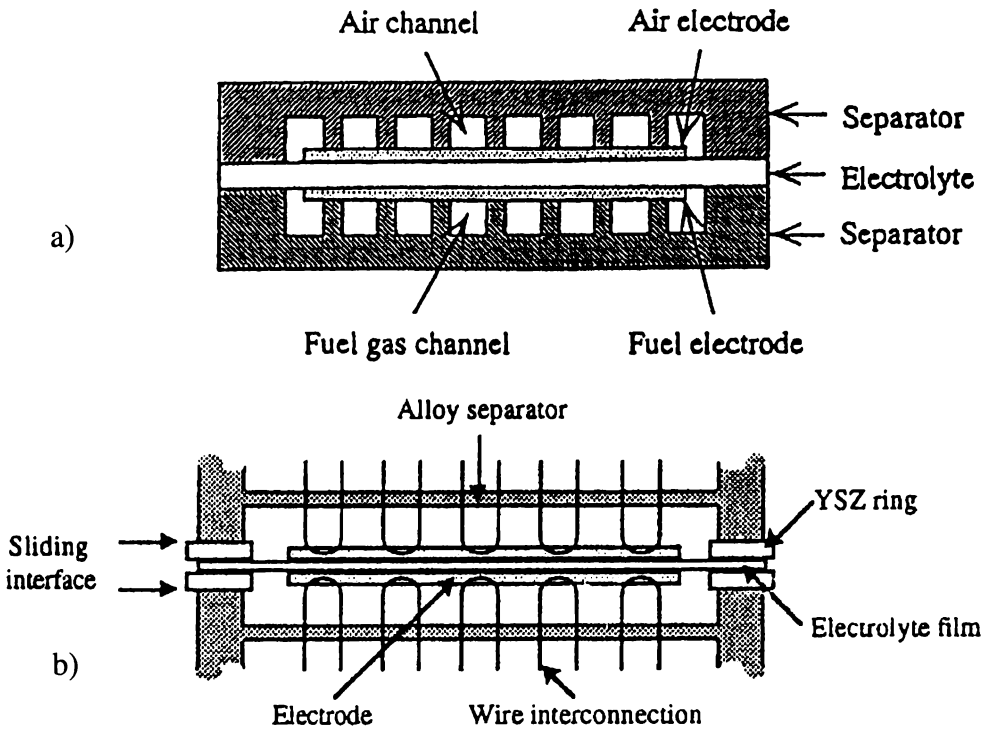


Fig. 2.10. Electrical interconnection in the fixed (a), and free floating (b) planar interconnect designs (*85*).

The tubular interconnect designs are shown in Fig. 2.11 for the Siemens Westinghouse design (*94*) and in Fig. 1.6 for the small diameter tubular design.

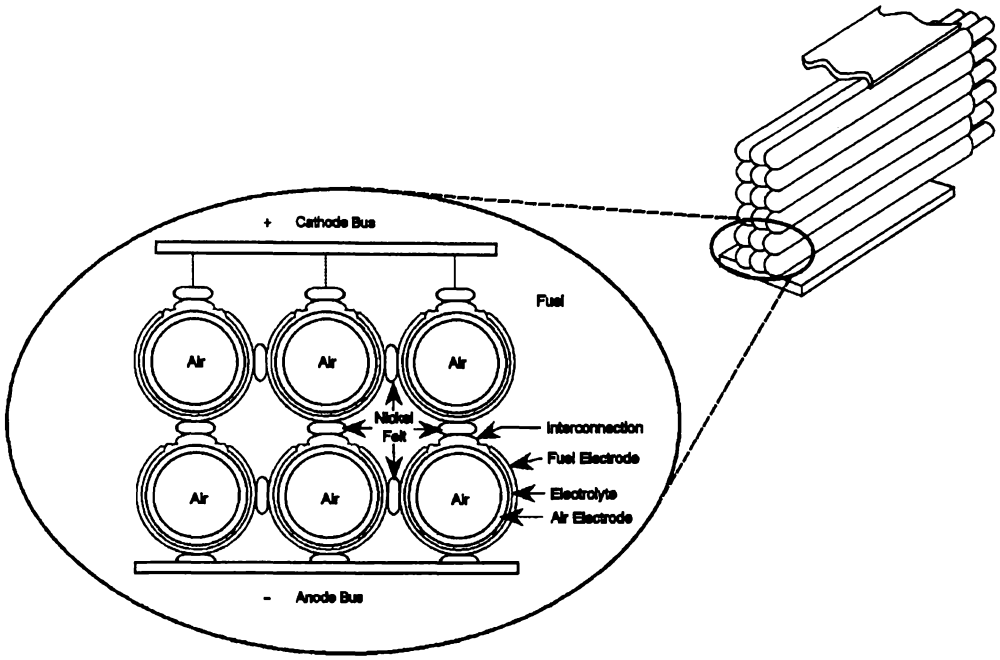


Fig. 2.11. Electrical interconnection in the Siemens Westinghouse tubular design (*94*).

## 2.5 References


1. N. Q. Minh, *J. Amer. Ceram. Soc.* **76**, 563 (1993).
2. M. Dokiya, T. Horita, N. Saki, T. Kawada, H. Yokokawa, B. A. van Hassel, and C. S. Montross, *in* "14th Risø International Symposium on Material Science" (F. W. Poulsen, J. J. Bentzen, T. Jacobsen, E. Skou, and M. J. L. Østergård, eds.), p. 33, 1993.
3. P. Kofstad and R. Bredesen, *Solid State Ionics* **52**, 69 (1992).
4. S. Desouza, S. J. Visco, and L. C. Dejonghe, *J. Electrochem. Soc.* **144**, L35 (1997).
5. D. L. Maricle, T. E. Swarr, and S. Karavolis, *Solid State Ionics* **52**, 173 (1992).
6. K. Zheng, B. C. H. Steele, M. Sahibzada, and I. S. Metcalfe, *Solid State Ionics* **86-8**, 1241 (1996).
7. H. U. Anderson, *in* "14th Risø International Symposium on Material Science, High Temperature Electrochemical Behaviour of Fast Ion and Mixed Conductors" (F. W. Poulsen, J. J. Bentzen, T. Jacobsen, E. Skou, and M. J. L. Østergård, eds.), p. 1, 1993.
8. F. S. Galasso, "Perovskites and High Tc Superconductors," p. 293. Gordon and Breach Science Publishers, 1990.
9. N. Ramadass, *Mat. Sci. Eng.* **36**, 231 (1978).
10. C. P. Khattak and D. E. Cox, *Mat. Res. Bull.* **12**, 463 (1997).
11. N. Sakai, T. Kawada, H. Yokokawa, and M. Dokiya, *Solid State Ionics* **40/41**, 394 (1991).
12. A. N. Petrov, O. F. Kononchuk, A. V. Andreev, V. A. Cherepanov, and P. Kofstad, *Solid State Ionics* **80**, 189 (1995).
13. J. Mizusaki, *Solid State Ionics* **52**, 79 (1992).
14. H. U. Anderson, *Solid State Ionics* **52**, 33 (1992).
15. F. A. Kröger and H. J. Vink, *Solid State Physics* **3**, 307 (1965).
16. I. Yasuda and T. Hikita, *J. Electrochem. Soc.* **140**, 1699 (1993).
17. I. Yasuda and M. Hishinuma, *Solid State Ionics* **80**, 141 (1995).

18. J. A. M. van Roosmalen and E. H. P. Cordfunke, *J. Solid State Chem.* **93**, 212 (1991).

19. H. E. Höfer and R. Schmidberger, *J. Electrochem. Soc.* **141**, 782 (1994).

20. M. Mori, T. Yamamoto, H. Itoh, T. Abe, S. Yamamoto, Y. Takeda, and O. Yamamoto, *in* "First European Solid Oxide Fuel Cell Forum" (U. Bossel, ed.), Vol. 1, p. 465, Lucerne Switzerland, 1994.

21. H. Schmidt, B. Brückner, and K. Fischer, *in* "Proceedings of the Fourth International Symposium on Solid Oxide Fuel Cells (SOFC-IV)" (M. Dokiya, O. Yamamoto, H. Tagawa, and S. C. Singhal, eds.), p. 869. The Electrochemical Society Inc., Yokohama, Japan, 1995.

22. D. P. Karim and A. T. Aldred, *Physical Review B* **20**, 2255 (1979).

23. P. A. Cox, "The Electronic Structure and Chemistry of Solids," p. 1. Oxford University Press, 1987.

24. J. A. M. van Roosmalen, J. P. P. Huijsmans, and L. Plomp, *Solid State Ionics* **66**, 279 (1993).

25. D. B. Meadowcroft, *Brit. J. Appl. Phys. Revs.* , 1225 (1969).

26. R. Koc and H. U. Anderson, *J. Mat. Sci.* **27**, 5477 (1992).

27. A. N. Petrov and P. Kofstad, *in* "Proceedings of the Third International Symposium on Solid Oxide Fuel Cells" (S. C. Singhal and H. Iwahara, eds.), Vol. 93 - 94, p. 220, Honolulu, Hawaii, 1993.

28. P. M. Raccah and J. B. Goodenough, *Journal of Applied Physics* **39**, 1209 (1968).

29. N. Sakai, T. Kawada, H. Yokokawa, and M. Dokiya, *in* "The Second International Symposium on Solid Oxide Fuel Cells" (F. Grosz, P. Zegers, S. C. Singhal, and O. Yamamoto, eds.), p. 629, Athens, Greece, 1991.

30. H. Yokokawa, N. Sakai, T. Kawada, and M. Dokiya, *J. Electrochem. Soc.* **138**, 1018 (1991).

31. J. D. Carter, C. C. Appel, and M. Mogensen, *J. Solid State Chem.* **122**, 407 (1996).

32. I. Yasuda and M. Hishinuma, *Solid State Ionics* **78**, 109 (1995).

33. I. Yasuda and T. Hikita, *J. Mat. Sci.* **29**, 2801 (1994).

34. N. Sakai, T. Kawada, H. Yokokawa, and M. Dokiya, *in* "IFCC The International Fuel Cell Conference", p. 365, Makuhari, Japan, 1992.

35. T. Kawada, N. Sakai, H. Yokokawa, M. Dokiya, and I. Anzai, *Solid State Ionics* **50**, 189 (1992).

36. M. Mori, H. Itoh, N. Mori, T. Abe, O. Yamamoto, Y. Takeda, and N. Imanishi, "Science and Technology of Zirconia V," p. 776. Technomic Publishing Co. Inc., NY., 1993.

37. N. Sakai, T. Kawada, H. Yokokawa, M. Dokiya, and T. Iwata, *J. Mat. Sci.* **25**, 4531 (1990).

38. H. Yokokawa, N. Sakai, T. Kawada, and M. Dokiya, *Solid State Ionics* **52**, 43 (1992).

39. M. Mori, "PhD Thesis - Study of Materials for High Temperature Solid Oxide Fuel Cells," Mie University, Tsu, Japan, 1995.

40. T. Yamamoto, H. Itoh, M. Mori, N. Mori, T. Watanabe, N. Imanishi, Y. Takeda, and O. Yamamoto, *J. Power Sources* **61**, 219 (1996).

41. N. Sakai, T. Kawada, H. Yokokawa, and M. Dokiya, *in* "Proc. of Zirconia V", p. 1, Melbourne, 1992.

42. H. Yokokawa, S. Yamauchi, and T. Matsumoto, *Thermochim Acta* **245**, 45 (1994).

43. D. W. Richardson, "Modern Ceramic Engineering - Properties, Processing, and Use in Design,". Marcel Dekker, Inc., 1992.

44. S. Majumdar, T. Claar, and B. Flandermeyer, *J. Am. Ceram. Soc.* **69**, 628 (1986).

45. C. S. Montross, H. Yokokawa, and M. Dokiya, *in* "Proceedings of the Second Symposium on Solid Oxide Fuel Cells", p. 121, Solid Oxide Fuel Cell Society of Japan - Extended Abstracts, Tokyo, 1993.

46. C. S. Montross, *Brit. Ceram. Trans.* **95**, 1 (1996).

47. N. Q. Minh and T. Takahshi, "Science and Technology of Ceramic Fuel Cells," p. 183. Elsevier Science B.V., Netherlands, 1995.

48. K. Eguchi, T. Setoguchi, and H. Hiromichi, *in* "Energy Conversion and Utilisation with High Efficiency - Science and Technology for Energy Conversion", p. 93. 1990.

49. G. A. Tompsett and N. M. Sammes, *J. Am. Ceram. Soc.* **80**, 3181 (1997).

50. T. Kadowaki, T. Shiomitsu, E. Matsuda, H. Nakagawa, H. Tsuneizumi, and T. Maruyama, *Solid State Ionics* **67**, 65 (1993).

51. W. Köck, H. P. Martinz, H. Greiner, and M. Janousek, *in* "Proceedings of the Fourth International Symposium on Solid Oxide Fuel Cells (SOFC-IV)" (M. Dokiya, O. Yamamoto, H. Tagawa, and S. C. Singhal, eds.), p. 841. The Electrochemical Society Inc., Yokohama, Japan, 1995.

52. J. S. Reed, "Introduction to the Principals of Ceramic Processing," p. 486. John Wiley & Sons, Inc., New York, 1988.

53. L. Groupp and H. U. Anderson, *J. Am. Ceram. Soc.* **59**, 449 (1976).

54. L. W. Tai and P. A. Lessing, *J Amer Ceram Soc* **74**, 155 (1991).

55. L. A. Chick, J. L. Bates, and G. D. Maupin, *in* "The Second International Symposium on Solid Oxide Fuel Cells" (F. Grosz, P. Zegers, S. C. Singhal, and O. Yamamoto, eds.), p. 621, Athens, Greece, 1991.

56. N. Sakai, T. Kawada, H. Yokokawa, M. Dokiya, and I. Kojima, *J. Amer. Ceram. Soc.* **76**, 609 (1993).

57. J. D. Carter, V. Sprenkle, M. M. Nasrallah, and H. U. Anderson, *in* "Proceedings of the Third International Symposium on Solid Oxide Fuel Cells" (S. C. Singhal and H. Iwahara, eds.), Vol. 93 - 94, p. 344, Honolulu, Hawaii, 1993.

58. N. Sakai, T. Kawada, H. Yokokawa, M. Dokiya, and T. Iwata, *Solid State Ionics* **40/41**, 394 (1990).

59. J. D. Carter, "PhD Thesis - The Low-Temperature Sintering Behaviour of ((La,Ca)$CrO_3$),". University of Missouri-Rolla, 1992.

60. D. B. Meadowcroft and J. M. Wimmer, *Amer. Ceram. Soc. Bull.* **58**, 610 (1979).

61. N. Christiansen, P. Gordes, N. C. Alstrup, and G. Mogensen, *in* "Proceedings of the Third International Symposium on Solid Oxide Fuel Cells" (S. C. Singhal and H. Iwahara, eds.), Vol. 93 - 94, p. 401, Honolulu, Hawaii, 1993.

62. J. Mizusaki, J. Tabuchi, T. Matsuura, S. Yamauchi, and K. Fueki, *J. Electrochem. Soc.* **136**, 2082 (1989).

63. Sammes and R. Ratnaraj, *J. Mat. Sci.* **32**, 1839 (1996).

64. A. Holt and P. Kofstad, *Solid State Ionics* **69**, 137 (1994).

65. A. Holt and P. Kofstad, *Solid State Ionics* **69**, 127 (1994).

66. P. Kofstad, *in* "Second European Solid Oxide Fuel Cell Forum" (B. Thorstensen, ed.), Vol. 1, p. 479, Oslo Norway, 1996.

67. W. J. Quadakkers, H. Greiner, M. Hansel, A. Pattanaik, A. S. Khanna, and W. Mallener, *Solid State Ionics* **91**, 55 (1996).

68. B. Brückner, H. Landes, and B. Rathjen, *in* "Proceedings of the Third International Symposium on Solid Oxide Fuel Cells" (S. C. Singhal and H. Iwahara, eds.), Vol. 93 - 94, p. 641, Honolulu, Hawaii, 1993.

69. W. Quadakkers, H. Greiner, and W. Köck, *in* "First European Solid Oxide Fuel Cell Forum" (U. Bossel, ed.), Vol. 1, p. 525, Lucerne Switzerland, 1994.

70. S. Taniguchi, M. Kadowaki, T. Yasuo, Y. Akiyama, Y. Itoh, Y. Miyake, and K. Nishio, *Denki Kagaku* **64**, 568 (1996).

71. Y. Akiyama, S. Taniguchi, T. Yasuo, M. Kadowaki, and T. Saitoh, *J. Power Sources* **50**, 361 (1994).

72. S. P. S. Badwal, R. Deller, K. Foger, Y. Ramprakash, and J. P. Zhang, *Solid State Ionics* **99**, 297 (1997).

73. S. Taniguchi, M. Kadowaki, H. Kawamura, T. Yasuo, Y. Akiyama, Y. Miyake, and T. Saitoh, *J. Power Sources* **55**, 73 (1995).

74. W. J. Quadakkers, H. Greiner, W. Köck, H. P. Buchkremer, K. Hilpert, and D. Stöver, *in* "Second European Solid Oxide Fuel Cell Forum" (B. Thorstensen, ed.), Vol. 1, p. 297, Oslo Norway, 1996.

75. B. Brückner, C. Günther, R. Ruckdäschel, E. Fendler, and H. Schmidt, *in* "Fuel Cell", p. 155, Orlando Florida, November 17-20, 1996.

76. J. Urbanek, M. Miller, H. Schmidt, and K. Hilpert, *in* "Second European Solid Oxide Fuel Cell Forum" (B. Thorstensen, ed.), Vol. 1, p. 503, Oslo Norway, 1996.

77. E. Fendler, R. Henne, R. Ruckaschel, and H. Schmidt, *in* "Second European Solid Oxide Fuel Cell Forum" (B. Thorstensen, ed.), Vol. 1, p. 269, Oslo Norway, 1996.

78. S. Taniguchi, M. Kadowaki, H. Kawamura, T. Yasuo, Y. Akiyama, Y. Miyake, T. Saitoh, and M. Harada, *in* "1994 Fuel Cell Seminar", p. 41, San Diego, California, 1994.

79. C. Günther, H. J. Beie, P. Greil, and F. Richter, *in* "Second European Solid Oxide Fuel Cell Forum" (B. Thorstensen, ed.), Vol. 1, p. 491, Oslo Norway, 1996.

80. E. Batawi, K. Honegger, R. Diethelm, and M. Wettstein, *in* "Second European Solid Oxide Fuel Cell Forum" (B. Thorstensen, ed.), Vol. 1, p. 307, Oslo Norway, 1996.

81. T. Kimura, T. Namikawa, and Y. Yamazaki, *Denki Kagaku* **61**, 1115 (1993).

82. K. Sasaki and L. J. Gauckler, *Denki Kagaku* **64**, 654 (1996).

83. J. Koeppen and W. Winkler, *in* "Second European Solid Oxide Fuel Cell Forum" (B. Thorstensen, ed.), Vol. 1, p. 247, Oslo Norway, 1996.

84. N. Tomita, T. Namikawa, and Y. Yamazaki, *Denki Kagaku* **62**, 638 (1994).

85. Y. Yamazaki, T. Namikawa, N. Oishi, and T. Yamazaki, *in* "Proceedings of the Fourth International Symposium on Solid Oxide Fuel Cells (SOFC-IV)" (M. Dokiya, O. Yamamoto, H. Tagawa, and S. C. Singhal, eds.), p. 236. The Electrochemical Society Inc., Yokohama, Japan, 1995.

86. Y. Yamazaki, T. Namikawa, T. Ide, H. Kabumoto, N. Oishi, T. Motoki, and T. Yamazaki, *in* "Solid Oxide Fuel Cells V" (U. Stimming, S. C. Singhal, H. Tagawa, and W. Lehner, eds.), Vol. PV 97-40, p. 1291. The Electrochemical Society, Inc., Aachen, Germany, 1997.

87. K. Akagi, A. Siartori, M. Iha, and O. Chikagawa, *in* "Proceedings of the Fourth International Symposium on Solid Oxide Fuel Cells (SOFC-IV)" (M. Dokiya, O. Yamamoto, H. Tagawa, and S. C. Singhal, eds.), p. 129. The Electrochemical Society Inc., Yokohama, Japan, 1995.

88. L. Blum, W. Drenkahan, H. Greiner, and E. Ivers-Tiffee, *in* "Proceedings of the Fourth International Symposium on Solid Oxide Fuel Cells (SOFC-IV)" (M. Dokiya, O. Yamamoto, H. Tagawa, and S. C. Singhal, eds.), p. 163. The Electrochemical Society Inc., Yokohama, Japan, 1995.

89. U. Bossel, *in* "Proceedings of the Fourth International Symposium on Solid Oxide Fuel Cells (SOFC-IV)" (M. Dokiya, O. Yamamoto, H. Tagawa, and S. C. Singhal, eds.), p. 42. The Electrochemical Society Inc., Yokohama, Japan, 1995.

90. K. Kendall and T. W. J. Longstaff, *in* "Second European Solid Oxide Fuel Cell Forum" (B. Thorstensen, ed.), Vol. 1, p. 195, Oslo Norway, 1996.

91. H. Sasaki, S. Otoshi, M. Suzuki, T. Sogi, A. Kajimura, N. Sugiura, and M. Ippommatsu, *Solid State Ionics* **72**, 253 (1994).

92. A. O. Isenberg, *Solid State Ionics* **3/4**, 431 (1981).

93. N. Hisatome, K. Nagata, S. Kakigami, and H. Omura, *in* "Fuel Cell", p. 195, Orlando Florida, November 17-20, 1996.

94. "Fuel Cell Handbook," US Department of Energy, Pittsburgh, Penn., USA, 1998.

# Chapter Three

## *Experimental Methods*

# 3.1 Introduction

Each Chapter given in this thesis contains the relevant experimental methods Section. For clarity, however, this Chapter contains further information on certain experimental apparatus and methods.

## 3.1.1 Apparatus used to measure the electrical properties of tubular SOFCs

Fig. 3.1 shows an overview of the experimental apparatus used to measure the electrical properties of the tubular SOFCs. The cells were placed in a purpose-built furnace (non-inductively wound). A gas line connected to a dual supply of $H_2$ and $N_2$ was then attached to the end of the cell, while the current collecting, and associated reference and sensing wires for the electrodes, were brought outside the furnace. Before testing, the cells were heated in the furnace to the desired temperature, while $N_2$ was passed through the tube. Upon reaching operational temperature the $N_2$ supply was slowly turned off as $H_2$ was added. The anode was then reduced by passing pure $H_2$, at a rate of 25 $cm^3$ $min^{-1}$, bubbled through water at 25°C, through the cell for 15 min. The current-voltage characteristics (I-V) of the cells were then measured using a potentiostat in air at a constant operating temperature, and constant flow rate of 25 $cm^3$ $min^{-1}$ $H_2$. The cathode resistance was determined by the potential difference between the sensing electrode on the cathode and a reference electrode adjacent to the cathode (see position V1 in Fig. 3.2). The contact resistance was ascertained by measuring the potential difference between the cathode current collect and a small sensing electrode adjacent to the current-collector on the same cathode (see position V2 in Fig. 3.2).

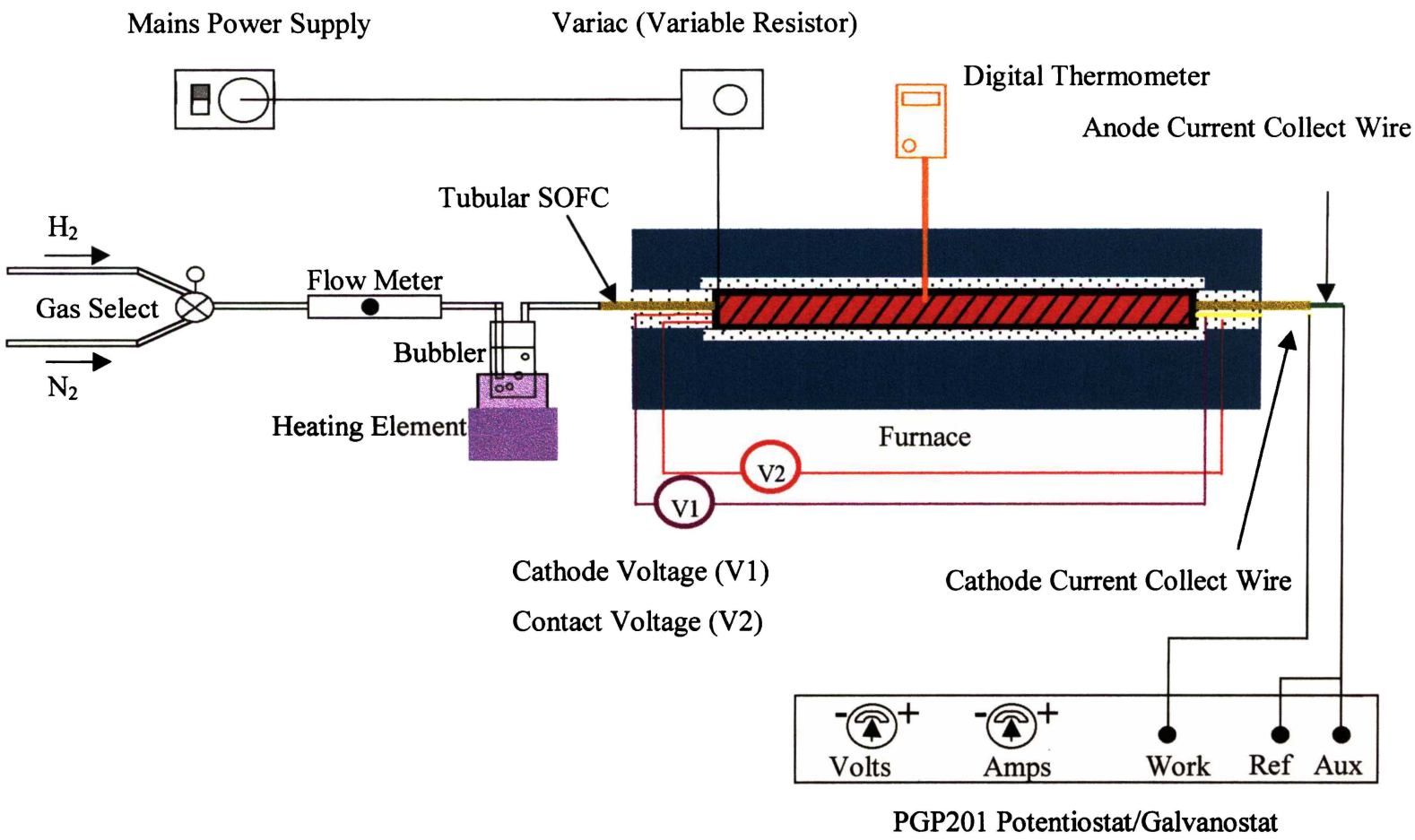


Fig 3.1. Schematic showing an overview of the experimental apparatus used to measure the I-V characteristics of tubular SOFCs.

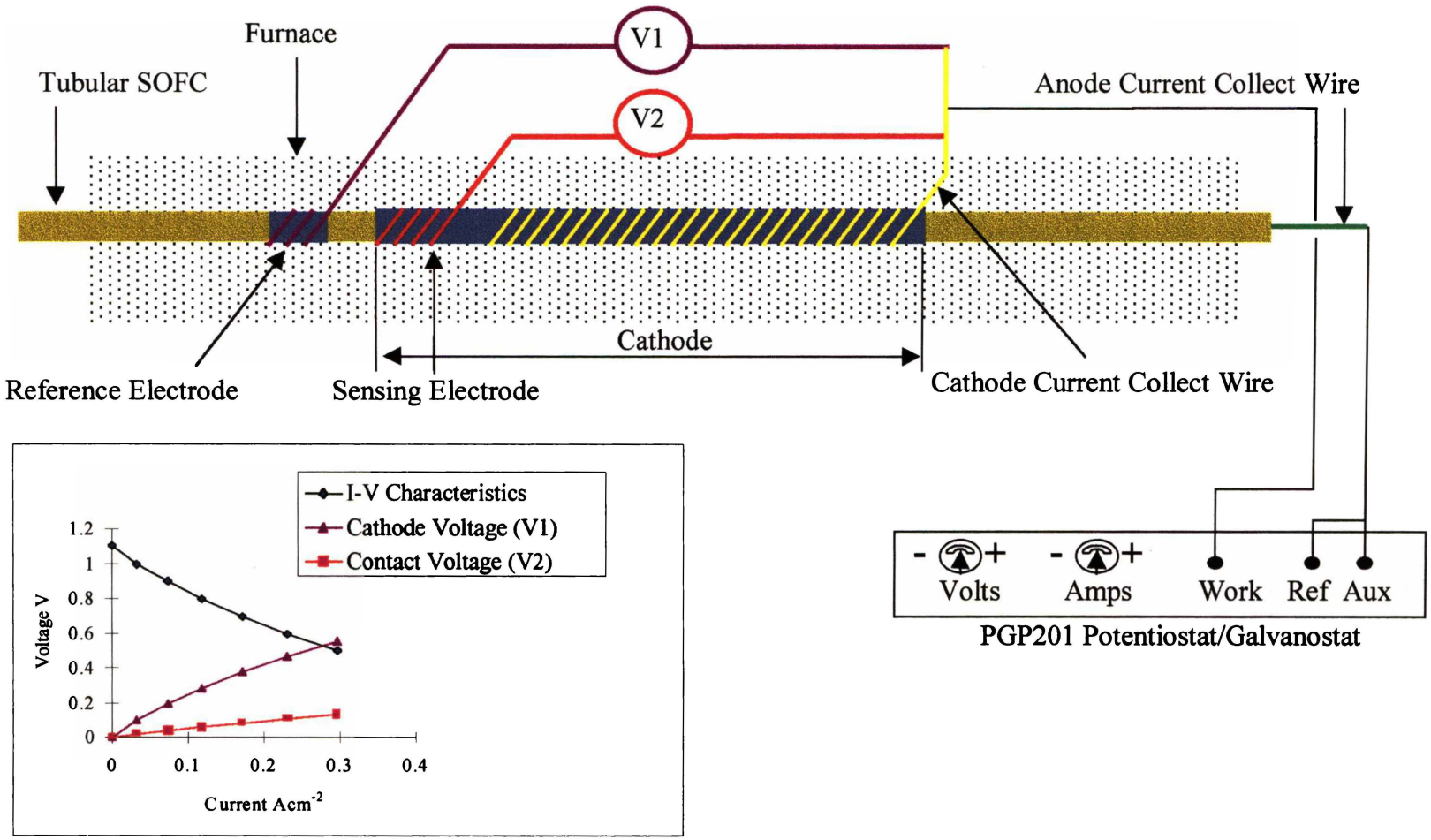


Fig 3.2. Detailed view showing the electrode configuration used to measure the electrical properties of tubular SOFCs. The graph shows the typical I-V characteristics, cathode voltages and contact voltages obtained.

### 3.1.2 Apparatus used to extrude tubular SOFCs

Fig. 3.3 shows the in-house designed high-strength steel piston extruder used to extrude tubular SOFCs. To reduce friction between the die wall and extrudate, surfaces in contact with the extrudate (the die head and the spider) were polished using 1 μm diamond paste. The diameter of the exit hole was 3.38 mm and the diameter of the pin was 3.15 mm. A PTFE 2 cm long plug, approximately 0.3 mm larger than piston bore (such that a push fit seal was obtained), was placed between the metal piston and the extrudate, and was used as a seal to stop the extrudate from jamming the piston. After the extrudate was located in the piston hole with the PTFE seal and piston on top, the die was placed on a stand on an Instron 25 kN testing machine. The piston was forced down at a constant rate of 2.5 mm $min^{-1}$. The extrudate was then forced through the die to form the tubes. After the extruded tubes had been dried, the tubes were placed in an oven and the binder burnt out, using a heating rate of 0.5°C $min^{-1}$ up to 650°C. The tubes were then heated at a higher rate of 5°C $min^{-1}$ to the appropriate sintering temperature.

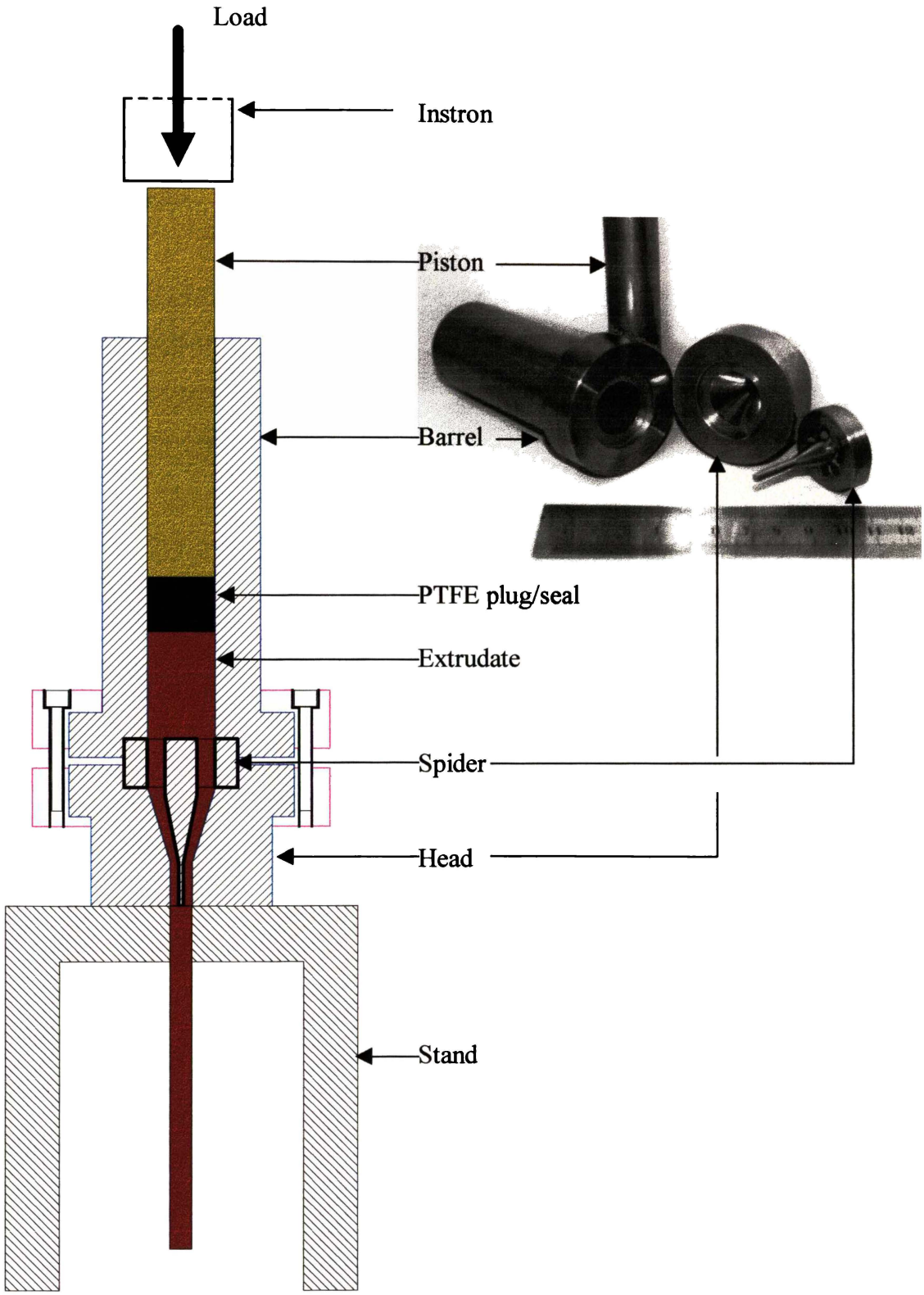


Fig. 3.3. Cross-sectional drawing and photograph of extruder described in Chapter 5.

### 3.1.3 Fabrication of the grooved $Cr5Fe1Y_2O_3$ interconnect/current collect plate

The grooved $Cr5Fe1Y_2O_3$ plate, obtained from Plansee (a-6600 Rutte Tirol Austria), was machined using a Monoset cutter and tool grinder (Cincinnati Milling Machine Co.) with a parting off wheel. An example of a grooved plate is shown in Fig. 3.4.

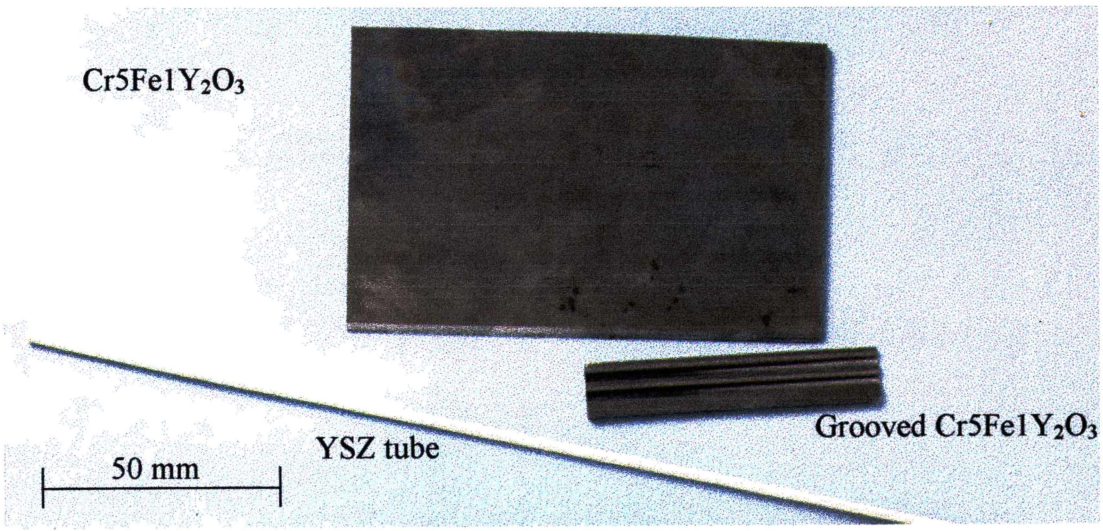


Fig. 3.4. Shows an example of the grooved $Cr5Fe1Y_2O_3$ interconnect, the $Cr5Fe1Y_2O_3$ plate from which it was machined, and a YSZ electrolyte tube.

# Chapter Four

## *Cathode Current-Collectors for a Novel Tubular Solid Oxide Fuel Cell Design*

Published in: *J. Power Sources* **70**, 85 (1998)

# *Introductory note*

Silver wires or metal alloy Nimonic 90 wires wound around (LaSr)$MnO_3$ (LSM) cathodes were initially used by Kilbride (*1*) as cathode current collector/interconnector for small diameter YSZ based high temperature (900°C) tubular SOFCs. The purpose of the work studied in this Chapter was to further develop these methods of current-collection/interconnection by improving electrical contact between the current collector and the cathode, and thus achieve better cell performances.

Silver coatings, applied as strips along the LSM cathodes, were investigated in this Chapter as an alternative to the silver wires developed by Kilbride (*1*). It was considered that this development would lead to better electrical contact (the silver coating would remain in intimate electrical contact with the cathode), and be less cumbersome (no wires wound around the cathode). When tests were performed using both methods of current collection, the silver strip coating yielded similar cell performances as those achieved for the silver wire. Unfortunately at high temperatures the evaporation of silver is high, thus making it unsuitable for sustained use in high temperature SOFCs.

Alternative methods of current collection were therefore examined. Typically, metals that form a moderately conductive protective $Cr_2O_3$ scale (chromia formers) are employed as the current collect/interconnect in high temperature SOFCs (*2*). To improve the electrical contact between the metal wire current collector and cathode, metal alloy wires were coated with $LaCoO_3$. This coating was shown by Schmidt et al. (*3*) to improve the electrical contact between the metal interconnect and the cathode in a planar design SOFC. $LaCoO_3$ was also chosen because Schmidt et al. (*3*) revealed its superior performance in maintaining low contact resistance over $La_{0.8}Sr_{0.2}MnO_3$ and $La_{0.8}Sr_{0.2}CoO_3$ coatings. The use of perovskite coatings on metal current collects/interconnects to improve cell performance is discussed in Chapter Two.

The metal alloy wire cathode current collectors yielded lower cell performances than the silver systems. The use, however, of conductive $LaCoO_3$ coatings on the metal alloy wires did demonstrate that coatings can improve cell performance through better electrical contact.

The silver systems yielded better cell performances than the metal wires. If silver could be incorporated into the interconnect design of a medium temperature SOFC, silver evaporation could be reduced considerably, and high cell performance maintained for longer durations. As described by Kofstad et al. (*4*), alternative materials such as silver-ceramic composite (cermet) may be incorporated into the current collect/interconnect design, if a reduction in SOFC operational temperature is achieved.

This led to the fabrication of medium temperature $Gd_2O_3$ doped $CeO_2$ electrolyte tubes. The purpose of the research detailed in Chapter Five was to fabricate a lower operational (550–650°C) temperature electrolyte ($Ce_{0.8}Gd_{0.2}O_{1.9}$) tubular SOFC. If lower temperature operation was achieved, a wider variety of current collect/interconnect materials could be used.

Published in: *J. Power Sources* **70**, 85 (1998).

# Cathode Current-Collectors for a Novel Tubular SOFC Design

C. E. Hatchwell and N. M. Sammes
Centre for Technology, The University of Waikato, Private Bag 3105, Hamilton New Zealand

K. Kendall
The Birchall Centre for Materials Science, Keele University, Staffordshire ST55BG, Great Britain

## 4.1 Abstract

Two methods of current collection/interconnection are developed for a novel tubular design solid oxide fuel cell (SOFC). Nimonic 90 wires, coated with $LaCoO_{3-\delta}$ are used as cathode current-collectors. When compared with the uncoated Nimonic wires, the $LaCoO_{3-\delta}$ perovskite coated Nimonic wires improve the current densities of the cells. The latter is attributed to the fact that the coating improves the electrical contact between the wire and the cathode. The second method of current collection, whereby silver inks are painted on to the surface of the cathodes and then fired in situ, achieves greater cell performances than the Nimonic 90 wire systems. At 900°C and 0.7 V, with 3 cm long cathodes, a current density of 0.20 A $cm^{-2}$ is achieved for cells with silver strip current-collectors.

Keywords: Solid oxide fuel cell; Current collection

## 4.2 Introduction

The tubular solid oxide fuel cell (SOFC) is based upon a tubular geometry single cell. The advantages of the tubular fuel cell include: the ease of sealing; the ability to cope with higher thermal stresses; rapid response to load variation; tolerance to fuel feed variation; tolerance to load interruption. Power densities of 0.9 $W/cm^2$ have been achieved for certain tubular SOFCs (*5*). Disadvantages of the tubular design include a higher cost of manufacture and the longer current paths which result in significant ohmic losses (*6*).

One of the most prominent tubular SOFC designs is that developed by Westinghouse. It originally consisted of a porous support tube (PST) made from calcia-stabilised zirconia with the cathode, electrolyte and anode layers fabricated over the top, and an interconnect strip joined to the cathode. A later design has dispensed with the performance limiting PST in favour of a thicker walled cathode tube. Fabrication of the Westinghouse design involves the slurry coating of the manganite cathode onto the support tube, followed by a strip of interconnect material ($LaCr(Mg)O_3$) then yttria stabilised zirconia (YSZ) applied by EVD, and finally the addition of the anode, a Ni/YSZ cermet, which is coated on top with EVD and slurry coating. To connect the tubular cells electrically, nickel felt is connected to the interconnect of a tubular cell and to the anode of the adjacent cell. Other tubular designs include the bell and spigot configuration and the segmented-cell-in-series design (*7*). Recently, a novel tubular SOFC design based on small diameter thermally shock resistant zirconia tubes was developed (*8*). A major advantage of this novel tubular design was that it allows for rapid start-up in the order of a few seconds. By contrast, the planar and other tubular designs have typical warm-up times of approximately 6 h and 1 h respectively. Further advantages of this tubular design include low cost manufacture and ease of sealing.

To enable higher voltage outputs (and thus power outputs) the single tubular cells must be stacked into multi-cellular units. Stacking of the single cells is carried out using an electronically conducting interconnect/current-collector for series or parallel

connections. Depending on the fuel cell design, the interconnect must be both chemically and physically stable in reducing and oxidising environments, have good electronic conductivity, have sufficient strength to support other cells (particularly in the planar design) and be easily fabricated into the required configuration. The most common materials used for the interconnect are the alkaline earth-doped lanthanum chromites, used in both the planar and tubular designs, and chromia forming alloys (alloys that form a protective and conductive $Cr_2O_3$ coating) used for the planar design (*9*). Evaporation of chromium from the surface of the metal interconnect on the cathode side has been shown to be detrimental to cell performance. The chromium evaporation can be suppressed, however, by the surface treatment of the alloy separator (*3, 10*). Furthermore, the coating of the metal interconnect with a perovskite has been shown to decrease contact resistance and improve stability of cell performance over time (*3, 11-13*). Alternatively, research revealed that at operating temperatures of around 850-900°C, silver wire wound around the cathode was a simple method of current collection (*1*). Due to the low melting point of silver (*4*), however, the evaporation rate is very pronounced at the present tubular fuel cell operating temperatures (850-900°C). Therefore, either lower operating temperatures would have to be achieved or an alternative to silver would have to be found. Examples of silver used in a SOFC include Ag-$La_{0.7}Sr_{0.3}CrO_3$ (Ag-LSC) cathode cermets, covered with a porous LSC cap, that showed no observed silver segregation, evaporation, or change in interfacial resistance over a 200 h period at 750°C (*14*). Furthermore, earlier research has also shown the use of silver in lowering the cathode interfacial resistance in medium temperature SOFCs run at 750°C (*15*).

In this study, $LaCoO_{3-\delta}$ coated and uncoated Nimonic 90 wire, silver wire and silver strip were studied and compared as potential cathode current-collector/interconnector systems for the novel tubular SOFCs.

# 4.3 Experimental

## 4.3.1 The tubular SOFCs

The ceramic single tubular solid oxide fuel cell consists of an extruded yttria stabilised zirconia (YSZ) electrolyte tube (TZ-8Y, Tosoh Corp.), with an outside diameter and thickness of approximately 2.5 mm and 150 μm respectively. The extrudate was provided by Viking, while the extrusion and subsequent sintering at 1400°C of the electrolyte tubes was performed by SAPCO. A commercial $La_{0.82}Sr_{0.18}MnO_3$ cathode (LSM82X96019-2, Merck) was applied on the outside of the tube and Ni/YSZ ceramic metal composite anode on the inside. The cathode current-collectors consisted of a silver ink painted and then fired onto the surface of the cathode, a commercial 0.32 mm Nimonic 90 wire (Ni53,/Cr20/Co18/Fe5/Ti2.5/Al1.5, Alloy Wire Int.) and a 0.25 mm silver wire wound along the length of the cathode. The novel tubular SOFCs are shown in Fig. 4.1.

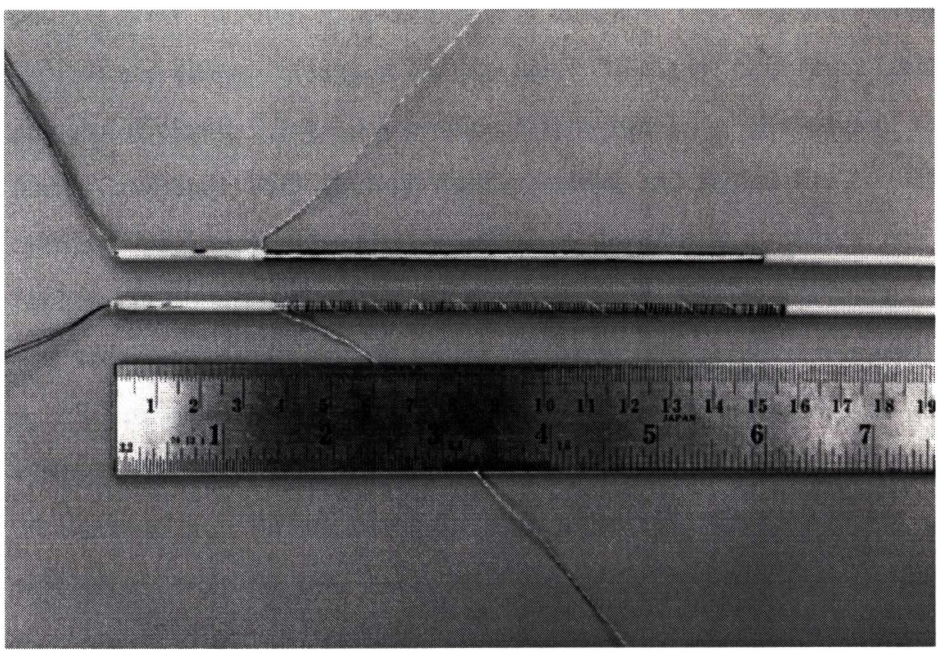

Fig. 4.1. Photograph of the novel tubular SOFCs with 12 cm cathodes (with silver strip and wire current-collectors, respectively).

### 4.3.2 Cathode fabrication

The contacting electrochemical layer was applied using a LSM/YSZ ink; 7.5 g LSM, 7.5 g YSZ (Tosoh TZ10Y), 3.1 g 1,1,1-trichloroethane, 2.3 g methanol and 0.2 g glycerol trioleate were milled with zirconia media for 4 h. The LSM outer layer was prepared from 20 g LSM, 24 g acetone and, 0.6 g KD1 (Zeneca). The first cathode layer, consisting of LSM/YSZ, was then painted by hand, using a brush, onto the outside of the zirconia tube and finally dried in an oven at 140°C for 0.5 h. The second layer, consisting of LSM only, was then applied over the top of the first layer and again dried in an oven.

### 4.3.3 Anode fabrication

The anode was deposited onto the entire inside length of the tubular cells by drawing anode ink up through a cell using a syringe. In order to prepare the anode ink, 5 g of YSZ (Unitec FYT11) was calcined by placing it in a furnace (Carbolite RHF 17/3) and heating at the maximum possible rate to 1500°C, holding for 10 min, and then cooling down to room temperature. The calcined YSZ was then removed from the furnace and sieved through a 212 μm sieve. 10.5 g of NiO (Alfa Chemicals), 0.1 g glycerol trioleate, 2.9 g 1,1,1-trichloroethane and 2.1 g of methanol was added to a plastic container, with zirconia milling media, and milled for 2 h. The previously calcined YSZ was subsequently added to the plastic container and milled for a further 1 h. Finally, 0.1 g PVB (polyvinyl butyral, Aldrich Chemical Company, Inc.) was added to the solution and milled for 2 min. The solution was used immediately. A YSZ tubular cell was attached to a PVC tube that was in turn connected to a syringe. The free end of the cell was then placed in the anode ink. The syringe was then used to draw the anode ink up through the cell to coat the inside, any excess ink was ejected from the tube using the syringe. The cell was initially left to drain and then placed in an oven at 140°C to dry. An anode coating of approximately 40 μm was achieved. After the anodes and cathodes were applied, the cells were fired using a ramp rate of 1°C $min^{-1}$ to 500°C (no dwell), 5°C $min^{-1}$ to 1300°C (dwell 1 h) and then 10°C $min^{-1}$ to room temperature.

### 4.3.4 Fabrication of cathode and anode current-collectors

After firing the electrodes onto the YSZ tube, the current-collectors were added. The cathode current-collector systems used in this work were silver and Nimonic 90 wires wound around the cathodes, and silver ink painted onto the cathodes. The silver wires were wound around the cathodes, and used as a standard to compare the effect the alternative Nimonic 90 wire and silver strip current-collector systems had on fuel cell performance. Before the Nimonic 90 wires were wound around the cathodes, they were coated with $LaCoO_{3-\delta}$. The latter compound was chosen because it has exhibited low contact resistances (*3*). $LaCoO_{3-\delta}$ perovskite powders used for the coating of the alloy wires were synthesised using the glycine nitrate process (*16*). A slurry system was then developed to coat the cathode wire. The system is shown in Table 4.1. The appropriate amounts of perovskite powder, solvent (consisting of 31% toluene and 69% 2-propanol) and dispersant were mixed in a beaker for 1 h using a magnetic stirrer. The binder and plasticiser were subsequently added, and mixing continued for a further 1 h. Solvent was evaporated off, until a thick 'honey-like' consistency was obtained. A perovskite coating of approximately 20 μm was achieved by drawing Nimonic 90 alloy wire at a constant rate through a syringe containing the slurry. The needle end of the syringe, through which the wire emerged, was covered in plasticine. The plasticine stopped the solution from escaping and aided the coating of the wire. The coating was then dried in air for approximately 6 h, after which the coated and uncoated wires were wound around their respective cathodes on the tubular cells, and fired at a rate of 5°C $min^{-1}$ in air to 1200°C, dwelled for 1 h and then cooled down to room temperature at a rate of 10°C $min^{-1}$. The effect that the coating on the Nimonic 90 wires had on cell performance was then measured.

Table 4.1. Weight percentages (wt.%) of dispersant, plasticiser and binder relative to the weight of the $LaCoO_{3-\delta}$.

| Dispersant wt.% | Binder wt.% | Plasticiser wt.% |
|---|---|---|
| KD1 | PVB6:20Epoxy | PEG4:DOP4:Terp3 |
| 3 | 26 | 11 |

DOP is Di-octyl-phthalate, PEG is poly (ethylene glycol), PVB is polyvinyl butyral, Terp is Terpineol.

Unless otherwise stated, the silver strip current-collector was applied by painting two silver ink strips (product C 10503D1, Gwent Electronic Materials Ltd. UK), approximately 1 mm in width, on opposite sides along the length of the surface of the individual cathodes. The cells were then dried in an oven for 15 min at 140°C and then fired. The firing took approximately 40 min, with a dwell period of 6 min, at a maximum temperature of 800°C. Silver wire leads were then attached to the cathode silver strip current collects by winding the silver around the tubes to contact the end of the silver strips. To ensure intimate contact between the wire and the strip, silver ink was painted onto the contacting area, dried and then fired as above.

The anode current-collector consisted of two 0.5 mm Ni wires (99.98%, Advent Research Materials Ltd.) placed down the inside of the tube, whereby the two Ni wires remained in contact with the anode purely by mechanical force exerted by the wires on the inside of the tube.

### 4.3.5 SOFC testing

The cells were placed in a purpose-built furnace. A gas line connected to a dual supply of $H_2$ and $N_2$ was then attached to the end of the cell, while the current collecting, and associated reference and sensing wires for the electrodes, were brought outside the furnace. Before testing, the cells were heated in the furnace to 900°C, while $N_2$ was passed through the tube. Upon reaching 900°C the $N_2$ supply was slowly turned off as $H_2$ was added. The anode was then reduced by passing pure $H_2$, at a rate of 25 $cm^3$ $min^{-1}$, bubbled through water at 25°C, through the cell for

15 min. The current-voltage characteristics (I-V) of the cells were then measured using a passive potentiostat (*17*) in air at a constant temperature of 900°C, and constant flow rate of 25 $cm^3$ $min^{-1}$ $H_2$. The contact resistance was ascertained by measuring the potential difference between the cathode current collect and a small sensing electrode adjacent to the current-collector on the same cathode. The cathode resistance was determined by the potential difference between the sensing electrode on the cathode and a reference electrode adjacent to the cathode.

## 4.4 Results and discussion

An issue which proved challenging was the adherence of the coating to the wire before and after firing. A lanthanum cobaltite slurry had to be developed that would adhere to the wire during winding onto the cathode. This was achieved using the formulation detailed in Table 4.1. A Hitachi S4000 scanning electron microscope (SEM) was used to analyse the surface morphology of the perovskite coating on the wire after testing. The coating did not adhere well to the metal wire. Cobalt-containing perovskite materials previously used as coatings to reduce contact resistance, and Cr evaporation, on the metal interconnect have also exhibited poor adherence to the interconnect after testing (*3*). It is evident, however, that when a comparison is made between the uncoated and coated Nimonic 90 wires, as shown in Fig. 4.2(a, b), the coating does appear to improve the overall cell performance. For example at 0.7 V, as shown in Table 4.2, Nimonic 90 coated wires had a contact voltage of 0.239 V and a current density of 0.049 A $cm^{-2}$ compared to a contact voltage of 0.322 V and current density of 0.034 A $cm^{-2}$ for the uncoated Nimonic 90 wires. Previous research by other authors on planar cells has yielded similar results (*3, 11, 12*).

Table 4.2. I-V characteristics of silver and Nimonic 90 alloy wire current collection systems at 0.7 V for 3 cm cells.

| Current collect | Average current density (A $cm^{-2}$ at 0.7 V) | Cathode voltage V | Contact voltage V |
|---|---|---|---|
| Uncoated Nimonic 90 | 0.034 | 0.376 | 0.322 |
| Coated Nimonic 90 | 0.049 | 0.356 | 0.239 |

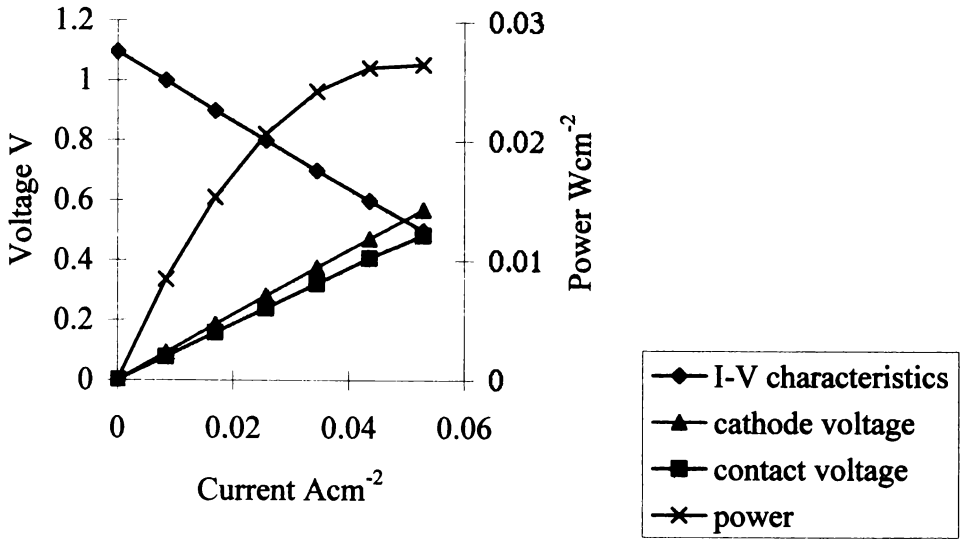


(a)

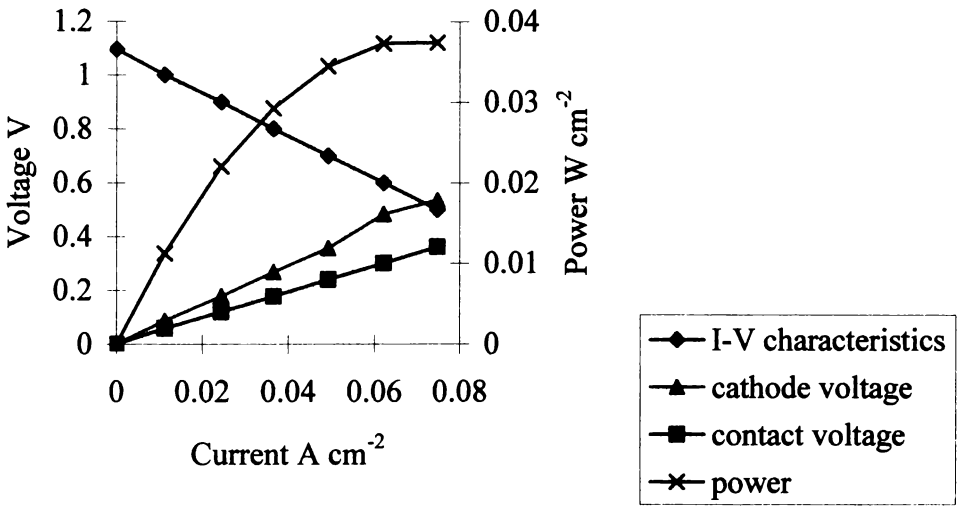


(b)

Fig. 4.2. I-V characteristics for 3 cm fuel cells measured in air at a constant temperature of 900°C and a constant flow rate of saturated $H_2$ bubbled through $H_2O$ at 25 $cm^3$ $min^{-1}$: (a) uncoated Nimonic 90 wire; (b) Nimonic 90 coated with $LaCoO_{3-\delta}$.

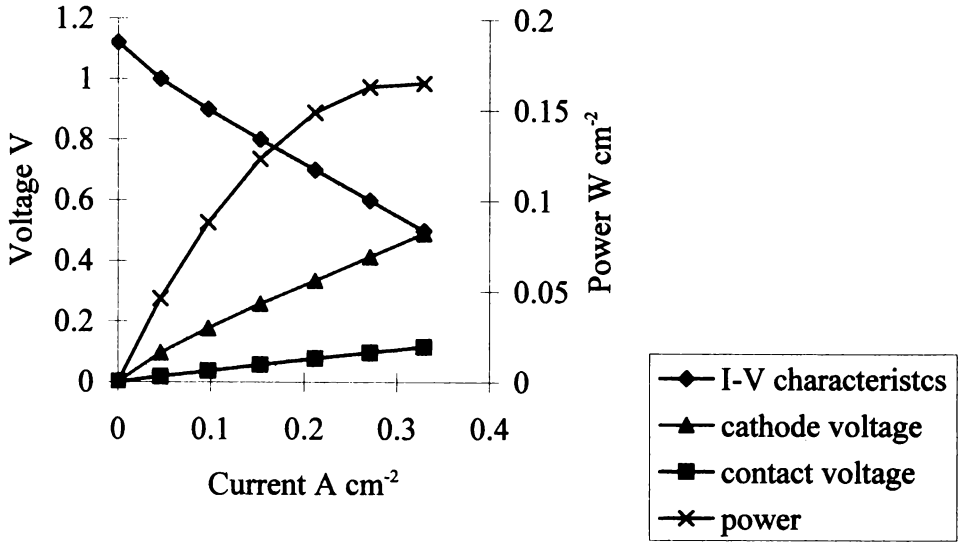


(a)

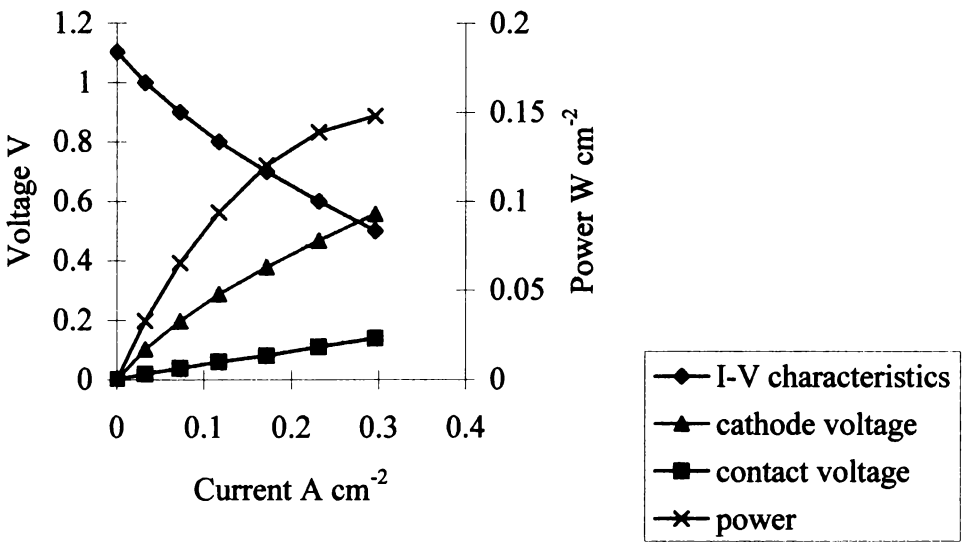


(b)

Fig. 4.3. I-V characteristics for 3 cm fuel cells measured in air at a constant temperature of 900°C and constant flow rate of saturated $H_2$ bubbled through $H_2O$ at 25 $cm^3$ $min^{-1}$: (a) silver wire; (b) silver strip.

The I-V characteristics, total cathode contribution to resistance and the contact contribution to resistance are presented and in Fig. 4.3(a, b) for the silver wire and the strip current-collectors, respectively. As shown in Table 4.3, both the silver wire and the silver strip have similar values of contact voltage and cell current densities. Both methods of current collection exhibit superior performance over the Nimonic 90 coated and uncoated wires. An electron micrograph of the LSM/Ag strip interface is given in Fig. 4.4.

Table 4.3. I-V characteristics of the silver wire and silver strip cathode current collects at 0.7 V for 3 cm cell lengths.

| Current collect | Current density ($A\ cm^{-2}$ at 0.7 V) | Cathode voltage V | Contact voltage V |
|---|---|---|---|
| Silver wire | 0.21 | 0.34 | 0.08 |
| Silver strip | 0.20 | 0.38 | 0.08 |

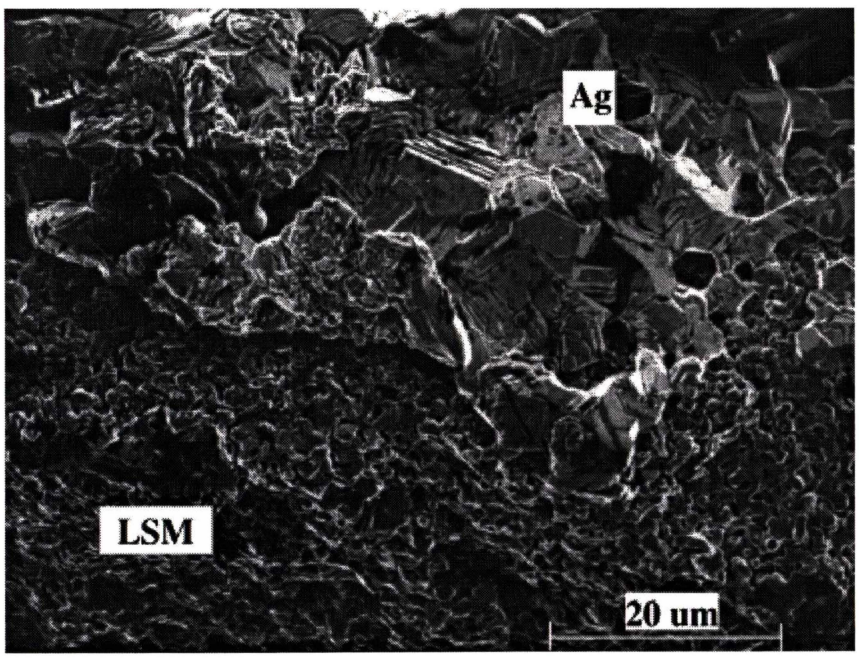


Fig. 4.4. Electron micrograph of LSM/Ag interface.

To ascertain the effect of cell length on performance, cells were fabricated with cathodes of length 3 and 12 cm, the results listed in Table 4.3 and Table 4.4 reveal, that the silver strip performs as well as the silver wire over different cell lengths. The

current density for the 3 cm cells was much higher than that of the longer 12 cm cells. The results are in agreement with similar work carried out previously, whereby current densities decreased with increasing cell length (*1*).

Table 4.4. Current densities of 12 cm long cathodes at 0.7 V.

| Length | Average current density ($A\ cm^{-2}$ at 0.7 V) |
|---|---|
| 12 cm silver strip | 0.087 |
| 12 cm silver wire | 0.074 |

In order to assess the quantity and coverage of silver that is needed to deliver maximum cell performance using the silver ink, various coverages of silver ink were applied to the cathodes. Listed in Table 4.5 are the two silver coverages, along with their corresponding current densities, held at a constant potential of 0.7 V. The current density of the two cells is similar. For example, the cell with a cathode covered completely in silver ink gave a similar current density as the cell with two strips of silver along the length of the cell cathode. In addition, the cell with the cathode covered completely in silver performs adequately. This indicates that the presence of silver does not effect cell cathode performance because it is permeable to oxygen. The difference in current density between the cells described in Table 4.3 and Table 4.5 is ascribed to the cells being made from different batches of cathode and anode inks.

Table 4.5. Current densities of 3 cm cells with different coverages of silver current collect ink at 0.7 V.

| Coverage | Average current density ($A\ cm^{-2}$ at 0.7 V) |
|---|---|
| Two thin silver strips painted along the cathode | 0.11 |
| Silver painted over the entire cathode | 0.12 |

## 4.5 Conclusions

The coating of Nimonic 90 wires with $LaCoO_{3-\delta}$ is shown, to a limited extent, improve cell performance by reducing the contact resistance between the wires and the cathode. The use of Nimonic 90 wires is, however, an unsatisfactory method of cathode current-collection for the novel tubular SOFC used in this work as the overall cell performances are well below that achieved for alternative silver wire or strip current-collectors.

From the experimental data, it is found that the silver strips painted on to the surface of the cathodes perform as well as the silver wire, and may prove to be a useful means of current collection in low temperature SOFCs. In addition, it is observed that the current density is not improved dramatically by an increase in the area of cathode covered by silver. This suggests that the silver does not interfere with the cathode reaction. The current increases with increase in the contact area of the cathode, but not proportionally.

## 4.6 References

1. I. P. Kilbride, J. Power Sources **61**, 167 (1996).
2. W. Köck, H. P. Martinz, H. Greiner, and M. Janousek, in "Proceedings of the Fourth International Symposium on Solid Oxide Fuel Cells (SOFC-IV)" (M. Dokiya, O. Yamamoto, H. Tagawa, and S. C. Singhal, eds.), p. 841. The Electrochemical Society Inc., Yokohama, Japan, 1995.
3. H. Schmidt, B. Brückner, and K. Fischer, in "Proceedings of the Fourth International Symposium on Solid Oxide Fuel Cells (SOFC-IV)" (M. Dokiya, O. Yamamoto, H. Tagawa, and S. C. Singhal, eds.), p. 869. The Electrochemical Society Inc., Yokohama, Japan, 1995.
4. P. Kofstad and R. Bredesen, Solid State Ionics **52**, 69 (1992).
5. H. Sasaki, S. Otoshi, M. Suzuki, T. Sogi, A. Kajimura, N. Sugiura, and M. Ippommatsu, Solid State Ionics **72**, 253 (1994).
6. D. C. Fee, S. A. Zwick, and A. P. Ackerman, in "Proceedings of the Conference on High-Temperature Solid Oxide Electrolytes", Vol. 1, p. 29.
7. N. Q. Minh, J. Amer. Ceram. Soc. **76**, 563 (1993).
8. K. Kendall and M. Prica, in "Proceedings of the First European Solid Oxide Fuel Cell Forum" (U. Bossel, ed.), Vol. 1, p. 163, Lucerne, Switzerland, 1994.
9. M. Dokiya, T. Horita, N. Saki, T. Kawada, H. Yokokawa, B. A. van Hassel, and C. S. Montross, in "14th Risø International Symposium on Material Science" (F. W. Poulsen, J. J. Bentzen, T. Jacobsen, E. Skou, and M. J. L. Østergard, eds.), p. 33, 1993.
10. Y. Akiyama, S. Taniguchi, T. Yasuo, M. Kadowaki, and T. Saitoh, J. Power Sources **50**, 361 (1994).
11. T. Kimura, T. Namikawa, and Y. Yamazaki, Denki Kagaku **61**, 1115 (1993).
12. T. Kadowaki, T. Shiomitsu, E. Matsuda, H. Nakagawa, H. Tsuneizumi, and T. Maruyama, Solid State Ionics **67**, 65 (1993).
13. T. Shiomitsu, T. Kadowaki, T. Ogawa, and T. Maruyama, in "Proceedings of the Fourth International Symposium on Solid Oxide Fuel Cells (SOFC-IV)"

(M. Dokiya, O. Yamamoto, H. Tagawa, and S. C. Singhal, eds.), p. 850. The Electrochemical Society Inc., Yokohama, Japan, 1995.

14. L. S. Wang and S. A. Barnett, Solid State Ionics **76**, 103 (1995).
15. L. S. Wang and S. A. Barnett, J. Electrochem. Soc. **139**, L89 (1992).
16. L. A. Chick, L. R. Pederson, G. D. Maupin, J. L. Bates, and J. G. Exharhos, Mater. Lett. **10**, 1 (1990).
17. R. C. Copcutt, in "Electrochem. 95", University of Wales. Bangor, UK, 1995.

# Chapter Five

## *Fabrication and Properties of $Ce_{0.8}Gd_{0.2}O_{1.9}$ Electrolyte-Based Tubular Solid Oxide Fuel Cells*

Submitted to: *Solid State Ionics* (1998).

# *Introductory note*

The purpose of the research described in this Chapter was to fabricate medium temperature $Ce_{0.8}Gd_{0.2}O_{1.9}$ electrolyte based tubular SOFCs.

Pastes containing $Ce_{0.8}Gd_{0.2}O_{1.9}$ ceramic powder and organic additives were extruded to form hollow electrolyte tubes. Various methods to improve the microstructure of the tubes were studied, these included changes in ceramic powder morphology by heat-treatments, and modification of the organic additives. The organic additives were burnt-out and the tubular electrolyte sintered. The microstructures of these tubes were then examined. The effect sintering regimes had on the grain size and surface porosity of the sintered tubes was also investigated (Appendix B).

Dense gas-tight electrolyte tubes were successfully fabricated. Electrodes and current collectors were applied to the electrolyte tube and the cell electrically tested. Silver wire was used as the cathode current collector for initial tests as it was easier to fabricate, and performed as well as the silver strip coatings investigated in Chapter Four. Cell testing was successful, as the I-V characteristics obtained were similar in form to the I-V characteristics of $Ce(Gd)O_{2-x}$ based SOFCs fabricated by Zheng et al. (*1*) (see Section 1.5.1.4).

Chapter Six then examines an alternative method of current collection to the silver and Nimonic 90 wire methods studied in Chapters Four and Five. As a medium temperature SOFC was fabricated, it was envisaged silver composites could be incorporated into the current collect design.

Submitted to: *Solid State Ionics* (1998).

# Fabrication and Properties of $Ce_{0.8}Gd_{0.2}O_{1.9}$ Electrolyte-Based Tubular Solid Oxide Fuel Cells

C. Hatchwell and N. M. Sammes

Department of Technology, The University of Waikato, Private Bag 3105, Hamilton, New Zealand

I. W. M. Brown

Industrial Research Limited, PO Box 31-310, Lower Hutt, New Zealand

## 5.1 Abstract

A general procedure for the extrusion of $Ce_{0.8}Gd_{0.2}O_{1.9}$ tubular electrolytes is detailed. Using a commercial water based binder system, $Ce_{0.8}Gd_{0.2}O_{1.9}$ was extruded, then fired at 1600°C to form high-density electrolyte tubes (98% relative to theoretical). Heat-treatment of the $Ce_{0.8}Gd_{0.2}O_{1.9}$ powder at 900°C for 4 h yielded tubes that were highly dense with a smooth surface finish while non heat-treated powders resulted in an extrusion that was less dense with poor surface finish. Electrodes were applied and the tubular SOFC was electrically tested. A good open circuit voltage of 0.911 V was achieved for the cell, however, a poor operating current density of 0.0123 A $cm^{-2}$ at 0.7 V was obtained.

The results demonstrate the potential of fabricating and operating tubular SOFCs.

Keywords: Cerium oxide; Ceria; Extrusion; Solid Oxide Fuel Cell.

## 5.2 Introduction

Solid oxide fuel cells (SOFC) are high efficiency energy conversion devices that produce electricity by electrochemical reaction of a fuel with an oxidant. Fuel cells characteristically have high energy conversion efficiencies, reduced pollutant emissions, the potential for co-generation in high temperature systems, the ability to be powered on a wide range of fuels and the potential to be manufactured at low cost. The majority of fuel cell applications are envisaged to be in both the transportation industry and in the efficient production of localised and centralised power (*2*).

A typical SOFC consists of an electrolyte such as yttria stabilised zirconia (YSZ), with a Ni-YSZ fuel electrode (anode) and an $(LaSr)MnO_3$ air electrode. The single fuel cell units consisting of anode/electrolyte/cathode are connected electrically using an interconnect such as $(La,Sr)CrO_3$. As the mobility of the oxygen ions in the YSZ electrolyte is a thermally activated process, this type of SOFC operates at temperatures of approximately 900-1000°C, to achieve sufficient oxide ion mobility in the electrolyte. These high operating temperatures are inconvenient, as the selection of materials is severely limited due to chemical reactivity and stability of the various components at high operating temperatures (*3, 4*). A reduction in the operating temperature by reducing the electrolyte thickness and/or using a lower temperature electrolyte, such as $Ce_{0.8}Gd_{0.2}O_{1.9}$ (CGO) (*1, 5, 6*), would allow for greater materials selection. For example, in the planar design, a reduction in operating temperature to 650°C would allow the use of a stainless steel interconnect instead of the comparatively high cost $(La,Sr)CrO_3$.

In addition to the planar SOFC design there is also the tubular design. Major advantages of the tubular SOFC over the planar include the capacity to cope with higher thermal stresses, ease of sealing, quick response to load variation, tolerance to fuel feed variation and tolerance to load interruption (*2*). Previously, a novel tubular SOFC design, based on small diameter thermally shock resistant YSZ tubes, was developed. In contrast to planar and certain other tubular designs, that take 6 h and

1 h respectively to reach operational temperature, the novel thermally shock resistant tubes have start-up response times that are in the order of a few seconds (*7-9*).

This paper details the preparation of small diameter CGO tubes by way of extrusion, in order to combine the advantages of using a lower temperature electrolyte with small diameter highly thermally shock resistant tubular design.

## 5.3 Experimental

The procedure used to prepare CGO tubular fuel cells involving various processing steps is detailed below.

### 5.3.1 Powder processing

As the particle size distribution and specific surface area of the ceramic powder are very important parameters in obtaining a highly dense extruded ceramic, it was necessary to modify the as-received powder particle size/surface area by heat-treatment. Various heat-treatment times and temperatures were used and are described in Table 5.1. Particle size analysis was performed using a Shimadzu, SALD-2001 (SALD-2001-ATA2:V1.00) particle analyser. A balance between particle size and amount of organic additives was necessary to obtain highly dense extruded ceramic tubes. The heat-treatments were performed using a muffle furnace (Carbolite).

Table 5.1. The powder, calcination and milling times plus respective particle size and surface area of the ceramic powders used in this study.

| Sample | Powder | Calcination temperature (°C) and time (h) | Milling time (h) | Mean particle size (μm) | BET Surface area ($m^2 g^{-1}$) |
|---|---|---|---|---|---|
| 1 | $Ce_{0.8}Gd_{0.2}O_{1.9}$ | - | - | nano crystalline | 120-140 |
| 2 | $Ce_{0.8}Gd_{0.2}O_{1.9}$ | 650°C/4 h | - | 9 | 12.2 |
| 3 | $Ce_{0.8}Gd_{0.2}O_{1.9}$ | 1000°C/4 h | 24 h | 2 | < 1 |
| 4 | $Ce_{0.8}Gd_{0.2}O_{1.9}$ | 900°C/4 h | - | 21 | 9.5 |
| 5 | $Ce_{0.8}Gd_{0.2}O_{1.9}$ | 900°C/4 h | - | 21 | 9.5 |

CGO was milled for 24 h in ethanol in a 250 ml Nalgene container with zirconia grinding media. Table 5.1 describes the powder examined, the calcination and milling times, plus the respective particle size and surface area of the ceramic powders used in this study.

## 5.3.2 Paste preparation

A commercial ceramic powder, $Ce_{0.8}Gd_{0.2}O_{1.9}$ (CGO) (NexTech Materials, Ltd. Worthington, OH) was used in this work. Extrudates (green ceramic body containing the ceramic and extrusion aids), with the correct properties for extruding into tubes, were fabricated using a number of different fabrication regimes. In this work, it was decided to study a water-based system, rather than the more conventional organic-based systems (initial studies had shown the ceramic powder to be stable in water). Commercial water based binders B-1051 and B-1052 from the Duramax™ range of ceramic additive polymers specific to extrusion were employed (Rhom and Haas-Formulation Chemicals).

Table 5.2. Weight percentages (wt.%) of organic additives relative to the weight of ceramic powder.

| Sample | PEG-400 1:10 distilled water (wt.%) | AMP-95™ (wt.%) | Duramax™ Binders B1-1051 (wt.%) | Duramax™ Binders B1-1052 (wt.%) | Distilled Water, (wt.%) |
|---|---|---|---|---|---|
| 1 | 10.0 | 4.7 | 11.9 | 6.6 | 25.1 |
| 2 | 7.3 | 1.7 | 8.2 | 4.9 | 13.7 |
| 3 | 6.7 | 1.9 | 8.0 | 4.7 | 8.4 |
| 4 | 6.9 | 1.8 | 8.4 | 4.6 | 8.1 |
| 5 | 6.9 | 1.8 | 8.2 | 4.9 | 12.1 |

Table 5.2 describes the various paste formulations examined in this study. 100 g of CGO and 0.5 g PEG-400 (Union Carbide Co., Danbury, CT), pre-dispersed in various wt.% of distilled water, were mixed using a high shear mixer for 2-3 min. Between 1.7 and 4.7 wt.% of AMP-95 (Angus Chemical, Buffalo Grove, IL) was then added and mixed for 5 min. Various wt.% of the Duramax™ binders, B-1051 and B-1052, were then added to the whole and mixed for a further 5 min. Finally, various wt.% of de-ionised water was added and mixed for a final 5 min. After addition of the water, and appropriate mixing, the resulting extrudate was placed inside a plastic bag, pressed flat in an uni-axial press using between 3 and 6 MPa, folded twice then pressed again. This pressing/folding process, was carried out to simulate shearing conditions, and was repeated until the system appeared properly mixed. A plastic bag was used to stop evaporation of solvent and to keep the extrudate clean. The sample was finally left to age, in air, overnight. It is also note worthy that mixing times were only approximate and depended on the consistency of the mixtures between addition of components.

### 5.3.3 Extrusion apparatus

The extrusion of the tubular CGO cells was performed using an in-house designed high strength steel piston extruder. To reduce friction between the die wall and extrudate, surfaces in contact with the extrudate in the die head were polished using 1 μm diamond paste. The diameter of the exit hole was 3.38 mm and the diameter of the pin was 3.15 mm. A PTFE 2 cm long plug, approximately 0.3 mm larger than piston bore (such that a push fit seal was obtained), was placed between the metal piston and the extrudate, and was used as a seal to stop the extrudate from jamming the piston. After the extrudate was located in the piston hole with the PTFE seal and piston on top, the die was placed on a stand on a Instron 25 kN testing machine. The piston was forced down at a constant rate of 2.5 mm $min^{-1}$. The extrudate was then forced through the die to form a tube. The resulting green tube was placed into corrugated or v-shaped card-board holders and dried in air for 24 h. Two glass stirring rods were positioned along the length of the each tube to help prevent

warping during drying. Finally the tubes were placed in 1/4 round tubes of $Al_2O_3$ in an oven at 120°C for a further 1 h to dry.

### 5.3.4 Binder burnout

In order to obtain a successful firing regime to burn out organics before sintering, the ceramic tubes were placed in a thermal gravimetric analysis (TGA)/binder burnout furnace to record the mass loss over increasing time and temperature. The sample was placed on a sample stage, a flat silica glass plate, inside a vertically mounted tubular furnace. The sample stage was in-turn connected to a balance (Metler Toledo with LC-R terminal) located outside the furnace, that was used to detect the changes in the weight of the sample. The weight and temperature changes were recorded using a computer data logging system.

Sintering of the ceramic tubes was carried out in a chamber furnace (Ceramic Engineering), using a Eurotherm temperature controller and Super Kanthal heating elements. The electrolytes sitting in 1/4 round tubes of $Al_2O_3$ were placed in the furnace to be fired. Microstructural and compositional analysis was performed using a Cambridge Stereoscan MkII scanning electron microscope (SEM) equipped with Oxford-Link energy dispersive X-ray analysis.

### 5.3.5 Application of electrodes

Exact details of the cell fabrication and electrical measurements can be found in a previous paper (*10*). The Ni-YSZ anode was applied first down the inside the tube by drawing anode ink up through the cell using a syringe. The anode was then left to dry and then fired at 1300°C for 1 h (heating and cooling rates of 5°C $min^{-1}$). Cathode inks were applied by brush to the outside of the cells which consisted of a contacting layer applied directly to the surface of the cell and a current collecting layer applied directly over the top of the first layer. The contacting layer consisted of a 2:1 ratio of

$La_{0.6}Sr_{0.4}CoO_3$ to CGO, while the current collecting layer was $La_{0.6}Sr_{0.4}CoO_3$. The 12 cm long cathode was then fired in air at 1200°C for 1 h.

### 5.3.6 Current collection

The anode current collector was composed of 2 Ni wires (99.98%, Advent Research Chemicals), 0.5 mm in diameter forced down the centre of the tube. The cathode current collect was 0.25 mm diameter Ag wire (Advent) wound around the outside of the cathode.

### 5.3.7 Cell testing

The tubular cell was then placed inside a purpose built furnace with associated connected current collecting wires and $H_2$ supply leading outside the furnace. Before testing, the Ni-YSZ anode was reduced by heating the tube to 600°C in air then introducing $H_2$ bubbled through water at a constant 25°C at a rate of 25 $cm^3$ $min^{-1}$ for 15 min. The I-V characteristics of the cell were then measured using a potentiostat (PGP201 Potentiostat/Galvanostat, Radio Copenhagen) in air at a constant temperature of 600°C, and constant flow rate of 25 $cm^3$ $min^{-1}$ $H_2$.

## 5.4 Results and discussion

### 5.4.1 Fabrication

As described in the literature (*11*), the powder particle size/distribution and morphology play an important role in the quality of the final extruded product. For example, ceramic powder with particle size below 1 μm is said to have lower number of problems associated with extrusion than ceramic powder above 1 μm. In contrast, powders with high surface areas require larger amounts of organic additives to

produce ceramic pastes. The large amount of additives necessary to achieve this, results in very low green densities, making it extremely hard to obtain high sintered densities (*12*). Therefore, to understand the relationship between particle size/amount of organic additives and final sintered density, as-received (submicron)/heat-treated and milled powders were used to establish the amounts of organic additives necessary to extrude CGO. These processing parameters were then related to the quality of the final sintered tube.

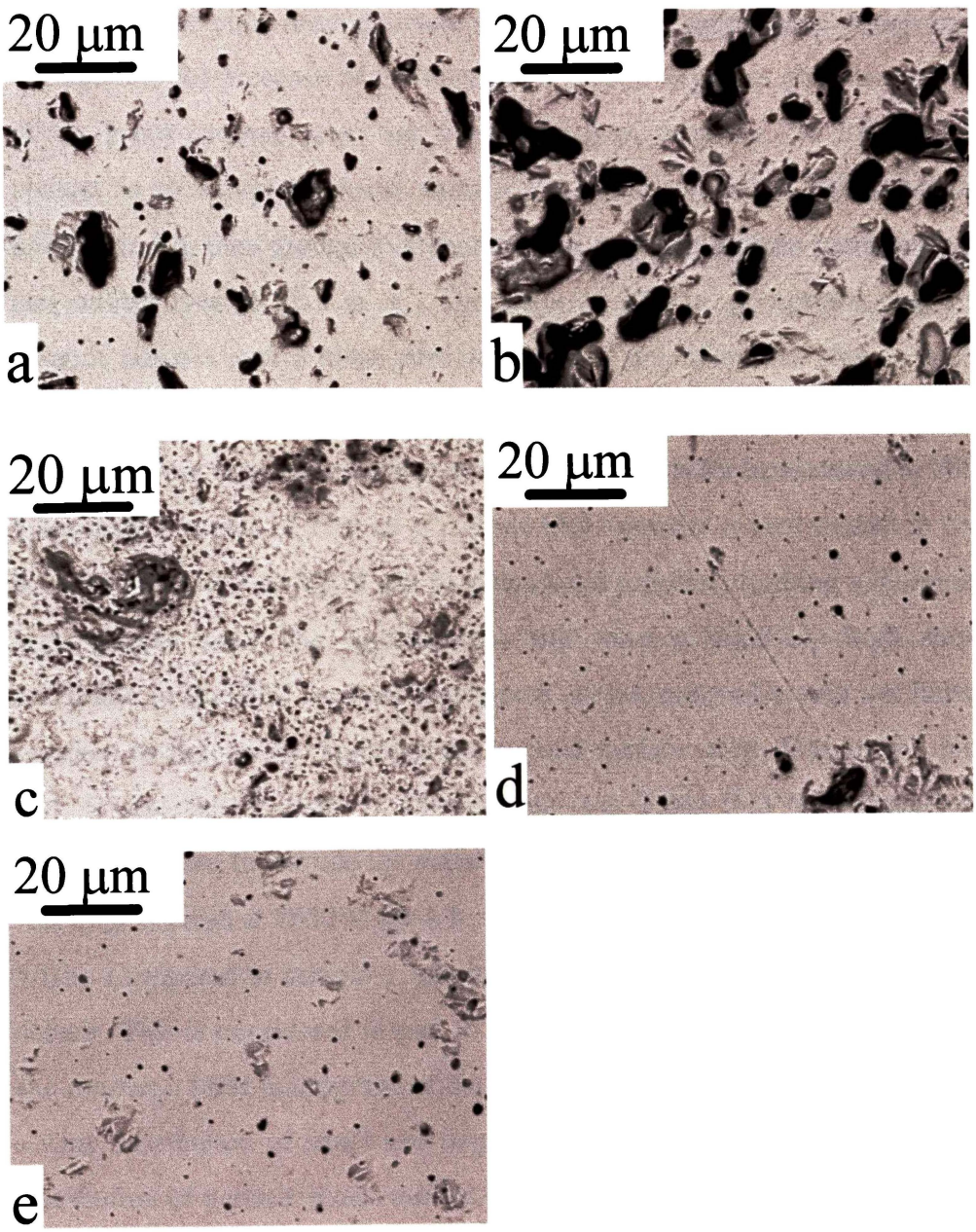


Fig. 5.1. SEM micrographs of the polished cross-sections of the sintered CGO extruded tubes; (a) sample 1; (b) sample 2; (c) sample 3; (d) sample 4; (e) sample 5.

For sample 1, as-received CGO was used. 58.3 wt.% of organic additives was necessary to achieve an extrudable paste. A high proportion of organic additives was required because of the low particle size and high surface area of the powder; this required a high proportion of organics to coat the particles to form an extrudable paste. Upon extrusion the surface of the extruded tube was rough in comparison to the inside surface of the cell. The SEM micrograph of a polished cross-section of the extruded tube sintered at 1550°C is shown in Fig. 5.1(a). A high proportion of defects in the sintered ceramic sample can be seen. The presence of the defects was ascribed to the poor microstructure of the extruded green tube, which in turn was attributed to the presence of the high proportion of organics (thus low green density of the green ceramic tube) and poor mixing of organics. To reduce the organic content to an acceptable level, sample 2 was pressed into a pellet, heat-treated at 650°C for 4 h, then ground in a hand-mortar, yielding a mean particle size of 9 μm and surface area of 12.2 $m^2 g^{-1}$. The value of 12.2 $m^2 g^{-1}$ appears very high for a ceramic powder with a mean particle size of 9 μm. However, this anomaly can be explained with reference to the high surface area of the powder obtained when heat-treated at lower temperatures. For example, CGO powder heat-treated at 700°C for 4 h has a surface area of 32.9 $m^2 g^{-1}$. When CGO powder is heat-treated in pellet form for a period of 4 h at 650°C the particles bond together, forming agglomerates with high particle size. The agglomerates still have a relatively high surface area accessible to the BET analysis instrument, as the material would not have sintered together to reduce the agglomerate internal surface area. Due to the increase in particle size and decrease in surface area (see Table 5.1) the amount of organic additives needed to extrude the material was reduced to a total of 36 wt.%. The tube was then sintered at 1650°C for 6 h; the resulting SEM micrograph is shown in Fig. 5.1(b). Compared to sample 1, sample 2 has a higher and larger proportion of hole defects. This is considered in-part to be due to poor grinding when using the pestle and mortar; a SEM micrograph of the powder taken after grinding showed there to be a wide distribution of small and large agglomerates. It is considered that this wide distribution of particle sizes resulted in the prominence of a high number of defects due to improper packing and/or alignment of the ceramic particles during extrusion. Therefore, it was considered necessary to mill all further samples of the heat-treated

powder before addition of the organic extrusion aids to reduce particle size distribution.

The preparation of sample 3 is detailed in Table 5.1 and Table 5.2. After heat-treatment of sample 3 at 1000°C for 4 h, the pellet was ground then milled for 24 h. Milling was expected to reduce both particle size distribution and mean particle size. As sample 3 had a lower mean particle size (2 μm) than sample 2 it was expected that the surface area of sample 3 would have been higher than the 12.2 $m^2 g^{-1}$ attained for sample 2. However, the actual surface area achieved for sample 3 was below the 1 $m^2 g^{-1}$ detection limit. The reason for the very low surface area was attributed to the higher sintering temperature of 1000°C for 4 h in pellet form (which would reduce the internal surface area of the particles). Therefore it was assumed the particles had a higher density and thus reduced porosity due to the higher heat-treatment temperature. Furthermore, it was also assumed that the ceramic powder morphology was altered to such an extent as to reduce the surface area of the particles. A reduced surface area resulted in a lower proportion of organics being added. Upon extrusion, tubes were soft and deformed under their own weight. The cause of deformation was postulated as being due to the sample having too much organic additive relative to the surface area (which seems a contradiction as the wt.% of the additives was actually decreased), where increased amounts of organic additive relative to surface area would effectively increase the plasticity of the extrudate. Another possible cause of deformation was not enough wt.% of the rigid binder B1-1051. The outside surface texture of the extruded tube was rough while the inside was smooth. The SEM micrograph of the polished cross-section of the sintered tube (shown in Fig. 5.1(c)), fired at 1500°C for 2 h, showed the size of the hole defects to have been dramatically decreased, however the proportion of defects was still unacceptable.

It was decided that calcination of the powder (sample 3, Table 5.1) in pellet form and subsequent milling stage was resulting in a particle size and morphology that was still detrimental to extrusion, such that poor sintered density, and surface finish, were the result. Therefore, it was decided to heat-treat the as-received material in powder form (sample 4). As shown in Table 5.1, the raw powder was heated at 900°C for 4 h, and yielded a surface area of 9.5 $m^2 g^{-1}$ with mean particle size of 21 μm.

As the relative amount of organics to surface area was effectively reduced, it was hoped that the stiffness of the extrudate would be improved. Furthermore, it was considered necessary to increase the rigid component of the extrudate, binder B1-1051, and decrease the more plastic component, in this case binder B1-1052. The rigidity and plasticity of the two binders being associated with their glass transition temperatures (Tg); where the B1-1051 has a Tg of 81°C, while the Tg of B1-1052 is 6°C. After extrusion at approximately 7 kN, the resulting tubes were rigid (maintained shape) with a smooth surface texture, however appearance of wear on the die surfaces was an indication that the pressure was too high. The tubes were fired at 1600°C for 2 h. The SEM micrograph, Fig. 5.1(d), of the polished cross-section of the extruded tube, shows the sample to be very dense and relatively defect-free in comparison to samples 1-3.

The surface SEM micrograph of the tube given in Fig. 5.2, reveals the grains to be between 3-10 μm in size and the surface to be free of porosity, indicating the sintering temperature to be suitable for this sample.

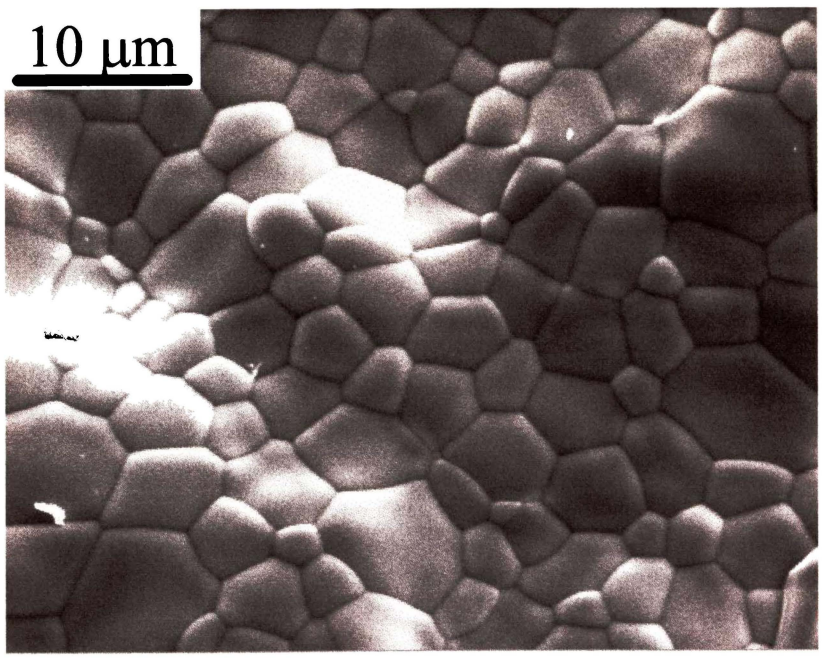


Fig. 5.2. SEM micrograph of the surface of sample 4, sintered at 1600°C/2 h.

Although sample 4 was successfully extruded, it was necessary to reduce the die wear by making the extrudate more plastic. However, there was a competing need for rigidity of the tube to stop deformation under its own weight. Thus, to reduce die wear, due to the high pressure required to force the paste through the die, and to maintain structural integrity of the tube upon extrusion, the overall binder content was increased for the more plastic binder. As shown for sample 5 in Table 5.2, the amount of binder B1-1051 was decreased (more rigid binder) while B1-1052 (more plastic binder) was increased, increasing the overall binder content. The desired result was achieved, with a decrease in extrusion pressure of between 4.4-4 kN and maintenance of structural integrity of the tube. The polished SEM micrograph of the sample 5 tube, sintered at 1600°C for 2 h, is given in Fig. 5.1(e) and shows a highly dense ceramic with few defects; the theoretical density achieved was 98%. The outside diameter and thickness of the sintered tubes were approximately 3.14 mm and 400 μm respectively. A photograph of the sintered tube is given in Fig. 5.3. Electrodes were applied to the sintered tubes and then current-voltage (I-V) characteristics determined.

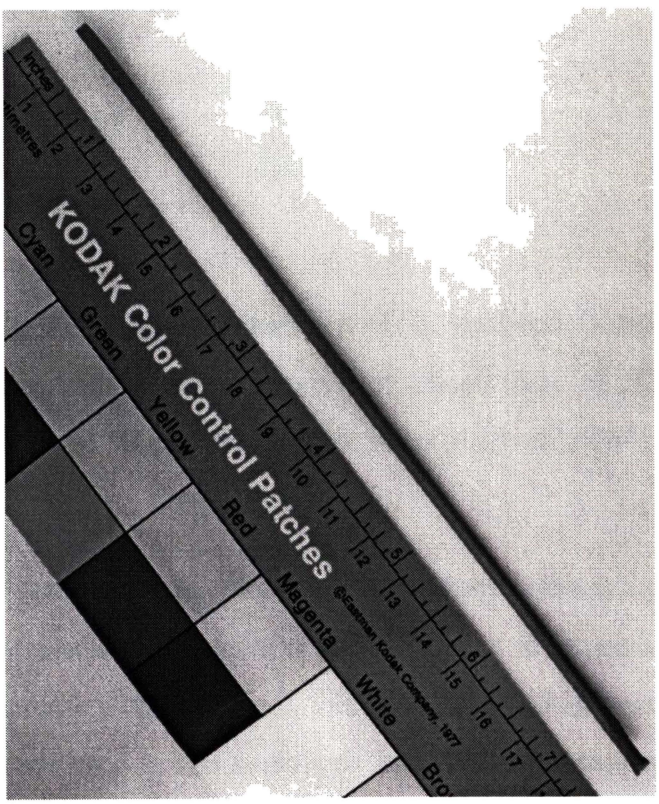


Fig. 5.3. Photograph of the CGO electrolyte (sample 4) sintered at 1600°C/2 h.

## 5.4.2 Electrochemical properties

Preliminary studies were undertaken on sample 4, to examine its electrochemical properties as an electrolyte (Fig. 5.4). A good open circuit voltage was achieved for the sample 5 cell of 0.911 V, indicating the electrolyte to be highly dense. The current voltage curve shows a current of 12.3 mA $cm^{-2}$ was achieved at 0.7 V (power density of 9 mW $cm^{-2}$) for the cell with a electrolyte thickness of 400 μm.

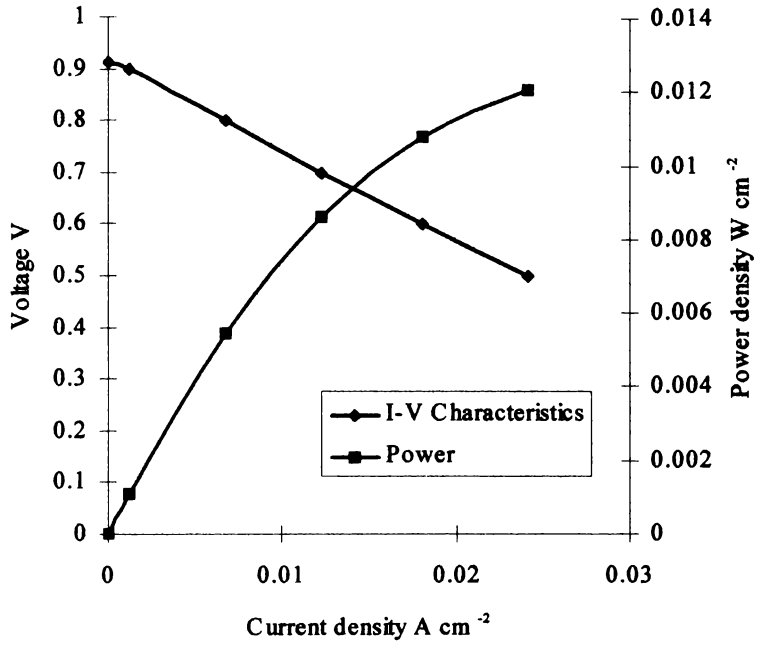


Fig. 5.4. I-V characteristics of the fuel cell (sample 4) with 12 cm long cathode, measured in air at a constant temperature of 600°C and constant flow rate of saturated $H_2$ bubbled through water at 25 $cm^3$ $min^{-1}$.

In comparison to other literature values (*1*) this is a poor result but in consideration of the electrolyte thickness of 400 μm it is expected the overall current density to increase with a decrease in the electrolyte thickness. It should also be noted that the anode used in this study was the same as those used in traditional high-temperature (950-1000°C) SOFC systems, and had not been optimised for use at 600°C, or with the CGO electrolyte. Additionally, the cathode electrode used in this study (used in

low temperature systems) was also not optimised. Further work is currently underway to examine alternative electrodes that would be more suitable for this system, and also to examine the long-term stability of the single cell.

## 5.5 Conclusions

By the manipulation of ceramic powder morphology and variation of the amounts of organic additives, CGO was extruded and then fired to form highly dense gas tight tubular electrolytes. This work illustrated the necessity of obtaining the correct particle size/specific surface area of the ceramic powder to achieve dense ceramic tubes by way of extrusion. The structural integrity of the extruded green tubes was improved by modifying the wt.% and ratio of organics, and altering the powder particle size and morphology. The extrusion pressure was lowered by introduction of a lower Tg binder with greater plasticity. I-V characteristics were obtained for the cell, a good OCV was achieved for the cell of 0.911 V with, however, poor operating current density of 12.3 mA $cm^{-2}$ at 0.7 V and power of only 9 mW $cm^{-2}$.

## 5.6 References

1. K. Zheng, B. C. H. Steele, M. Sahibzada, and I. S. Metcalfe, *Solid State Ionics* **86-8**, 1241 (1996).
2. N. Q. Minh, *J. Amer. Ceram. Soc.* **76**, 563 (1993).
3. P. Kofstad and R. Bredesen, *Solid State Ionics* **52**, 69 (1992).
4. H. Inaba and H. Tagawa, *Solid State Ionics* **83**, 1 (1996).
5. S. Desouza, S. J. Visco, and L. C. Dejonghe, *J. Electrochem. Soc.* **144**, L35 (1997).
6. D. L. Maricle, T. E. Swarr, and S. Karavolis, *Solid State Ionics* **52**, 173 (1992).
7. "The Westinghouse Solid Oxide Fuel Cell Program - A 1992 Progress Report," Westinghouse Electric Corporation, Pittsburgh, 1992.
8. K. Kendall and M. Prica, *in* "Proceedings of the First European Solid Oxide Fuel Cell Forum" (U. Bossel, ed.), Vol. 1, p. 163, Lucerne, Switzerland, 1994.
9. I. P. Kilbride, *J. Power Sources* **61**, 167 (1996).
10. C. E. Hatchwell, N. M. Sammes, and K. Kendall, *J. Power Sources* **70**, 85 (1998).
11. M. A. Janney, *in* "The American Ceramic Society 96th Annual Meeting & Exposition, Short Course, Ceramic Forming Processes", Indiana Convention Center Indianapolis, Indiana, 1994.
12. A. Roosen, *in* "Ceramic Transactions, Ceramic Powder Science II" (G. L. Messing, E. R. Fuller, and H. Hausner, eds.), Vol. 1, p. 675, 1988.

# Chapter Six

## *Current-Collectors for a Novel Tubular Solid Oxide Fuel Cell Design*

Published in: *J. Power Sources* **77**, 64 (1999).

# *Introductory note*

Leading on from studies performed in Chapter Four and Five, the following Chapter describes investigations into current collection for both YSZ and $Ce_{0.8}Gd_{0.2}O_{1.9}$ electrolyte based cells; using a novel combination of plate current collect design and tubular SOFC.

The plates were based on grooved Ducrolloy ($Cr5Fe1Y_2O_3$) metal plates used in the planar design similar in design to Fig. 2.10(a), and the cathode "bus" plate current collectors of the tubular design (see Fig. 2.11). Various perovskite and silver cermet coatings were applied to the $Cr5Fe1Y_2O_3$ in order to improve electrical contact between the cathode and the metal plate. Silver cermet coatings were utilised as it was considered they would improve electrical contact. Similar cermet coatings have been shown to have lower resistances than the perovskite alone and are stable at reduced operation temperature (750°C) (*1*).

The purposes of this new method were to:

- investigate an alternative design of current collection to the metal alloy wires and silver strip discussed in Chapter Four;
- investigate alternative conductive coatings to the $LaCoO_3$ detailed in Chapter Four (incorporate silver based cermet into the current collect design of a reduced temperature ($Ce_{0.8}Gd_{0.2}O_{1.9}$ electrolyte) SOFC);
- attain cell performances equal to those achieved using the silver wire current collectors,
- maintain the excellent high thermal shock resistant and rapid start up properties of the small diameter SOFCs;

For the medium temperature $Ce_{0.8}Gd_{0.2}O_{1.9}$ based electrolyte SOFC (developed in Chapter Five), Ag-$La_{0.8}Sr_{0.2}CrO_3$ and Ag-$La_{0.6}Sr_{0.4}CoO_3$ were used as coatings on the $Cr5Fe1Y_2O_3$.

$La_{0.6}Sr_{0.4}CoO_3$ was used in the silver cermet instead of $LaCoO_3$ ($LaCoO_3$ was used in Chapter Four to coat the metal wires) because it exhibits superior conductivity (*2*), and it has been used as a cathode material for $CeO_2$-based electrolytes (*3, 4*). Additionally, as described by Kofstad et al. (*5*), silver-ceramic composites (cermets) may be incorporated into the interconnect design if operational temperatures can be reduced below 800°C. Due to $La_{0.8}Sr_{0.2}CrO_3$ being one of the most commonly used and studied interconnect materials, it was incorporated into the alternative Ag-$La_{0.8}Sr_{0.2}CrO_3$ cermet coating.

For the high temperature YSZ cells, $La_{0.8}Sr_{0.2}CrO_3$ and Ag-$La_{0.8}Sr_{0.2}CrO_3$ coatings were applied to Cr5Fe1$Y_2O_3$. $La_{0.8}Sr_{0.2}CrO_3$ was used because it was successfully employed by Brückner et al. (*6*) as a protective/conductive coating on Cr5Fe1$Y_2O_3$ alloy in high temperature SOFCs. In addition, the stability of $La_{0.8}Sr_{0.2}CrO_3$ with the YSZ electrolyte has also been proven (*7*).

The feasibility of Ag-$La_{0.8}Sr_{0.2}CrO_3$ coating was assessed at high temperature. It was envisaged, however, that the Ag-$La_{0.8}Sr_{0.2}CrO_3$ coating could be used in conjunction with reduced temperature-operation YSZ electrolytes, as high temperature operation would lead to high rates of silver evaporation from the cermet. The feasibility of both coatings had to be tested using the high temperature YSZ cells because no medium temperature YSZ electrolytes were fabricated in this thesis. Cobalt-based perovskite coatings such as $LaCoO_3$ used previously to coat the metal alloy wires described in Chapter Four were not utilised here. This was because $LaCoO_3$ is considered to be more reactive with the YSZ electrolyte at higher operating temperatures than (La,Sr)$CrO_3$ (*8*).

The final Chapter examines the compatibility of certain interconnect/current collect materials studied in Chapter Six, with the medium temperature $Ce_{0.8}Gd_{0.2}O_{1.9}$ electrolyte.

Published in: *J. Power Sources* **77**, 64 (1999).

# Current-Collectors for a Novel Tubular SOFC Design

C. Hatchwell and N. M. Sammes

Department of Technology, The University of Waikato, Private Bag 3105, Hamilton, New Zealand

I. W. M. Brown

Industrial Research Limited, PO Box 31-310, Lower Hutt, New Zealand

K. Kendall

The Birchall Centre for Materials Science, Keele University, Keele, Staffordshire ST5 5BG, UK

## 6.1 Abstract

Current collection/interconnection of novel tubular solid oxide fuel cells (SOFCs) was achieved using alloy metal interconnects based on Ducrolloy ($Cr5Fe1Y_2O_3$) coated with various electronically conductive coatings. Coatings applied to the metal interconnect were shown to improve cell performance. For example, at 900°C in air, a Ag-$La_{0.8}Sr_{0.2}CrO_3$ (Ag-LSC) coated interconnect was used in conjunction with an 8 mol% yttria stabilised zirconia (YSZ) tubular electrolyte based SOFC. At 0.7 V a cell performance of 40 mA $cm^{-2}$ was achieved for the coated sample, compared to the lower performance of 16 mA $cm^{-2}$ attained for the uncoated interconnect. The thermal shock resistant properties of the tubes were shown not to be compromised by use of the metal interconnect.

Keywords: Solid oxide fuel cell; current collection

## 6.2 Introduction

SOFCs are highly energy efficient devices used to generate electricity from a variety of fuels. SOFCs may be fabricated in a variety of designs, including planar, tubular, segmented in-series and monolithic. To obtain higher power out-puts SOFCs are connected electrically in series or parallel using an electronically conducting interconnect (*9*). The literature shows there to be many forms of the interconnect/current collector depending on cell design, which vary from metal wires connected with metal gas separator plates (*10, 11*), Ni felts used in combination with metal plates (*12*), Ni/Cr wires (*13*), doped $LaCrO_3$ (*14*) and chromia forming metal plates (*15*). Of these, doped $LaCrO_3$ and chromia forming alloys (or a combination) are the most widely employed (*14*). The design and material components of the interconnect are highly dependent on its application with respect to the type of SOFC. For example, interconnects have been designed with reduced thermal stresses that overcome problems associated with thermal cycling, mismatches in thermal expansion coefficient (TEC) and improved electrical contact. Yamazaki et. al. (*16*), have reduced the thermal stress (where thermal stresses arise from differences in thermal expansion between the metal and ceramic components) in the planar SOFC stacks by implementation of a sliding mechanism between the separator and electrolyte, and by introduction of flexible wire interconnectors between the electrodes and the separators. Flexible wires have also been used in conjunction with tubular cells, which are detailed in a previous paper by the author (*17*). For the planar SOFC, Brückner et al. (*18*) coated a metal interconnect with a conductive perovskite coating to improve electrical contact; the metal alloy plate used was Ducrolloy ($Cr5Fe1Y_2O_3$), a metal designed for interconnect applications to have a conductive oxide coating and a TEC closely matching other cell components. As described by Brückner et al. (*18*), electrical contact between interconnect and cathode is reduced due to the unevenness of their surfaces. Application of a cathode coating on the interconnect can increase the electrical contact between the cathode and interconnect, by compensating for the corrugations present on their respective surfaces. Under operational temperature and slight mechanical pressure, the coating can adjust to the uneven surfaces, enlarging the electrical contact area considerably. Coatings can also

be used to reduce the chromium evaporation from the metal interconnect to the cathode, which is detrimental to cell performance. Therefore, tailoring the coating to have better electronic conductivity and/or reduce chromium evaporation would be a plausible way to improve cell performance. The use of Ag cermets as cathodes in SOFCs has been shown to improve the cell performance by lowering the resistivity of the electrode and increasing the contact area between the electrode and electrolyte (*1*). Using a similar philosophy, Ag cermets could be fabricated and applied as a coating to the surface of the metal alloy interconnect, reducing the resistance between the interconnect and cathode. In utilising the highly shock resistant properties of the tubular SOFCs with a metal interconnect of similar TEC and highly conductive coatings, it was envisaged that a thermally shock resistant method of interconnection could be achieved.

In this study, tubular cells were combined in a novel way with the planar type Cr5Fe1$Y_2O_3$ metal alloy interconnect. Various conductive perovskite and Ag cermet coatings were applied to the Cr5Fe1$Y_2O_3$ metal plate and are studied and compared as potential cathode current-collector/interconnector systems for both medium (600-850°C) and high temperature (900-1000°C) based tubular electrolyte SOFCs.

## 6.3 Experimental

### 6.3.1 The Tubular SOFCs

The tubular solid oxide fuel cells (SOFC) used in this study consisted of extruded electrolyte tubes, either YSZ or $Ce_{0.8}Gd_{0.2}O_{1.9}$ (CGO), with the cathodes (air electrodes) on the outside of the tubes and anodes (fuel electrodes) on the inside. Current collection for the cathode was achieved using Ag wire or perovskite/cermet coated metal alloy plates, while current collection for the anode was performed using Ni wires forced down the inside of the tube; details of the cathodes, anodes and current collectors used in conjunction with the YSZ and CGO electrolytes are given

in Table 6.1. Fig. 6.1 shows the proposed novel highly thermal shock resistant stacking combination of tubular cells with interconnector/current collector plates.

Table 6.1. Cathode current collectors, cathode layers, anodes and anode current collectors used in conjunction with 8 mol% $Y_2O_3$ stabilised $ZrO_2$ (YSZ) and $Ce_{0.8}Gd_{0.2}O_{1.9}$ (CGO) cells.

| | YSZ tubular cell | CGO tubular cell |
|---|---|---|
| Cathode current collectors | Ag wire<br>Ag-<br>$La_{0.8}Sr_{0.2}CrO_3$/Cr5Fe1$Y_2O_3$<br>$La_{0.8}Sr_{0.2}CrO_3$/Cr5Fe1$Y_2O_3$<br>Cr5Fe1$Y_2O_3$ | Ag wire<br>Ag-$La_{0.8}Sr_{0.2}CrO_3$/Cr5Fe1$Y_2O_3$<br>Ag-<br>$La_{0.6}Sr_{0.4}CoO_3$/Cr5Fe1$Y_2O_3$<br>Cr5Fe1$Y_2O_3$ |
| Layer 1 cathode | $La_{0.82}Sr_{0.18}MnO_3$ | $La_{0.6}Sr_{0.4}CoO_3$ |
| Layer 2 cathode | $La_{0.82}Sr_{0.18}MnO_3$2:1YSZ | $La_{0.6}Sr_{0.4}CoO_3$3:1CGO |
| Layer 3 cathode | - | $La_{0.6}Sr_{0.4}CoO_3$2:1CGO |
| Electrolyte | YSZ | $Ce_{0.8}Gd_{0.2}O_{1.9}$ |
| Anode | Ni-YSZ | Ni-YSZ |
| Anode current collect | Ni wire | Ni wire |

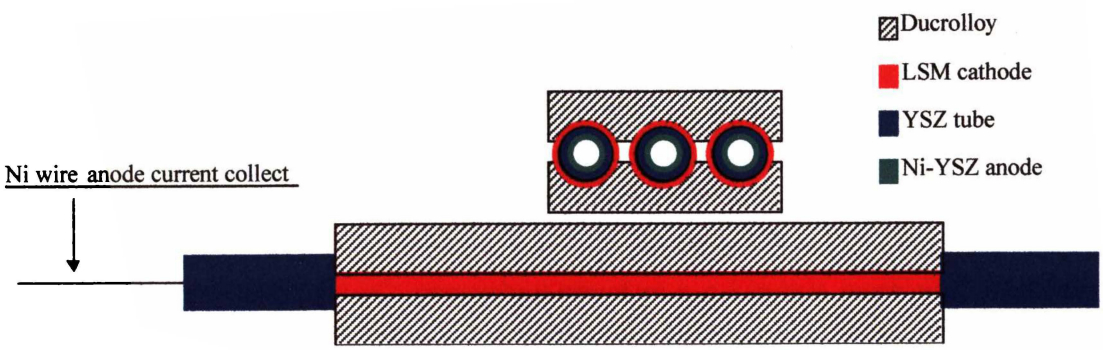


Fig. 6.1. Illustration of the novel small diameter SOFC tubes combined with Ducrolloy metal plate current collectors/interconnectors (Cr5Fe1$Y_2O_3$).

## 6.3.2 Fabrication of the electrolyte tubes

The YSZ electrolyte consisted of an extruded YSZ tube, sintered at 1450°C for 1 h, with an outside diameter of approximately 2.4 mm and thickness of 150 μm (extrudate supplied by Viking; extrusion and sintering performed by SAPCO). The CGO electrolyte was fabricated by extruding CGO extrudate through an in-house designed high strength steel piston extruder to form a tube. The extrudate was made by combining $Ce_{0.8}Gd_{0.2}O_{1.9}$ (CGO) (NexTech Materials, Ltd. Worthington, OH), heat-treated at 900°C for 4 h, with commercial binders specific to extrusion (Rohm and Haas - Formulation Chemicals); details of the chemicals used are given in Table 6.2. The resulting green body tube was dried in air, then sintered at 1600°C for 2 h. Full details of extrudate preparation, extrusion and firing can be found elsewhere (*19*). The final sintered tube had an outside diameter and wall thickness of approximately 3.14 mm and 400 μm respectively.

Table 6.2. Weight percentages (wt.%) of organic additives relative to the weight of the ceramic CGO powder.

| PEG 1:10 $H_2O$ (wt.%) | AMP-95™ (wt.%) | Binder 1 (wt.%) | Binder 2 (wt.%) | $H_2O$ (wt.%) |
|---|---|---|---|---|
| 6.9 | 1.8 | 8.2 | 4.9 | 12.1 |

PEG is poly (ethylene glycol)-400 (Union Carbide Co., Danbury, CT), $H_2O$is de-ionised water, AMP-95™ is a pH control agent (Angus Chemical, Buffalo Grove, IL), Binder 1 is B1-1051 Duramax™, and Binder 2 is B1-1052 Duramax™.

## 6.3.3 Perovskite powder preparation

$La_{0.6}Sr_{0.4}CoO_3$ and $La_{0.8}Sr_{0.2}CrO_3$ perovskite powders used in this work were prepared using the glycine nitrate process (*20*). Stoichiometric mixtures of aqueous nitrate solutions containing $La(NO_3)_3.6H_2O$, $Sr(NO_3)_2$ and $Cr(NO_3)_3.9H_2O$ or $Co(NO_3)_2.6H_2O$ (Rectapur, Univar and Acros respectively, ≥ 99.9% purity) with glycine, were heated

in a beaker until ignition. The resulting powders were calcined in air at 900°C for 12 h.

### 6.3.4 Cathode fabrication

The cathode for the YSZ cell consisted of 2 layers; a contacting electrochemical layer in contact with the YSZ tube and a thicker cathode layer over the contacting layer. The contacting electrochemical layer, a 2:1 ratio of $La_{0.82}Sr_{0.18}MnO_3$ (LSM) commercial powder (Merck, LSM82X96010-2) to YSZ (TOSOH 8YSZ, 99.9% pure) ink, was painted onto the YSZ tube using a brush, and then dried in an oven at 140°C for 0.5 h. The LSM second layer was then applied by brush over the first layer and again dried in an oven. The cathode for the CGO electrolyte was fabricated in a similar fashion, however, the cathode consisted of 3 layers; a contacting layer of 2:1 ratio of $La_{0.6}Sr_{0.4}CoO_3$ to CGO, an intermediate layer of 3:1 ratio of $La_{0.6}Sr_{0.4}CoO_3$ to CGO and a third layer applied over the first 2 layers consisting of $La_{0.6}Sr_{0.4}CoO_3$. Each layer was dried and fired (1300°C for 1 h) before the next layer was applied. Before the inks were prepared, the ceramic powders were placed in 250 ml Nalgene bottles with ethanol and zirconia milling media and milled for 24 h. The mixture was then poured into evaporating dishes and the solvent removed by placing the dishes in an oven. To prepare the inks, the powders were mixed using a glass stirring rod with decal medium (Johnson Matthey Colour Pty. Ltd. ref. no. 7340/s) and mineral spirits (Aldrich); the mineral spirits were used to modify the viscosity of the inks. The outermost cathode layer consisted of 20 g ceramic powder mixed with 7.3 g decal medium and 1.5 g of mineral spirits. The intermediate and contacting layers consisted of 20 g powder mixed with 20 g of decal medium and 5.6 g of mineral spirits.

### 6.3.5 Anode fabrication

The anode was deposited onto the entire inside length of the tubular cells by draining anode ink through the cell. Preparation of the anode ink involved various steps. 5 g of 8 mol% YSZ (TOSOH 8YSZ, 99.9% pure) was calcined in a furnace (Carbolite RHF 17/3) and heated at 10 K $min^{-1}$ to 1500°C, holding for 10 min, and then cooled down to room temperature. The calcined YSZ was then sieved through a 180 μm sieve. 10.5 g of NiO (Alfa Chemicals), 2.9 g 1,1,1-trichloroethene, 2.1 g of methanol, 0.1 g di-butyl phthalate (Aldrich 99%) and 0.1 g of KD1 dispersant (Zeneca) was added, with zirconia milling media, to a plastic container, and milled for 2 h. The calcined YSZ was then added to the container and milled for a further 1 h. On completion of the milling, 0.1 g of PVB (polyvinyl butyral, Aldrich Chemical Company, Inc.) was added to the mixture and milled for a final 2 min. The anode ink was used immediately. A PVC tube was used to connect a syringe to the ceramic tubular electrolyte, ink was then poured into the syringe and allowed to drain through the cell. The cell was initially left to drain and then placed in an oven at 140°C to dry. A second coating was applied in a similar fashion. A total anode coating of approximately 30 μm was achieved. After application of electrodes, the cells were fired using a ramp rate of 1 K $min^{-1}$ to 500°C, 5 K $min^{-1}$ to 1300°C, 1300°C (dwell 1 h), and then 10 K $min^{-1}$ to room temperature.

### 6.3.6 Fabrication of cathode and anode current collectors

After firing the electrodes onto the YSZ tube, the current collectors were added. For relative comparison of cell current-voltage (I-V) curves with different methods of current collection, a single YSZ cell was used. Similarly, a single CGO cell was used to test the effect different current collection methods had on the CGO cell performance. The cathode current collector systems used in this work were Ag wires wound around the cathodes and coated (perovskite and cermet coated) and uncoated Cr5Fe1$Y_2O_3$. The Ag wires were wound around the cathodes, and were used as a standard to compare the effect the alternative Cr5Fe1$Y_2O_3$ metal plate based current

collector/interconnect systems had on fuel cell performance. As has already been described, Fig. 6.1 shows the proposed tubular cell and flat plate current collect system; the system employed in this work, however, used either a single YSZ or CGO cell wedged between the current collect plates. Before the Cr5Fe1$Y_2O_3$ was used as a current collector, the various perovskite and cermet coatings were applied. Inks were prepared in a similar manner as those used for the $La_{0.6}Sr_{0.4}CoO_3$ contacting layers described previously. In order to collect current from the metal plates, Ag wires were wound around the metal plates and attached to the Cr5Fe1$Y_2O_3$ using Ag paste. This was then dried in an oven for 15 min at 140°C and then fired in-situ up to the operating temperature of the cells during cell tests.

Anode current collection was achieved using two 0.5 mm Ni wires (99.98%, Advent Research Materials Ltd.) placed down the inside of the tubes, such that two Ni wires remained in contact with the anode by mechanical force exerted by the wires on the inside of the tubes.

### 6.3.7 SOFC testing

A purpose-built furnace was used for cell tests. A gas line connected to a dual supply of $H_2$ and $N_2$ was then attached to the end of the cell, while the current collecting wires for the electrodes were brought outside the furnace. Before testing, the cells were heated in the furnace to their respective operating temperatures, 900°C for the YSZ electrolyte and 600°C for the CGO electrolyte, while $N_2$ was passed through the tube. Upon reaching operating temperature, the $N_2$ supply was slowly turned off as $H_2$ was introduced. Anode reduction was achieved by passing pure $H_2$, at a rate of 25 $cm^3$ $min^{-1}$, bubbled through water at 25°C, through the cell for 15 min. The I-V characteristics of the cells were then measured using a potentiostat (PGP201 Potentiostat/Galvanostat, Radio Copenhagen) in air at the operating temperatures of the cells, and constant flow rate of 25 $cm^3$ $min^{-1}$ $H_2$.

## 6.4 Results and discussion

As previously described (*18*), the electrical contact area between the metallic interconnect and cathode can be greatly increased by coating the interconnect with a perovskite, thus improving cell performance. The results given in Fig. 6.2, clearly show this behaviour. When the YSZ cell was used in conjunction with the coated Cr5Fe1$Y_2O_3$, current densities achieved were far higher than when using the uncoated Cr5Fe1$Y_2O_3$. The use of a Ag-$La_{0.8}Sr_{0.2}CrO_3$ coating yielded a cell performance that almost equalled the standard Ag wire current collect. The I-V characteristics of the $La_{0.8}Sr_{0.2}CrO_3$ coating shown in Fig. 6.2, although less than that achieved using the Ag-$La_{0.8}Sr_{0.2}CrO_3$, showed an overall gain in cell performance over the uncoated interconnect. Furthermore, the performance of the $La_{0.8}Sr_{0.2}CrO_3$ coated interconnect was not overly inferior to the Ag wire interconnect, showing this to be an appropriate method of interconnection. The difference in performance between the two coatings was attributed mainly to the lower resistivity of the Ag-$La_{0.8}Sr_{0.2}CrO_3$ cermet compared with the $La_{0.8}Sr_{0.2}CrO_3$ ceramic. Both coatings weakly adhered to the surface of the interconnect, but could easily be wiped off using a paper towel. The high thermal shock resistant properties of the tubular design were not compromised, as the assembly could be brought up to temperature within minutes, even though the tubular cell was wedged between the two interconnect plates. This design allows for rapid start-up when compared to other tubular and planar cell designs that can take hours to reach operating temperature (*17*).

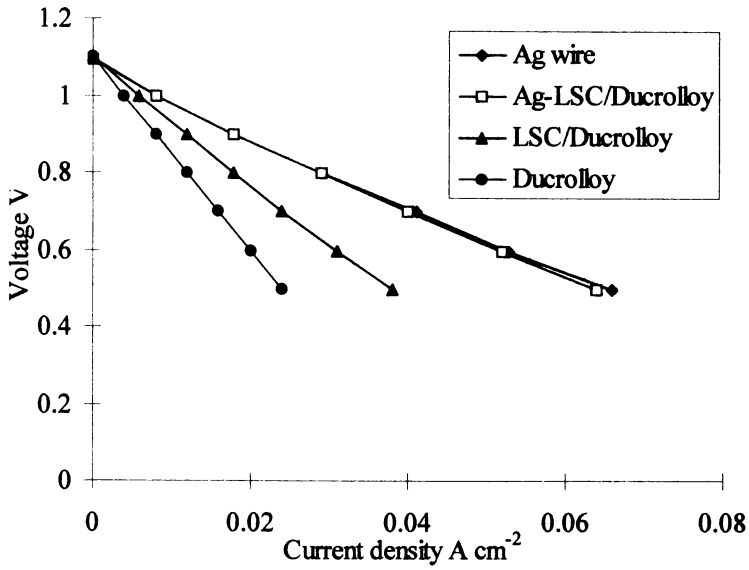


Fig. 6.2. I-V characteristics of YSZ electrolyte cells using different methods of cathode current collection; where Ag-LSC is Ag-$La_{0.8}Sr_{0.2}CrO_3$, and Ducrolloy is Cr5Fe1$Y_2O_3$. The cell was tested at 900°C using a constant flow rate of saturated $H_2$ bubbled through water at 25 $cm^3$ $min^{-1}$.

Fig. 6.3 describes the results obtained for the CGO-based SOFC system at 600°C. The I-V characteristics in Fig. 6.3 show Ag-$La_{0.8}Sr_{0.2}CrO_3$ coating to have yielded a better performance than the Ag-$La_{0.6}Sr_{0.4}CoO_3$ coating even though the ceramic component of the latter coating is reported to have a much higher conductivity of 1000 S $cm^{-1}$ (*21*) compared to 36.6 S $cm^{-1}$ for the $La_{0.8}Sr_{0.2}CrO_3$ component of Ag-$La_{0.8}Sr_{0.2}CrO_3$ (*22*). On removal of the Ag-$La_{0.6}Sr_{0.4}CoO_3$ coated interconnect from the cell, it was found that the coating had bonded together and de-laminated from the surface of the interconnect. We believe that this de-lamination induces a higher resistance, resulting in poorer cell performance. It was assumed that the thermal expansion coefficient difference between the coating and the interconnect was too large. For example, the TEC of $La_{0.6}Sr_{0.4}CoO_3$ and Ag have reported values of 18.8 (*23*) and 25.2 x $10^{-6}$ $K^{-1}$ (*5*) respectively, compared to 11.3 x $10^{-6}$ $K^{-1}$ for Cr5Fe1$Y_2O_3$ (*24*). To maintain a closer match of TEC between the coating and Cr5Fe1$Y_2O_3$, Ag-$La_{0.8}Sr_{0.2}CrO_3$ was used (TEC of $La_{0.84}Sr_{0.16}CrO_3$ is 9.6 x $10^{-6}$ $K^{-1}$); as

the Ag-$La_{0.8}Sr_{0.2}CrO_3$ coating was found to adhere to the surface of the interconnect when testing the YSZ electrolyte cell.

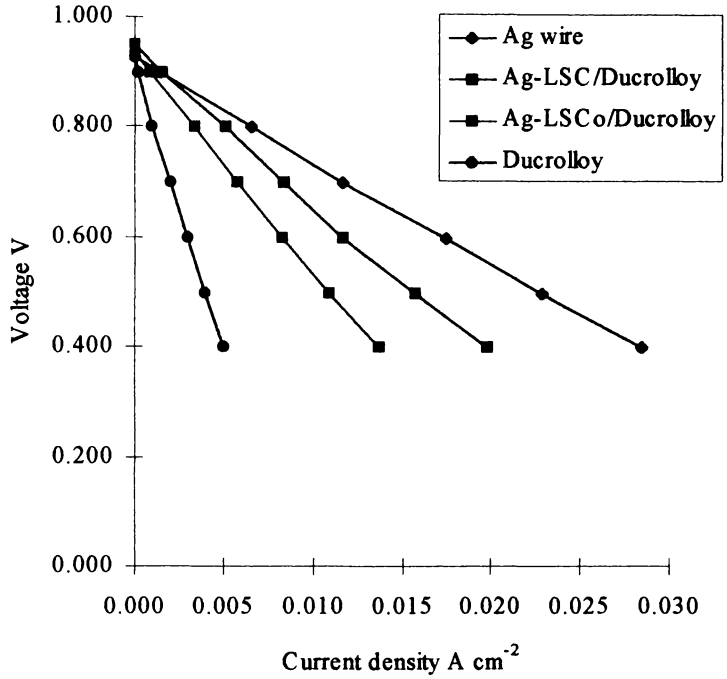


Fig. 6.3. I-V characteristics of CGO electrolyte cells using different methods of cathode current collection; where Ag-LSC is Ag-$La_{0.8}Sr_{0.2}CrO_3$, Ag-LSCo is Ag-$La_{0.6}Sr_{0.4}CoO_3$ and Ducrolloy is Cr5Fe1$Y_2O_3$. The cell was tested at 600°C using a constant flow rate of saturated $H_2$ bubbled through water at 25 $cm^3$ $min^{-1}$.

When Ag-$La_{0.8}Sr_{0.2}CrO_3$ coated Cr5Fe1$Y_2O_3$ and Ag wire current collectors were used alternately on the same YSZ cell, performances were approximately equal. However, when the same current collectors were used in a similar way on the CGO electrolyte cell, the performances achieved were lower for the Ag-$La_{0.8}Sr_{0.2}CrO_3$ coated Cr5Fe1$Y_2O_3$ than the Ag wire. The drop in performance relative to the Ag wire current collect is attributed to the use of a lower operating temperature of 600°C. The conductivity of $La_{0.8}Sr_{0.2}CrO_3$ is temperature dependent, and at lower temperatures is vastly reduced, increasing the resistivity of the coating (or increasing contact resistance between interconnect and cathode), thus reducing cell performance. At 900°C, on the YSZ electrolyte, $La_{0.8}Sr_{0.2}CrO_3$ would be expected to show a higher conductivity, thereby reducing the resistance between interconnect

and cathode. The change in temperature affects the conductivity of the coating, which in turn affects the performance of the cell; this is also illustrated in the work by Kimura et al. (*13*).

## 6.5 Conclusions

The coating of the metal interconnect (current collector) with a variety of perovskites and cermets was shown to improve cell performances. On comparison with the Ag wire current collect, the Ag-$La_{0.8}Sr_{0.2}CrO_3$ and alternate $La_{0.8}Sr_{0.2}CrO_3$ coated metal interconnects used in conjunction with the YSZ electrolyte cell (operating temperature of 900°C) yielded favourable performances. Similar results were demonstrated for the CGO electrolyte cell. However, a reduction in operating temperature, by use of the CGO electrolyte, resulted in a drop in cell performance. This reduction in cell performance was attributed to increased resistivity of the ceramic component of the coating at lower temperature. Furthermore, for the CGO cell, a high mismatch in TEC between the Ag-$La_{0.6}Sr_{0.4}CoO_3$ and the interconnect was shown to result in a reduced cell performance. It was also demonstrated that the high thermal shock resistant properties of the tubular cells wedged between the interconnects were not compromised. Future work will involve investigation of chemical bonding between the interconnect and cathode using various perovskite and cermet based materials; it is envisaged that improved bonding will allow better cell performance, although this may compromise the thermal shock resistant properties of the cell.

## 6.6 References


1. L. S. Wang and S. A. Barnett, *Solid State Ionics* **76**, 103 (1995).
2. A. N. Petrov, O. F. Kononchuk, A. V. Andreev, V. A. Cherepanov, and P. Kofstad, *Solid State Ionics* **80**, 189 (1995).
3. M. Gödickemeier, K. Sasaki, L. J. Gauckler, and I. Riess, *Solid State Ionics* **86-8**, 691 (1996).
4. W. Bakker, C. Milliken, J. Hartvigsen, S. Elangovan, and A. Khandkar, *in* "Solid Oxide Fuel Cells V" (U. Stimming, S. C. Singhal, H. Tagawa, and W. Lehner, eds.), Vol. PV 97-40, p. 254. The Electrochemical Society, Inc., Aachen, Germany, 1997.
5. P. Kofstad and R. Bredesen, *Solid State Ionics* **52**, 69 (1992).
6. B. Brückner, C. Günther, R. Ruckdäschel, E. Fendler, and H. Schmidt, *in* "Fuel Cell", p. 155, Orlando Florida, November 17-20, 1996.
7. M. Mori, H. Itoh, N. Mori, T. Abe, O. Yamamoto, Y. Takeda, and N. Imanishi, "Science and Technology of Zirconia V," p. 776. Technomic Publishing Co. Inc., NY., 1993.
8. O. Yamamoto, Y. Takeda, R. Kanno, and M. Noda, *Solid State Ionics* **22**, 241 (1987).
9. N. Q. Minh, *J. Amer. Ceram. Soc.* **76**, 563 (1993).
10. N. Tomita, T. Namikawa, and Y. Yamazaki, *Denki Kagaku* **62**, 638 (1994).
11. Y. Yamazaki, T. Namikawa, T. Ide, H. Kabumoto, N. Oishi, T. Motoki, and T. Yamazaki, *in* "Solid Oxide Fuel Cells V" (U. Stimming, S. C. Singhal, H. Tagawa, and W. Lehner, eds.), Vol. PV 97-40, p. 1291. The Electrochemical Society, Inc., Aachen, Germany, 1997.
12. K. Akagi, A. Siartori, M. Iha, and O. Chikagawa, *in* "Proceedings of the Fourth International Symposium on Solid Oxide Fuel Cells (SOFC-IV)" (M. Dokiya, O. Yamamoto, H. Tagawa, and S. C. Singhal, eds.), p. 129. The Electrochemical Society Inc., Yokohama, Japan, 1995.
13. T. Kimura, T. Namikawa, and Y. Yamazaki, *Denki Kagaku* **61**, 1115 (1993).
14. M. Dokiya, T. Horita, N. Saki, T. Kawada, H. Yokokawa, B. A. van Hassel, and C. S. Montross, *in* "14th Risø International Symposium on Material

Science" (F. W. Poulsen, J. J. Bentzen, T. Jacobsen, E. Skou, and M. J. L. Østergård, eds.), p. 33, 1993.

15. W. Quadakkers, H. Greiner, and W. Köck, *in* "First European Solid Oxide Fuel Cell Forum" (U. Bossel, ed.), Vol. 1, p. 525, Lucerne Switzerland, 1994.
16. Y. Yamazaki, T. Namikawa, N. Oishi, and T. Yamazaki, *in* "Proceedings of the Fourth International Symposium on Solid Oxide Fuel Cells (SOFC-IV)" (M. Dokiya, O. Yamamoto, H. Tagawa, and S. C. Singhal, eds.), p. 236. The Electrochemical Society Inc., Yokohama, Japan, 1995.
17. C. E. Hatchwell, N. M. Sammes, and I. W. M. Brown, submitted to *Solid State Ionics* (1998).
18. B. Brückner, H. Landes, and B. Rathjen, *in* "Proceedings of the Third International Symposium on Solid Oxide Fuel Cells" (S. C. Singhal and H. Iwahara, eds.), Vol. 93 - 94, p. 641, Honolulu, Hawaii, 1993.
19. C. Hatchwell, N. M. Sammes, and I. W. M. Brown, *Solid State Ionics* (1998).
20. L. A. Chick, L. R. Pederson, G. D. Maupin, J. L. Bates, and J. G. Exharhos, *Mater. Lett.* **10**, 1 (1990).
21. A. N. Petrov and P. Kofstad, *in* "Proceedings of the Third International Symposium on Solid Oxide Fuel Cells" (S. C. Singhal and H. Iwahara, eds.), Vol. 93 - 94, p. 220, Honolulu, Hawaii, 1993.
22. M. Mori, T. Yamamoto, H. Itoh, T. Abe, S. Yamamoto, Y. Takeda, and O. Yamamoto, *in* "First European Solid Oxide Fuel Cell Forum" (U. Bossel, ed.), Vol. 1, p. 465, Lucerne Switzerland, 1994.
23. K. Eguchi, T. Setoguchi, and H. Hiromichi, *in* "Energy Conversion and Utilisation with High Efficiency - Science and Technology for Energy Conversion", p. 93. 1990.
24. W. Köck, H. P. Martinz, H. Greiner, and M. Janousek, *in* "Proceedings of the Fourth International Symposium on Solid Oxide Fuel Cells (SOFC-IV)" (M. Dokiya, O. Yamamoto, H. Tagawa, and S. C. Singhal, eds.), p. 841. The Electrochemical Society Inc., Yokohama, Japan, 1995.

# Chapter Seven

## *Chemical Compatibility of Chromium-Based Interconnect Related Materials with Doped-Cerium Oxide Electrolyte*

Accepted for publication in: *J. Euro. Ceram. Soc.* (1999).

# *Introductory note*

This Chapter describes studies performed on the chemical compatibility of certain interconnect, and interconnect related materials with the $Ce_{0.8}Gd_{0.2}O_{1.9}$ medium temperature electrolyte.

In the previous Chapter, a chromia forming alloy ($Cr5Fe1Y_2O_3$) coated with $(La,Sr)CrO_3$ was used as a cathode current collector/interconnector for the $Ce_{0.8}Gd_{0.2}O_{1.9}$ electrolyte based SOFC. A literature survey showed no studies had been performed on the reactivity of these, or any other interconnect or interconnect related materials, with the $Ce_{0.8}Gd_{0.2}O_{1.9}$ electrolyte.

As described in Appendix C, an initial investigation was conducted on the reactivity of $CaCrO_4$ (a second phase related to $(La,Ca)CrO_3$) with $Ce_{0.8}Gd_{0.2}O_{1.9}$. This work highlighted the need to study the reactivity of interconnect materials and associated interconnect materials with $Ce_{0.8}Gd_{0.2}O_{1.9}$.

Accepted for publication in: *J. Euro. Ceram. Soc.* (1999).

# Chemical Compatibility of Chromium-Based Interconnect Related Materials with Doped-Cerium Oxide Electrolyte

C. E. Hatchwell, N. M. Sammes and G. A. Tompsett
Department of Technology, The University of Waikato, Private Bag 3105, Hamilton, New Zealand

I. W. M. Brown
Industrial Research Limited, PO Box 31-310, Lower Hutt, New Zealand

## 7.1 Abstract

X-ray diffraction and scanning electron microscopy were used to study the chemical compatibility of (La,Sr)$CrO_3$, $SrCrO_4$, $CaCrO_4$ and $Cr_2O_3$ (materials associated with the interconnect of a solid oxide fuel cell) with gadolinia-doped cerium oxide electrolyte (CGO). Powder mixtures and multilayer pellets of the interconnect related materials were annealed with CGO in air at temperatures ranging from 650°C to 1600°C for durations of up to 400 h. No reaction was observed between (La,Sr)$CrO_3$ and $Ce_{0.8}Gd_{0.2}O_{1.9}$ after annealing at 1600°C for 10 h. However, $SrCrO_4$, $CaCrO_4$ and $Cr_2O_3$ reacted with CGO, forming an unidentified phase.

Key Words: Cerium Oxide, Compatibility, X-ray diffraction, Electron Microscopy, SOFC.

## 7.2 Introduction

The single-cell solid oxide fuel cell (SOFC) consists of an anode and cathode (porous electrodes), separated by a solid electrolyte (typically yttria stabilised zirconia),

which conducts ions between the two electrodes. For practical applications, the single cells are connected in series to form a stack. This connection is achieved by utilisation of an interconnect which electrically interconnects the single cells such that repeat units of anode, electrolyte, cathode and interconnect are stacked on top of each other. These stacks can then be placed into series to increase the voltage, or in parallel to increase the total power output (*1*).

Alkaline earth-doped lanthanum chromites and chromia forming alloys (alloys that form a protective and conductive $Cr_2O_3$ coating) are commonly used as interconnects in SOFCs (*1*). The use of chromia forming alloys has led to reduced cell performance as chromium has been shown to evaporate from the surface of the metal interconnect into the cathode. This evaporation can be reduced by the surface treatment of the alloy separator (*2, 3*). In addition, the metal interconnect can be coated with a perovskite (typically doped $LaCrO_3$ or $LaCoO_3$), which has been shown to decrease contact resistance and improve the stability of cell performance over time (*3-6*).

To improve the sinterability and electrical conductivity of these protective/conductive coatings, dopants are added to the lanthanum chromites such as Sr and Ca (A-site) and Co (B-site) (*1*). $(La,Ca)CrO_3$, for example, can be sintered in air at 1300°C via the assistance of a transitory liquid phase that belongs to the $CaO$-$Cr_2O_3$ phase system. Under certain conditions, $CaCrO_4$ emanates as a secondary phase from $(La,Ca)CrO_3$. At 1022°C, this secondary phase melts incongruently to form a liquid and solid mixture. By addition of excess Ca into $(La,Ca)CrO_3$ improved sintering can be achieved as the addition of Ca enhances the sintering characteristics of the liquid phase (*7*). The improved sinterability of $LaCrO_3$, doped with Sr, was assumed to be due to a $SrCrO_4$ melt (*1*). The $SrCrO_4$ phase melts in air incongruently at 1251°C forming $Cr_2O_3$, liquid, and $O_2$ (*8*).

There have been a number of investigations that report on the reactivity of the SOFC components with each other (*7, 9, 10*). Few, however, report on the reaction of the interconnect with the electrolyte material. Mori et al. (*10*) have studied the reactions between alkaline earth doped lanthanum chromite and yttria stabilised zirconia. The authors found that $Sr_4Zr_3O_{10}$ formed when a mixture of 7.5 mol % yttria stabilised

zirconia (YSZ) was reacted with $La_{0.7}Sr_{0.3}CrO_3$ at 1500°C for 24 h, while $La_{1-x}Sr_xCrO_3$ (x = 0.1 and 0.2) showed no reaction product with YSZ at 1500°C for 168 h. Furthermore, all the elements of the perovskite diffused into the YSZ at 1500°C. Carter et al. (*7*) showed the difficulty of co-firing (La,Ca)$CrO_3$ with YSZ. The Ca migrates from (La,Ca)$CrO_3$, via a Ca-Cr-O liquid phase, to react with YSZ to form an intermediate layer of $CaZrO_3$, where-by the depth of the $CaZrO_3$ layer deposited was shown to increase with increasing Ca content in the exsolved Ca-Cr-O liquid phase.

(La,Sr)$CrO_3$ and (La,Ca)$CrO_3$ coated chromia-forming alloys may react with electrolytes such as gadolinia-doped ceria (CGO) during co-firing. For example, in a similar fashion to that of $CaCrO_4$ which was shown to react with YSZ (*7*), it is plausible that $SrCrO_4$, detected at the alloy interconnect/(La,Sr)$CrO_3$ interface (*3*), and $CaCrO_4$, present in Ca doped-lanthanum chromites, may react with CGO. Similarly, $Cr_2O_3$ formed on the surface of the chromia forming alloys may also react with CGO.

This study, therefore, focuses on the compatibility of (La,Sr)$CrO_3$, $SrCrO_4$, $CaCrO_4$ and $Cr_2O_3$ with CGO.

## 7.3 Experimental procedure

### 7.3.1 Sample preparation

$Ce_{0.8}Gd_{0.2}O_{1.9}$ was synthesised using $Ce(NO_3)_3.6H_2O$ and $Gd(NO_3)_3.6H_2O$ (Arcos and Aldrich respectively, ≥ 99.9% pure) by using the reverse strike co-precipitation method (*11*). A 0.5 M aqueous oxalic acid solution was prepared and the pH adjusted to between 6.7-6.9 using a dilute ammonia solution. $Ce(NO_3)_3.6H_2O$ and $Gd(NO_3)_3.6H_2O$ were dissolved in water and then added drop-wise to the oxalic acid solution. Ammonia was added at the same time to maintain a pH of between 5.0-6.0. The precipitate was filtered, and then washed using distilled water and ethanol respectively. After drying, the powder was calcined at 700°C for 1 h, pressed, then

sintered at 1600°C for a further 10 h. $La_{1-x}Sr_xCrO_3$ (where x = 0.0-0.4) was prepared by employing the glycine nitrate process (GNP) (*12*). Stoichiometric mixtures of aqueous nitrate solutions containing $La(NO_3)_3.6H_2O$, $Sr(NO_3)_2$ and $Cr(NO_3)_3.9H_2O$ (Rectapur, Univar and Acros respectively, ≥ 99.9% purity) with glycine, were heated in a beaker until ignition. The resulting powders were calcined in air at 900°C for 12 h, pressed then sintered at 1650°C for 10 h.

$SrCrO_4$ was synthesised by placing the appropriate stoichiometric quantities of $SrCO_3$ and $Cr_2O_3$ (BDH) into a Retsch centrifugal ball mill with ethanol and partially stabilised zirconia grinding media (PSZ), and milling for 24 h. The as-synthesised powders were then calcined at 800°C for 2 h.

Using the GNP, Ca and Cr nitrates with glycine were combusted to produce $CaCrO_4$, the resulting powder was then calcined in air at 800°C for 2 h.

### 7.3.2 Pressing

The ceramic powders were mixed in a pestle and mortar with 2 wt.% polyvinyl butyral (Aldrich). Enough acetone was then added to form a highly viscous mixture, which was then placed in an oven at 50°C until dry. The powder was ground, placed in a 15 mm diameter die, compacted with an uniaxial press using 30 MPa pressure, followed by pressing in an isostatic press at 200 MPa (Stansted Fluid Power Ltd. FPG2347). The binder was then burnt out by placing the samples in a furnace, ramped at 0.5 K $min^{-1}$ to 500°C, held for 1 h, then cooled at 10 K $min^{-1}$ to room temperature.

### 7.3.3 Powder mixtures

Powder mixtures, as detailed in Table 7.1, were prepared by mixing the powders together in a pestle and mortar then pressing them into pellet form. Powder mixtures of 1:1 molar ratios of $La_{1-x}Sr_xCrO_3$ (where x = 0.0, 0.1, 0.2, 0.3, 0.4) and CGO, or of

$Cr_2O_3$ and CGO were pressed into pellets. Similarly, CGO was mixed with either $SrCrO_4$ or $CaCrO_4$ in a 1:1.36 ratio. As described in the paper by Carter et al. (*7*), the amount of Ca for reaction with the YSZ electrolyte in $(La,Ca)CrO_3$ was restricted, therefore mixtures of $CaCrO_4$ and thus $SrCrO_4$ were reacted with CGO in the molar ratio of 1.36:1. $CaCrO_4$ was considered to be of a similar composition to the transient liquid phase in $(La,Ca)CrO_3$, therefore any reaction products associated with the $CaCrO_4$/CGO mixture could be related to those of the transient liquid phase. $SrCrO_4$ was considered in a similar context.

Table 7.1. Composition, molar ratio, reaction conditions and phase analysis of mixed powders (all powders were mixed with CGO in the ratios described).

Note: LSC = $La_{1-x}Sr_xCrO_3$, CGO = $Ce_{0.8}Gd_{0.2}O_{1.9}$, SCC = $Sr_{2.67}O_{0.33}(CrO_4)_{1.33}(CrO_4)_{0.67}$

| Composition | Molar ratio | Reaction conditions | Phase analysis |
|---|---|---|---|
| $La_{1-x}Sr_xCrO_3$ | 1:1 | 1300°C/400 h | LSC and CGO |
| (x = 0-0.4) | | 1420°C/10 h | LSC and CGO |
| | | 1600°C/10 h | LSC and CGO |
| $SrCrO_4$ | 1.36:1 | 750°C/67 h | $SrCrO_4$ and CGO |
| $SrCrO_4$ | 1.36:1 | 1300°C/24 h | $SrCrO_4$, SCC and CGO |
| $CaCrO_4$ | 1.36:1 | 1300°C/24 h | $CaCrO_4$, CGO, Ca-Ce-Gd-Cr-O |
| $Cr_2O_3$ | 1:1 | 650°C/400 h | $Cr_2O_3$ and CGO |
| | | 1300°C/400 h | $Cr_2O_3$ and CGO |
| | | 1400°C/10 h | $Cr_2O_3$ and CGO |
| | | 1600°C/10 h | $Cr_2O_3$, CGO, Cr-Gd-O |

All pellets were then annealed in air at various times and temperatures as described in Table 7.1. The pellets were then ground and analysed using x-ray powder diffraction (XRD) (Philips PW 1700 series automated powder diffractometer), equipped with a graphite monochromator. The characterisation was performed using Co-K$\alpha$ radiation of weighted mean wavelength $\lambda$ = 1.79026 Å with generator settings of 45 kV and 35 mA.

### 7.3.4 Reaction couples

To study the interfacial compatibility of CGO with the related interconnect materials, interfacial reaction couples, given in Table 7.2, were prepared in the following manner. $Cr_2O_3$ and CGO pellets were pressed separately and the binders burnt out as described above. The $Cr_2O_3$ pellet was then fired at 1200°C for 2 h while CGO was fired at 1600°C for 10 h. After firing, the pellets were then polished using a 1 μm diamond paste. The polished faces of $Cr_2O_3$ and CGO were then placed together with a 10 g weight on top inside a furnace. The reaction couple was then annealed for the various times and at the temperatures described in Table 7.2. The reaction couple of $La_{0.8}Sr_{0.2}CrO_3$ (pellet sintered at 1650°C), and CGO were prepared and reacted in a similar fashion.

In order to assess the interfacial reactivity of $SrCrO_4$ and $CaCrO_4$ with CGO, $SrCrO_4$ and $CaCrO_4$ pellets were placed onto the polished faces of CGO sintered plates. As detailed in Table 7.2, $SrCrO_4$/CGO reaction couples were then annealed at 1300°C for 24 h. Similarly, the $CaCrO_4$/CGO reaction couple was prepared in the same fashion and annealed in air at 1300°C for 24 h.

Table 7.2. Reaction of associated interconnect materials on CGO sintered plates.

| Compound | Reaction Conditions | Observations |
|---|---|---|
| $Cr_2O_3$ | 1300°C/400 h | No reaction |
| $La_{0.8}Sr_{0.2}CrO_3$ | 1300°C/400 h | No reaction |
| $SrCrO_4$ | 1300°C/24 h | Enveloped and melted through pellet |
| $CaCrO_4$ | 1300°C/24 h | Enveloped and melted through pellet |

All reaction couples were embedded in resin, sliced perpendicular to the interface and polished using 1 μm diamond paste. Scanning electron microscopy (SEM) (Cambridge Stereoscan MkII), equipped with energy dispersive x-ray analysis (Oxford-Link) was used to examine the lateral distribution of the elements across the reaction interface of the pellets.

## 7.4 Results and discussion

### 7.4.1 Powder mixtures

Powder mixtures were fired at various temperatures and times in order to identify any reaction products between CGO and related interconnect materials; Table 7.1 shows these results. No reaction was observed, between $La_{1-x}Sr_xCrO_3$ (X = 0.0-0.4) at 1300, 1420 or 1600°C. Similarly, as again described in Table 7.1, no reaction between $SrCrO_4$ and CGO was detected at 750°C for 67 h. However, as described in Fig. 7.1, $Sr_{2.67}O_{0.33}(CrO_4)_{1.33}(CrO_4)_{0.67}$ (SCC) (*8*) was shown to form in the powder mixture reacted at 1300°C for 24 h.

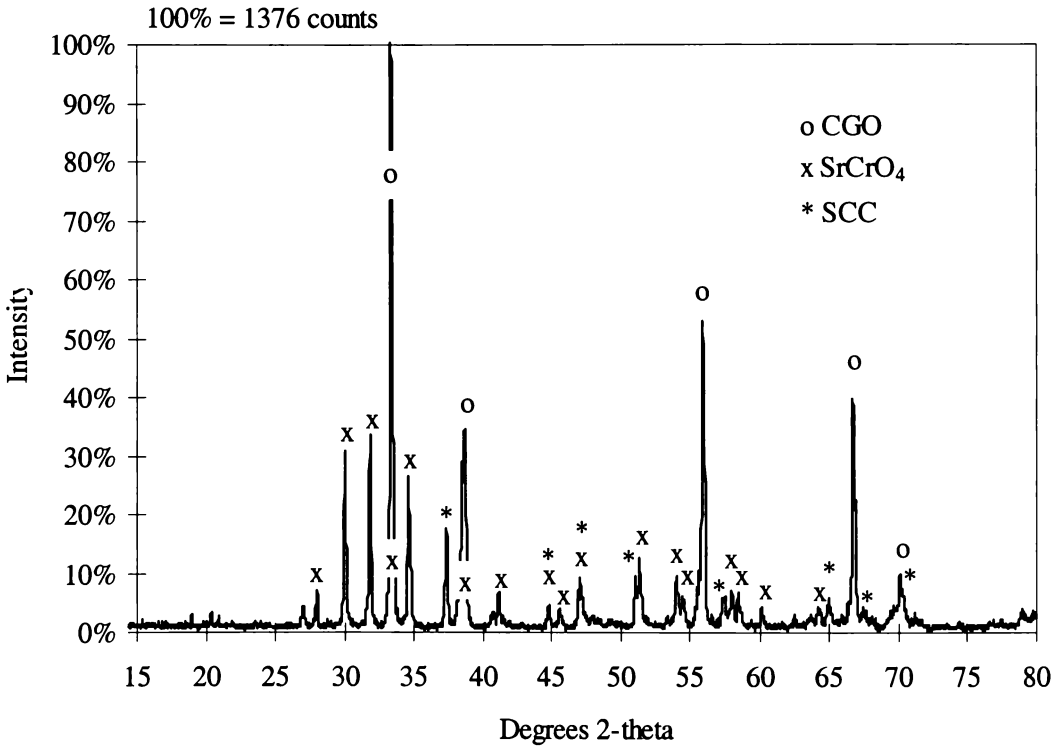


Fig. 7.1. XRD trace of a 1.36:1 molar ratio of $SrCrO_4$ and CGO powders fired at 1300°C over 24 h.

The $CaCrO_4$ 1.36:1 CGO molar ratio fired at 1300°C over 24 h revealed that an unidentified phase was formed; the XRD trace is shown in Fig. 7.2. This unidentified

phase was considered to be a perovskite, possibly orthorhombic in nature, as it was shown to closely match the ICDD powder diffraction file number of $InRhO_3$ (21-409) and also match, to a lesser extent, those of $LaCrO_3$ (33-701), $GdCrO_3$ (25-1056) and $CaCrO_3$ (21-137), although, as described later, this is somewhat inconclusive. Based on this evidence the cell dimensions were determined to be approximately, a = 5.3, b = 5.4, c = 7.6 Å.

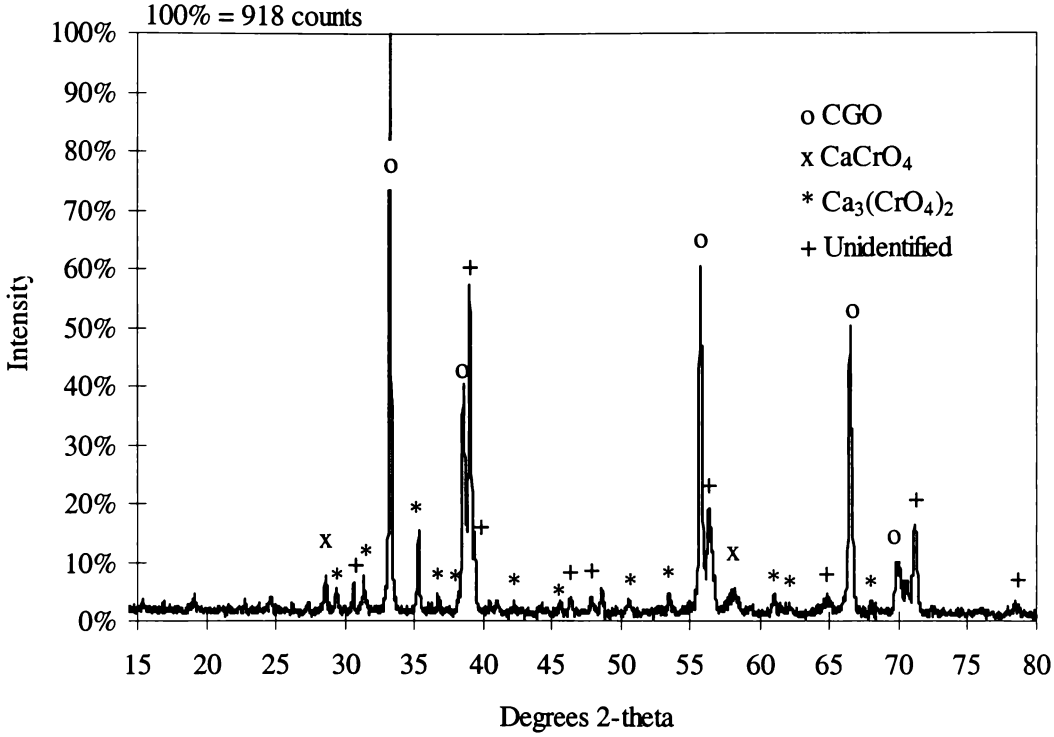


Fig. 7.2. XRD trace of a 1.36:1 molar ratio of $CaCrO_4$ and CGO powders fired at 1300°C over 24 h.

When the $Cr_2O_3$ 1:1 CGO molar ratio was fired over a range of temperatures, 650°C to 1600°C, the only reaction product detected was for the sample fired at 1600°C. The reaction product, as observed in Fig. 7.3, was thought to be $Ce_{1-x}Gd_xCrO_3$ perovskite, as the XRD peaks are similar to those in the ICDD powder diffraction data base for $LaCrO_3$ and $GdCrO_3$.

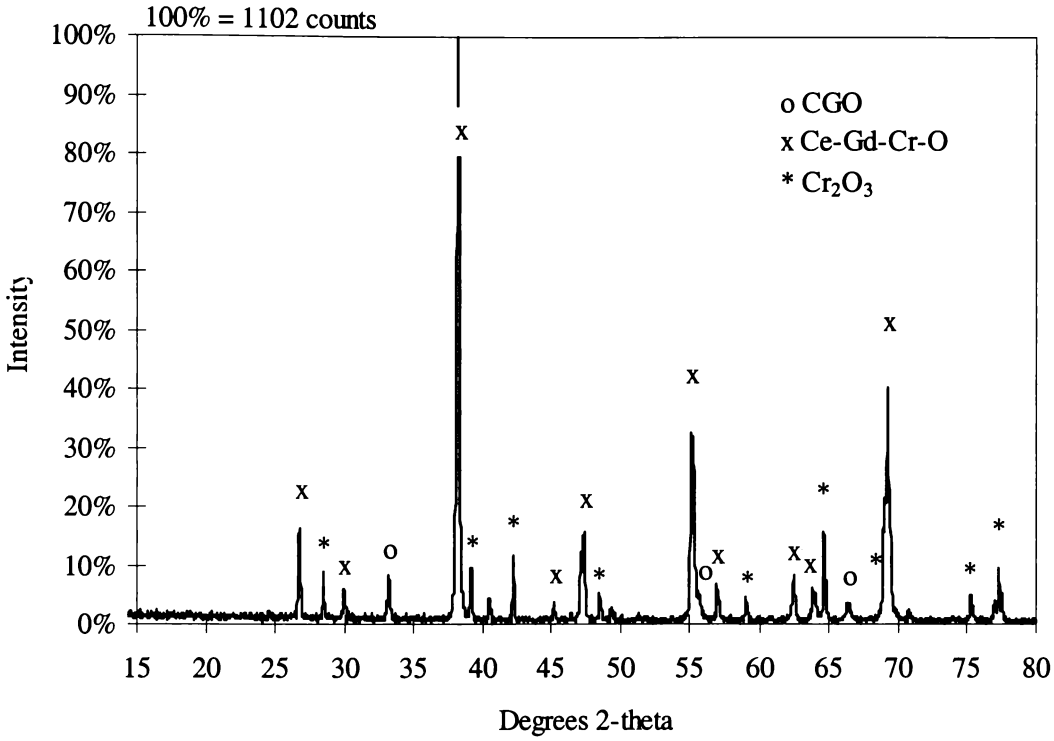


Fig. 7.3. XRD trace of a 1:1 molar ratio of $Cr_2O_3$ and CGO powders fired at 1600°C over 10 h.

## 7.4.2 Interfacial studies of $Cr_2O_3$ and $La_{0.8}Sr_{0.2}CrO_3$ on sintered CGO

The polished faces of the $Cr_2O_3$ and CGO pellets showed no visual signs of reaction after annealing at 1300°C for 400 h. EDX and SEM analysis were performed on the reaction faces and revealed no detectable migration of elements between the reaction couple. No reaction, as shown in Table 7.2, was detected for the $La_{0.8}Sr_{0.2}CrO_3$ and CGO reaction couple.

### 7.4.3 Interfacial studies of $SrCrO_4$ on sintered $Ce_{0.8}Gd_{0.2}O_{1.9}$

After annealing the $SrCrO_4$/CGO pellet couple in air at 1300°C for 24 h, visual examination showed the $SrCrO_4$ had partially melted and enveloped the entire surface of the CGO pellet. The $SrCrO_4$ pellet had changed colour from yellow to a dark black-green with inclusions of crystals. The couple was mounted in resin and polished. A dark green discolouration was observed where the $SrCrO_4$ had migrated into the CGO. SEM and EDX analysis were then performed to understand the nature of the interaction at the $SrCrO_4$/CGO interface.

A backscatter image, Fig. 7.4, shows the reaction regions; position A shows a grain at the interface, position B shows a banded region on the edge of the CGO saturated with pores, position C shows that there is no reaction within the bulk of the CGO, and position D shows dark contrasted grain boundaries in the CGO.

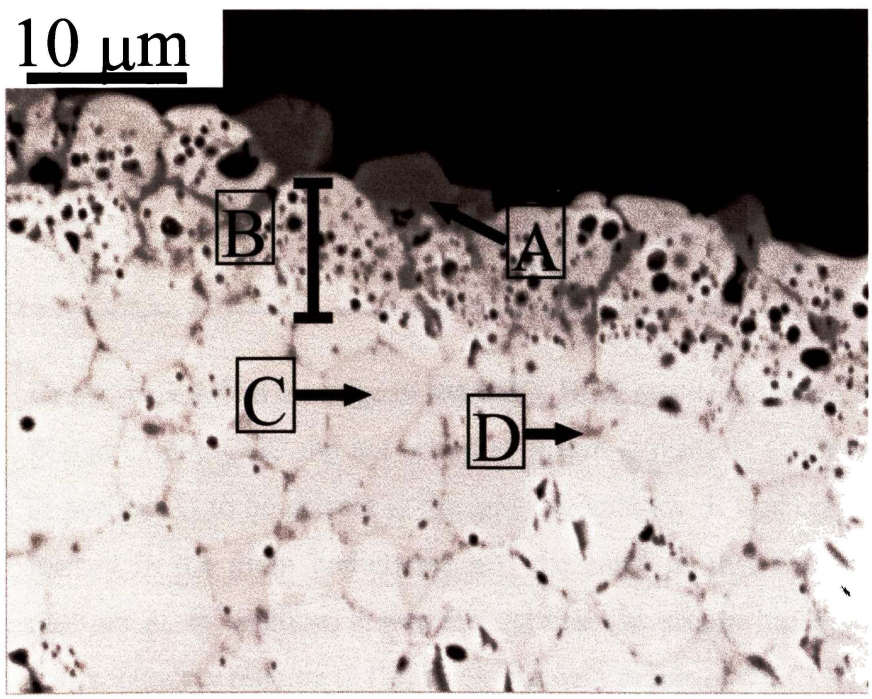


Fig. 7.4. SEM backscattered image of the $SrCrO_4$/CGO reaction couple interface annealed at 1300°C for 24 h.

As described in Table 7.3, using EDX point analysis at position A, a grain on the CGO/$SrCrO_4$ interface was shown to contain higher concentrations of Cr and Gd than Sr or Ce. As shown in the EDX map, Fig. 7.5, the grains present at the CGO/$SrCrO_4$ interface contain higher concentrations of Gd and Cr than Sr and Ce. In addition, EDX line analysis confirmed Gd had diffused, forming a larger component of the grain than Ce, leaving behind the Ce in higher concentrations in the banded region, Fig. 7.4 position B of the CGO. Position B, the reacted band on the CGO edge, was composed of a mixture of Sr and Cr at very low concentrations, and Ce and Gd in greater concentrations. Ce, relative to Gd, was seen to contain a proportionally higher concentration than in the bulk, position C, of the CGO sample due to the diffusion of the Gd into grains at the interface and grain boundaries D. The darker spots in the band were identified as pores.

Table 7.3. EDX point analysis of the $SrCrO_4$/CGO reaction couple interface annealed at 1300°C for 24 h.

| Element | Position A (Element wt.%) | Position B (Element wt.%) | Position C (Element wt.%) | Position D (Element wt.%) |
|---|---|---|---|---|
| Sr | 9 | 1 | - | 1 |
| Cr | 24 | 7 | - | 5 |
| Ce | 15 | 27 | 69 | 56 |
| Gd | 31 | 12 | 17 | 23 |

Below the band on the edge of the CGO, EDX results indicated that bulk diffusion of Sr and Cr into CGO did not occur, as shown at position C. However, Cr was shown in position D to be present at the grain boundaries. It was considered that the phase formed in the grain boundaries was the same as that formed at the interface at position A. In addition, it was evident that Gd was in higher concentrations in the grain boundary relative to Ce than in the bulk grains of the CGO.

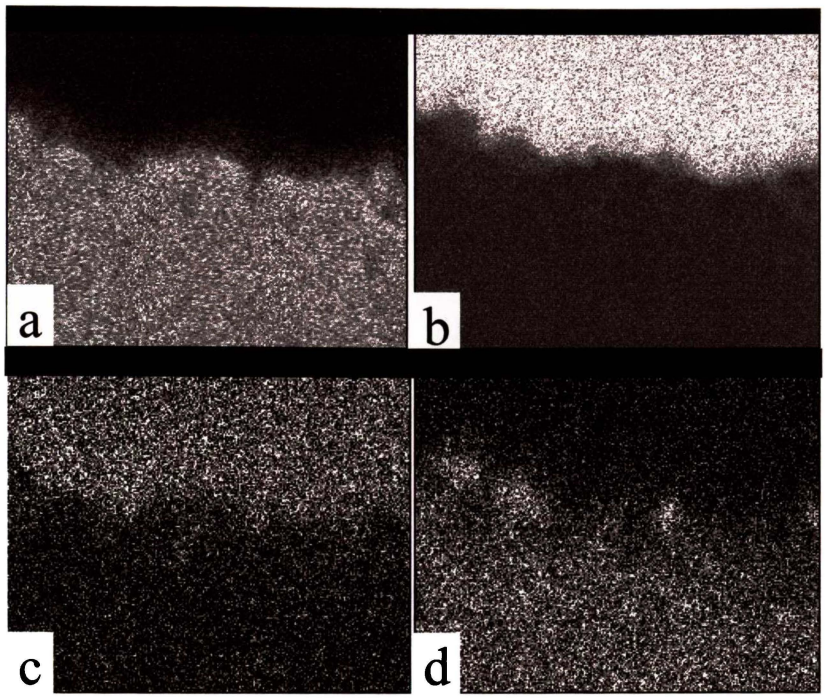


Fig. 7.5. X-ray backscattered map of the $SrCrO_4$/CGO reaction couple interface annealed at 1300°C for 24h: Ce (a); Sr (b); Cr (c); Gd (d).

### 7.4.4 Interfacial studies of $CaCrO_4$ on sintered $Ce_{0.8}Gd_{0.2}O_{1.9}$

After annealing at 1300°C for 24 h, the $CaCrO_4$ pellet had melted and enveloped the CGO pellet. The $CaCrO_4$ had turned black and had appeared, upon visual examination, to have melted through the CGO. Analysis of the backscattered SEM micrograph, Fig. 7.6 (position A), indicated that the lighter contrasted CGO grains were reacting with Ca-Cr-O transient liquid phase and being digested as the Ca-Cr-O migrated along grain boundaries, and the free surface, to form unidentified darker contrasted grains in very high concentration, position B. Pores present in CGO grains were shown to exist only after annealing, thus their formation was attributed to the reaction of CGO with $CaCrO_4$.

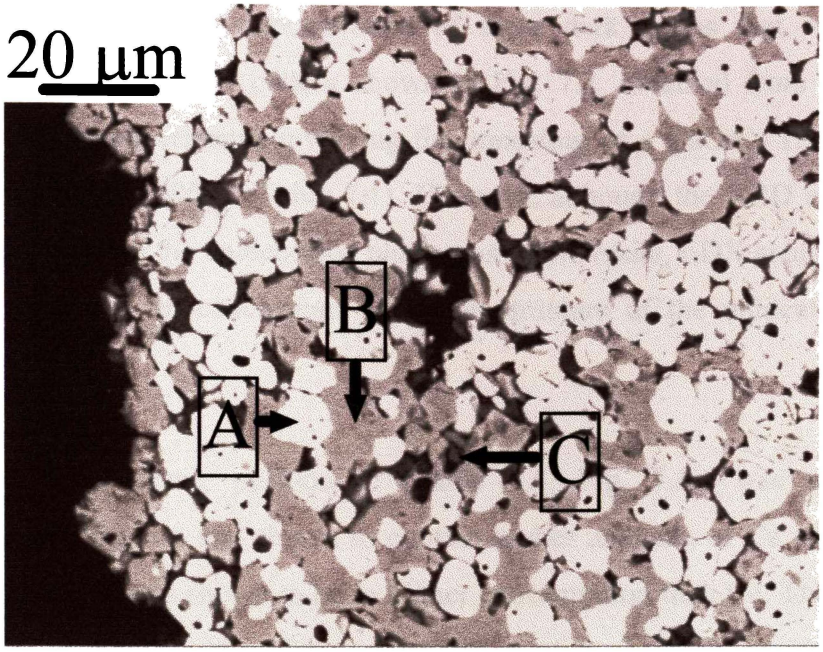


Fig. 7.6. SEM backscattered image of the $CaCrO_4$/CGO reaction couple interface annealed at 1300°C for 24 h.

Table 7.4 shows the results of the EDX point analysis performed on the $CaCrO_4$/CGO reaction couple. Analysis of an unreacted CGO grain, position A (Table 7.4, Fig. 7.6), shows there to be only Ce and Gd present. The unidentified dark grain, position B (Table 7.4, Fig. 7.6), was shown to contain Ce, Gd, Cr, and Ca, where-by these dark grains contain relatively high concentrations of Cr and Gd compared to Ca and Ce.

Table 7.4. EDX point analysis of the $CaCrO_4$/CGO reaction couple interface annealed at 1300°C for 1 h.

| Element | Position A (Element wt.%) | Position B (Element wt.%) | Position C (Element wt.%) |
|---|---|---|---|
| Ca | 2 | 11 | 32 |
| Cr | 2 | 26 | 23 |
| Ce | 67 | 12 | 2 |
| Gd | 10 | 28 | 6 |
| O | 15 | 23 | 25 |

It was the high concentration of these dark grains that was attributed to the unidentified XRD pattern shown in Fig. 7.2, obtained from the previous powder mixture experiments involving the annealing of a $CaCrO_4$ 1.36:1 CGO molar ratio reacted at 1300°C (Table 7.1). However, although the XRD analysis suggested the structure of the unidentified phase was a perovskite, EDX analysis did not show this. Therefore, no conclusions as to the structure of the unidentified phase could be drawn.

A third phase, position C (Table 7.4, Fig. 7.6), was present in very low concentrations and shown to contain higher amounts of Ca and Cr than Ce or Gd; again Gd was shown to be in higher concentration than Ce. The EDX map shown in Fig. 7.7 clearly identifies the distribution of the 2 phases present. It appeared that the $SrCrO_4$/CGO and $CaCrO_4$/CGO reaction couples, position A (Table 7.3, Fig. 7.4) and position B (Table 7.4, Fig. 7.6), had similar EDX elemental wt.% for Ce, Gd and Cr. This indicated that the phase at the interface for $SrCrO_4$/CGO couple may have been the same as the unidentified phase observed in the XRD trace of the $CaCrO_4$/CGO powder mixture in Fig. 7.2.

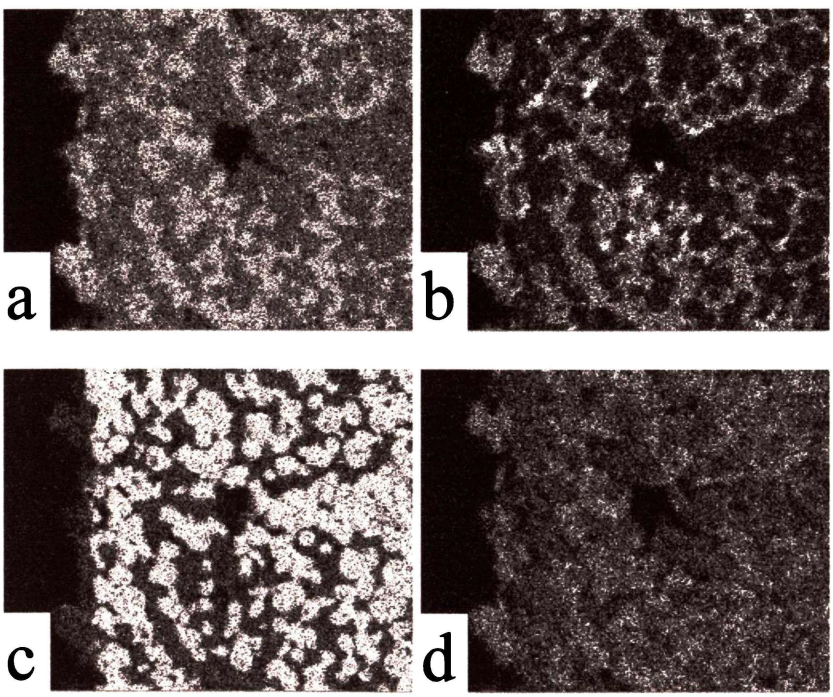


Fig. 7.7. X-ray backscattered map of the $CaCrO_4$/CGO reaction couple interface annealed at 1300°C for 24h: Cr (a); Ca (b); Ce (c); Gd (d).

## 7.5 Conclusions

$SrCrO_4$ was shown to react by way of a Sr-Cr-O liquid phase with CGO. An unknown phase formed at the $SrCrO_4$/CGO interface and grain boundaries, consisting of Ce, Gd, Sr, and Cr. Similarly, $CaCrO_4$ reacted with CGO via a transient Ca-Cr-O phase, digesting CGO grains, forming an unknown phase similar to that observed above. Phase pure $(LaSr)CrO_3$ did not react with CGO even at temperatures well above co-firing temperatures, while $Cr_2O_3$ was shown to be compatible with the electrolyte and only reacted at temperatures well above the operational and co-firing temperatures.

This study shows the detrimental effect the presence of $SrCrO_4$ and $CaCrO_4$ in doped lanthanum chromites can have on the chemical stability of CGO at the temperatures required for co-firing, and illustrates how chemical compatibility can be achieved by use of single phase $(LaSr)CrO_3$ material.

## 7.6 References


1. M. Dokiya, T. Horita, N. Saki, T. Kawada, H. Yokokawa, B. A. van Hassel, and C. S. Montross, *in* "14th Risø International Symposium on Material Science" (F. W. Poulsen, J. J. Bentzen, T. Jacobsen, E. Skou, and M. J. L. Østergård, eds.), p. 33, 1993.
2. Y. Akiyama, S. Taniguchi, T. Yasuo, M. Kadowaki, and T. Saitoh, *J. Power Sources* **50**, 361 (1994).
3. H. Schmidt, B. Brückner, and K. Fischer, *in* "Proceedings of the Fourth International Symposium on Solid Oxide Fuel Cells (SOFC-IV)" (M. Dokiya, O. Yamamoto, H. Tagawa, and S. C. Singhal, eds.), p. 869. The Electrochemical Society Inc., Yokohama, Japan, 1995.
4. T. Kimura, T. Namikawa, and Y. Yamazaki, *Denki Kagaku* **61**, 1115 (1993).
5. T. Kadowaki, T. Shiomitsu, E. Matsuda, H. Nakagawa, H. Tsuneizumi, and T. Maruyama, *Solid State Ionics* **67**, 65 (1993).
6. T. Shiomitsu, T. Kadowaki, T. Ogawa, and T. Maruyama, *in* "Proceedings of the Fourth International Symposium on Solid Oxide Fuel Cells (SOFC-IV)" (M. Dokiya, O. Yamamoto, H. Tagawa, and S. C. Singhal, eds.), p. 850. The Electrochemical Society Inc., Yokohama, Japan, 1995.
7. J. D. Carter, C. C. Appel, and M. Mogensen, *J. Solid State Chem.* **122**, 407 (1996).
8. T. Negas and R. S. Roth, *J. Res. Nat. Bur. of Standards. Sect. A* **73A**, 431 (1969).
9. T. Kawada, N. Sakai, H. Yokokawa, M. Dokiya, and I. Anzai, *Solid State Ionics* **50**, 189 (1992).
10. M. Mori, H. Itoh, N. Mori, T. Abe, O. Yamamoto, Y. Takeda, and N. Imanishi, "Science and Technology of Zirconia V," p. 776. Technomic Publishing Co. Inc., NY, 1993.
11. J. Van herle, T. Horita, T. Kawada, N. Sakai, H. Yokokawa, and M. Dokiya, *in* "Proceedings of the Fourth International Symposium on Solid Oxide Fuel Cells (SOFC-IV)" (M. Dokiya, O. Yamamoto, H. Tagawa, and S. C. Singhal, eds.), p. 1082. The Electrochemical Society Inc., Yokohama, Japan, 1995.

12. L. A. Chick, L. R. Pederson, G. D. Maupin, J. L. Bates, and J. G. Exharhos, *Mater. Lett.* **10**, 1 (1990).

# Chapter Eight

## *Conclusions and Recommendations*

## 8.1 Conclusions

As described in Chapter Two, the perovskites and perovskite-coated chromia forming metal systems are the most commonly employed current collect/interconnects in many SOFC applications.

In general, the interconnect/current collect materials must:

- have good electrical contact with the electrodes;
- have sufficient electronic conductivity;
- be chemically compatible with other cell components.

At high SOFC operating temperatures the interconnect materials' selection is restricted. A reduction in temperature will allow for a wider choice of materials. A decrease in temperature can be achieved by reducing the electrolyte thickness and/or using an electrolyte material with a higher ionic conductivity at lower temperatures.

In this thesis a number of different current collecting/interconnecting materials and designs were studied for high and medium temperature tubular SOFC systems. Commercially prepared YSZ electrolyte cells were used for high temperature studies, while medium temperature $Ce_{0.8}Gd_{0.2}O_{1.9}$ electrolyte based cells were fabricated using an extrusion technique. Novel studies on the chemical stability of the $Ce_{0.8}Gd_{0.2}O_{1.9}$ electrolyte with current-collect/interconnect materials were also performed.

As described in Chapter Four, two methods of current collection/interconnection for the cathode were developed for the YSZ electrolyte tubular SOFC. The methods were, Nimonic 90 wires coated with $LaCoO_3$ wound around the cathode, and silver coatings applied to the cathode as current collecting strips.

The coating of Nimonic 90 wires with $LaCoO_3$ was shown to improve cell performance by reducing the contact resistance between the wires and the cathode. At 0.7 V and 900°C (using $H_2$ bubbled through $H_2O$ at 25 $cm^3$ $min^{-1}$), the Nimonic 90

coated wires exhibited a current density of 49 mA $cm^{-2}$ compared to 34 mA $cm^{-2}$ for the uncoated Nimonic 90 wires. The use of Nimonic 90 wires was, however, considered to be an unsatisfactory method of cathode current collection for the YSZ-based electrolyte high temperature tubular SOFCs. When results were compared relative to those achieved for the silver current collection methods, the cell performances were much lower.

From the experimental data it was shown that the silver strips painted onto the surface of the cathodes, had cell performances that compared well with cells using the silver wire current collectors. At 900°C and 0.7 V (using $H_2$ bubbled through $H_2O$ at 25 $cm^3$ $min^{-1}$), a current density of 200 mA $cm^{-2}$ is achieved for cells with silver strip current-collectors as compared to 210 mA $cm^{-2}$ for the silver wire. When compared to the Nimonic 90 wire, the silver strip was a superior method of current collection. This was attributed to the silver having a greater electrical conductivity and better electrical contact. Unfortunately at 900°C, the evaporation rate of silver is high and therefore would not be feasible for sustained use at high temperature. It was concluded that the evaporation of silver could be greatly reduced if it was incorporated into the current collect design of a medium temperature (600°C) SOFC.

As described in Chapter Five, dense, gas-tight, medium temperature $Ce_{0.8}Gd_{0.2}O_{1.9}$ electrolyte tubes were successfully fabricated by extrusion. Processing parameters such as the modification of the $Ce_{0.8}Gd_{0.2}O_{1.9}$ particle size by heat-treatment, and addition of the correct proportion of organic extrusion aids were shown to be determining factors in the quality of the final sintered tube. Electrodes were added to the $Ce_{0.8}Gd_{0.2}O_{1.9}$ tubes and the cell tested, I-V curves were obtained. When operated at 600°C using $H_2$ bubbled through $H_2O$ at 25 $cm^3$ $min^{-1}$, a good open circuit voltage of 0.911 V was achieved for the cell. Unfortunately a poor operating current density of 12.3 mA $cm^{-2}$ at 0.7 V was obtained. The poor performance was attributed to the 400 μm thickness of the electrolyte, and because the electrodes had not been optimised for the $Ce_{0.8}Gd_{0.2}O_{1.9}$ SOFC system. The I-V characteristics obtained do, however, demonstrate that the cells have potential for fabrication and operation, as small diameter, medium temperature, tubular SOFCs.

As discussed in Chapter Six, grooved Cr5Fe1$Y_2O_3$ plates were used as an alternative method of current collection to the Nimonic 90 wire current collect and silver wires examined in Chapter Four. The grooved plates were tested on both high and medium temperature SOFCs. Cell performances were enhanced when coatings such as $La_{0.8}Sr_{0.2}CrO_3$ or Ag-$La_{0.8}Sr_{0.2}CrO_3$ were applied to the Cr5Fe1$Y_2O_3$ alloy plates.

Using the medium temperature $Ce_{0.8}Gd_{0.2}O_{1.9}$ electrolyte SOFCs developed in Chapter Five, silver was incorporated into the current collect/interconnect as a cermet coating on the metal alloy plates. Ag-$La_{0.8}Sr_{0.2}CrO_3$ was utilised, as similar cermet coatings exhibit lower resistance than the perovskite alone. At 600°C and 0.7 V, using $H_2$ bubbled through $H_2O$ at 25 $cm^3$ $min^{-1}$, a current density of 8 mA $cm^{-2}$ was achieved for the coated Cr5Fe1$Y_2O_3$ as compared to 2 mA $cm^{-2}$ for the non-coated. In comparison to the Ag-$La_{0.8}Sr_{0.2}CrO_3$ coated Cr5Fe1$Y_2O_3$, the silver wire did yield a higher performance of 12 mA $cm^{-2}$. The reduced performance of the Ag-$La_{0.8}Sr_{0.2}CrO_3$ coated plate compared to the silver wire may be due to the ceramic component having a lower conductivity at reduced temperature. When performances of the SOFCs using the Ag-$La_{0.8}Sr_{0.2}CrO_3$ and Ag-$La_{0.6}Sr_{0.4}CoO_3$ coatings were compared, the Ag-$La_{0.8}Sr_{0.2}CrO_3$ yielded better cell performances, even though the ceramic component of Ag-$La_{0.6}Sr_{0.4}CoO_3$ is reported to have a much higher conductivity. On removal of the Ag-$La_{0.6}Sr_{0.4}CoO_3$ coated interconnect from the cell, it was found that the coating had de-laminated from the Cr5Fe1$Y_2O_3$ interconnect surface. It was assumed that the thermal expansion coefficient difference between the coating and the interconnect was too large. It is believed the de-lamination induces a higher resistance, resulting in poorer cell performance.

At 900°C in air, using $H_2$ bubbled through $H_2O$ at 25 $cm^3$ $min^{-1}$, Ag-$La_{0.8}Sr_{0.2}CrO_3$ coated interconnects were used in conjunction with a high temperature, YSZ tubular electrolyte based SOFC. At 0.7 V, employing the Ag-$La_{0.8}Sr_{0.2}CrO_3$ coated Cr5Fe1$Y_2O_3$ plates, a cell current density of 40 mA $cm^{-2}$ was achieved, which compared well to 41 mA $cm^{-2}$ for the silver wire interconnect.

In comparison to the cell performance achieved using the Ag-$La_{0.8}Sr_{0.2}CrO_3$ coating, the $La_{0.8}Sr_{0.2}CrO_3$ coating exhibited reduced cell performance. The difference in

performance between the two coatings was attributed mainly to the lower resistivity of the Ag-$La_{0.8}Sr_{0.2}CrO_3$ cermet compared with the $La_{0.8}Sr_{0.2}CrO_3$ ceramic. The $La_{0.8}Sr_{0.2}CrO_3$ coating did show a gain in cell performance over the uncoated Cr5Fe1$Y_2O_3$ interconnect.

The alloy metal plate current collect design sustained the rapid start up properties required for the tubular SOFCs.

The compatibility of Cr-based interconnect related materials with the $Ce_{0.8}Gd_{0.2}O_{1.9}$ electrolyte was investigated in Chapter Seven. The $Cr_2O_3$ scale formed on the surface of Cr-based metal interconnect (such as Cr5Fe1$Y_2O_3$ used in this thesis), was shown to be compatible with the electrolyte at co-firing and operational temperatures. Similarly, the (La,Sr)$CrO_3$ ceramic interconnect proved to be compatible with $Ce_{0.8}Gd_{0.2}O_{1.9}$, even after annealing in air at temperatures as high as 1600°C.

Alternatively, $SrCrO_4$, a second phase associated with (La,Sr)$CrO_3$, was shown to react with $Ce_{0.8}Gd_{0.2}O_{1.9}$ at 1300°C forming a proposed perovskite phase, thought to be composed of Sr, Ce, Gd, and Cr. Also, $CaCrO_4$, a second phase related to the (La,Ca)$CrO_3$ interconnect material, was shown to react with $Ce_{0.8}Gd_{0.2}O_{1.9}$. It was postulated that if a second phase, such as $CaCrO_4$ or $SrCrO_4$, is present in the doped $LaCrO_3$, it may have a detrimental effect on their compatibility with $Ce_{0.8}Gd_{0.2}O_{1.9}$ during co-firing.

In summary:

- silver coatings employed as current collectors in high temperature SOFCs, achieved similar cell performances to those recorded for silver wire;
- perovskite and cermet coatings applied to the metal interconnects (both the Nimonic 90 wires and Cr5Fe1$Y_2O_3$ plates), were shown to improve the electrical contact and cell performance of SOFCs;
- medium temperature $Ce_{0.8}Gd_{0.2}O_{1.9}$ based electrolyte tubular cells can be successfully fabricated using extrusion;

- I-V curves demonstrated that $Ce_{0.8}Gd_{0.2}O_{1.9}$ based SOFCs have potential for fabrication and operation, as medium temperature, tubular SOFCs;
- single phase $La_{1-x}Sr_xCrO_3$ (x = 0-0.4), the perovskite coating used on the Cr5Fe1$Y_2O_3$ metal alloy interconnect, and the $Cr_2O_3$ scale formed on the alloy were shown to be compatible with $Ce_{0.8}Gd_{0.2}O_{1.9}$ at temperatures above operating and co-firing temperatures;
- if using (La,Sr)$CrO_3$ as a coating on the metal interconnect, second phases (such as $SrCrO_4$) should be avoided as they can react with the $Ce_{0.8}Gd_{0.2}O_{1.9}$ electrolyte at co-firing temperatures.

## 8.2 Recommendations

SOFC cell performance can be improved through optimisation of electrode, electrolyte and interconnect materials. In order to optimise the tubular SOFC systems studied in this thesis, a number of investigations could be performed.

For the $Ce(Gd)O_{2-x}$ based electrolyte system:

- optimisation of electrodes for the $Ce(Gd)O_{2-x}$ based cell;

- developments of thin film coatings to stop reduction of the $Ce(Gd)O_{2-x}$ electrolyte in fuel gas atmospheres;

For the SOFC systems in general:

- developments of lower operational temperature SOFC systems. For example an anode supported tubular SOFC with thin film (5-10 μm) YSZ or $Ce(Gd)O_{2-x}$ electrolytes may allow greater reduction in operational temperature due to decreased electrolyte thickness. The anode support tube could be fabricated using extrusion techniques.

- co-firing the interconnect with the electrodes of the tubular SOFCs, to obtain strong bonding and good electrical contact, and then to assess the thermal shock properties.

- development of functional perovskite coatings on the metal interconnect

Suggested work in the development of these functional coatings is discussed in further detail below.

### 8.2.1 Perovskite coatings on the metal interconnect.

An important consideration when stacking SOFCs is to obtain and maintain good electrical contact between the metal alloy interconnect and the electrodes, otherwise stack performance can be seriously reduced. Improved electrical contact and cell performance is achieved by application of coatings on the metal interconnect surface. Typically, chromia forming alloys such as Cr5Fe1$Y_2O_3$ coated with (La,Sr)$CrO_3$ can be used. The coating can also consist of several perovskite layers, known as "functional layers", that perform different functions.

Research detailed in this thesis showed coatings applied to metal alloys improved the performance of tubular SOFCs. In addition, studies on the stability of (La,Sr)$CrO_3$ and $Cr_2O_3$ (the oxide scale formed on the Cr5Fe1$Y_2O_3$ alloy surface) with $Ce_{0.8}Gd_{0.2}O_{1.9}$, revealed them to be chemically compatible. No studies were performed, however, using multi-functional layers.

More research needs to be performed on the use, fabrication and composition of these functional layers, in order to provide enhanced electrical contact and long-term stability.

#### 8.2.1.1 Recommended studies for development of functional perovskite layers

Initially, studies would involve the preparation of a standard interconnect material upon which coatings/functional layers can be applied and tested. It is proposed that the standard interconnect would be a $La_{0.8}Sr_{0.2}CrO_3$ coated Cr5Fe1$Y_2O_3$ alloy plate. $La_{0.8}Sr_{0.2}CrO_3$ would be applied to the metal alloy surface by vacuum plasma spray in order to form a dense coating, intimately contacting the metal alloy surface. Subsequent coating/s would then be applied over the pre-existing $La_{0.8}Sr_{0.2}CrO_3$ using an air brush or paint technique.

The fabrication of the coatings would involve:

- synthesis of perovskites by glycine nitrate process;
- fabrication of cermets;
- preparation of inks/paints containing perovskite or cermet;
- paint or airbrush coating/s over the pre-existing $La_{0.8}Sr_{0.2}CrO_3$ layer of the $La_{0.8}Sr_{0.2}CrO_3$/Cr5Fe1$Y_2O_3$ interconnect;
- firing of the coatings at various temperatures.

At the same time, investigations need to be performed to develop the coatings. The following variants could be studied:

- powder processing;
- cermet fabrication;
- coating composition;
- coating application;
- firing temperature.

Initial investigations would be kept relatively simple, varying only coating composition or firing temperature. Initial studies should be performed on silver cermet coatings such as Ag-$La_{0.8}Sr_{0.2}CrO_3$ and Ag-$La_{0.6}Sr_{0.4}CoO_3$. These coatings would be used in conjunction with medium temperature SOFCs.

Studies could involve varying the ratio of the silver to perovskite and then evaluating each coating with respect to its effectiveness in reducing contact resistance between the cathode and the metal interconnect. Under operating conditions, the contact resistance of each coating could be evaluated with respect to time. Furthermore, thermal cycling tests could be performed during the contact resistance measurements to ascertain the effect sharp temperature changes have on the coating integrity and contact resistance. SEM analysis combined with elemental mapping and microprobe analysis should be used to evaluate the stability/reactivity of the coatings themselves, and with other cell components.

Once a functional coating was found that achieved and maintained good electrical contact, a stack consisting of 6-10 cells would be constructed, employing a Cr5Fe1$Y_2O_3$/$La_{0.8}Sr_{0.2}CrO_3$ interconnect coated with the functional coating. The design of the interconnect could be similar to that described for the plate arrangement in Chapter 6, or a rod design in which the tubular SOFCs are placed in grooves along the length of the rod. The performance of the stack would be tested. For testing of long term coating integrity, cross-sections could be taken from SOFC systems that have been operated over time, to determine the stability of the coatings with the cell components under operating conditions.

# *Appendices*

# *Appendix A*

## Kröger-Vink Notation

The superscript symbols $'$, $^{\bullet}$ and $^{x}$ are used to represent a negative effective charge, positive charge and a neutral charge, respectively.

The subscript symbol denotes the lattice site label, that is either a chemical symbol, or the small letter 'i' for an interstitial site.

The main capitalised symbol designates the species occupying the site, or the capitalised letter 'V' for a vacancy on the labelled site.

For example:

$$Y_2O_3 \xrightarrow{ZrO_2} 2Y'_{Zr} + V_O^{\bullet\bullet} + 3O_O^x,$$

where: $Y'_{Zr}$ is the $Y^{3+}$ on the $Zr^{4+}$ site with an effective charge of –1;

$V_O^{\bullet\bullet}$ is the oxygen vacancy with an effective charge of +2;

$O_O^x$ is the occupied oxygen vacancy with no charge, that is, neutral.

An example of a cluster of defects can be represented:

$$(Sr'_{La} - V_O^{\bullet\bullet} - Sr'_{La})^x$$

Where, $(Sr'_{La} - V_O^{\bullet\bullet} - Sr'_{La})^x$ represents a cluster of strontium ions on lanthaum sites, associated with an oxygen vacancy, with a net neutral charge.

# *Appendix B*

A brief investigation was conducted to determine the effect temperature and time had on the grain size of $Ce_{0.8}Gd_{0.2}O_{1.9}$ extruded tubes, and is shown in Fig. 1 (Appendix B). These investigations were performed on tubes fabricated using the formulation and procedure developed for sample 4 in Chapter 5.

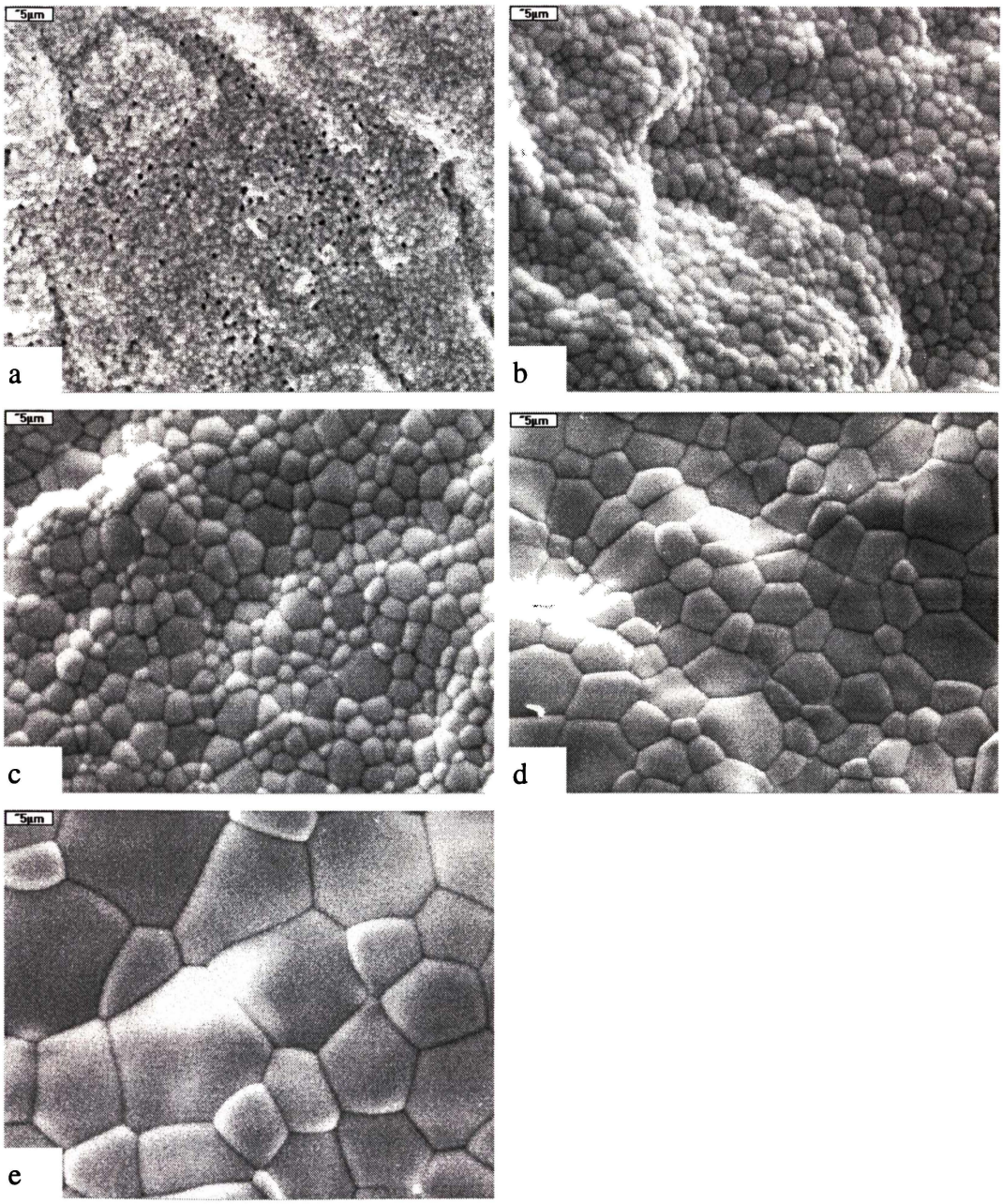


Fig. 1 (Appendix B) SEM micrographs showing the variation in surface grain size of $Ce_{0.8}Gd_{0.2}O_{1.9}$ sintered tubes with varying temperature and time: (a) 1450°C/4 h; (b) 1500°C/2 h; (c) 1550°C/2 h; (d) 1600°C/2 h; (e) 1650°C/6 h.

# *Appendix C*

Fig. 1 (appendix C) shows the adverse affect the $CaCrO_4$ melt (Ca-Cr-O) has on the $Ce_{0.8}Gd_{0.2}O_{1.9}$.electrolyte pellet. The $Ce_{0.8}Gd_{0.2}O_{1.9}$ pellet has formed cracks after annealing. Analysis described in Chapter indicated the $Ce_{0.8}Gd_{0.2}O_{1.9}$ grains were reacting with the Ca-Cr-O melt and being digested as the Ca-Cr-O migrated along grain boundaries, and the free surface to form an unidentified phase consisting of Ca-Cr-Ce-Gd-O.

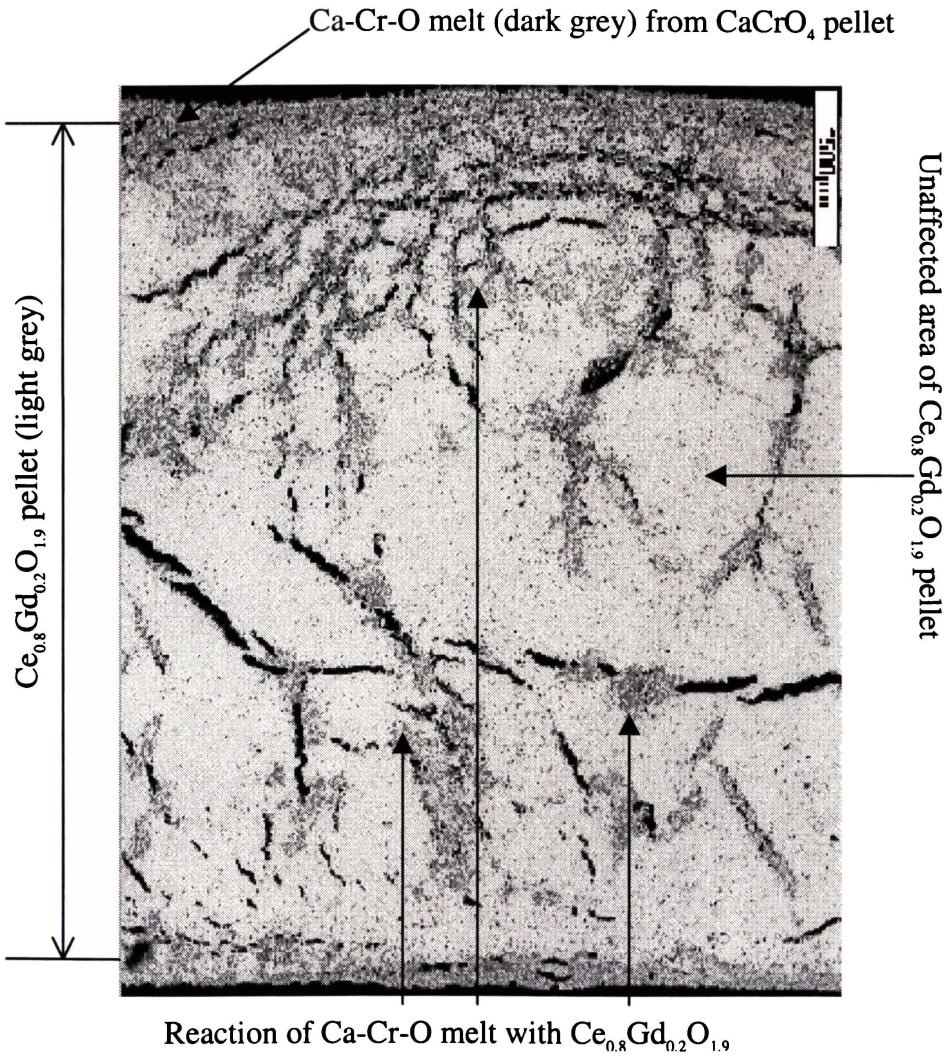


Fig. 1. SEM micrograph showing a cross section of a $Ce_{0.8}Gd_{0.2}O_{1.9}$ pellet annealed with a $CaCrO_4$ pellet. The $CaCrO_4$ pellet was placed on top of the $Ce_{0.8}Gd_{0.2}O_{1.9}$ pellet (top of picture) and annealed in air at 1300°C for 24 h. The Ca-Cr-O melt enveloped the entire $Ce_{0.8}Gd_{0.2}O_{1.9}$ pellet and migrated into the pellet reacting with the $Ce_{0.8}Gd_{0.2}O_{1.9}$.